


Summer 7-29-2017

GEOCHEMISTRY OF VOLATILES RELEASED BY INCIPIENT CONTINENTAL RIFTING AND SUBDUCTION PROCESSES

Hyunwoo Lee
University of New Mexico

Follow this and additional works at: https://digitalrepository.unm.edu/eps_etds

 Part of the [Geochemistry Commons](#), [Geology Commons](#), and the [Tectonics and Structure Commons](#)

Recommended Citation

Lee, Hyunwoo. "GEOCHEMISTRY OF VOLATILES RELEASED BY INCIPIENT CONTINENTAL RIFTING AND SUBDUCTION PROCESSES." (2017). https://digitalrepository.unm.edu/eps_etds/199

This Dissertation is brought to you for free and open access by the Electronic Theses and Dissertations at UNM Digital Repository. It has been accepted for inclusion in Earth and Planetary Sciences ETDs by an authorized administrator of UNM Digital Repository. For more information, please contact disc@unm.edu.

Hyunwoo Lee

Candidate

Earth and Planetary Sciences

Department

This dissertation is approved, and it is acceptable in quality and form for publication:

Approved by the Dissertation Committee:

Tobias P. Fischer, Chairperson

Zachary D. Sharp

Laura J. Crossey

Karl E. Karlstrom

Jolante van Wijk

**GEOCHEMISTRY OF VOLATILES RELEASED BY
INCIPIENT CONTINENTAL RIFTING AND SUBDUCTION PROCESSES**

by

HYUNWOO LEE

B.S., Geological Science, Yonsei University, 2009
M.S., Geological Science, Yonsei University, 2011

DISSERTATION

Submitted in Partial Fulfillment of the
Requirements for the Degree of

**Doctor of Philosophy
Earth and Planetary Sciences**

The University of New Mexico
Albuquerque, New Mexico

July, 2017

DEDICATION

This dissertation is dedicated to my grandmother, Boksoon Kim

ACKNOWLEDGEMENTS

Most of all, I would like to express my highest gratitude to my advisor, Tobias Fischer. First, I could leave South Korea to start my Ph.D. degree in this country because you were only person who gave an admission. I feel very grateful because I could get my Ph.D. degree under the guidance of a great volcanologist and scientist. Since August in 2012, I cannot count how many times I could have discussion with you, which made me well in Volcanology and Geochemistry. Also, spending a lot of time in the Volatiles Laboratory with you made me expertise in analyzing volcanic and hydrothermal samples. Field trips in East Africa and Costa Rica were great experiences. Ultimately, I could keep going on my track because you always believe me. I thank Zachary Sharp who is a great stable isotope geochemist for supporting my isotope analyses and giving me great insights. Thank Laura Crossey and Karl Karlstrom for your kind mentorship. I also appreciate Jolante van Wijk from New Mexico Tech, Socorro for accepting the external committee offer. In addition, I would like to express my appreciation to Nicu-Viorel Atudorei for supporting a lot of stable isotope analyses. Moreover, the road trip with Viorel from Ottawa, Canada to Albuquerque to deliver a mass spectrometer is one of the greatest experiences during my Ph.D. years. I am grateful to Cynthia Ebinger, Simon Kattenhorn, Maarten de Moor, Yuji Sano, and Naoto Takahata for collaborating exciting studies. Especially, I would like thank James Muirhead for your friendship and mentorship. My Ph.D. studies were sponsored by NSF (EAR-1113066 and EAR-1049713) and Sandia National Laboratories. I thank the department of Earth and Planetary Sciences, Cindy Jaramillo, Paula Pascetti, and Faith Mutchnik for supporting me during my Ph.D. period in Northrop hall. I am deeply grateful to my parents and brothers for waiting for me to finish my higher education. Finally, my achievement is a tribute to my wife, Anna Jo.

GEOCHEMISTRY OF VOLATILES RELEASED BY INCIPIENT CONTINENTAL RIFTING AND SUBDUCTION PROCESSES

By

HYUNWOO LEE

B.S., Geological Science, Yonsei University, 2009

M.S., Geological Science, Yonsei University, 2011

Ph. D., Earth and Planetary Sciences, University of New Mexico, 2017

ABSTRACT

Volatiles (N₂, CO₂, and He) are released by volcanism and hydrothermal activity during continental rifting and subduction processes. Analyses of volatile components have been conducted to obtain gas contents (CO₂, SO₂, H₂S, N₂, Ar, He, and so on), stable isotope compositions ($\delta^{13}\text{C}$, $\delta^{15}\text{N}$, and so on), and noble gas isotopes ($^3\text{He}/^4\text{He}$, $^{40}\text{Ar}/^{36}\text{Ar}$, and so on). This dissertation includes four chapters to report new nitrogen isotope fractionation factors of bubbling gases during gas-water transfer at various water temperatures (Chapter 1), first measurements of massive amounts of CO₂ released by incipient continental rifting in the Magadi and Natron Basin, East African Rift (Chapter 2), new results of gas chemistry, stable isotopes, and noble gas isotopes of hot springs in the same area as Chapter 2 (Chapter 3), and new nitrogen isotope compositions of springs at the Costa Rican subduction zone (Chapter 4).

Chapter 1 (published in *Geochemical Journal*) is the first experimental work to acquire nitrogen isotope fractionation factors during N₂ gas and water transfer at various temperature to examine nitrogen isotope shift for hydrothermal systems. This work reports measured $\delta^{15}\text{N}$ values of dissolved N₂ gas at 5 to 60°C. We obtained $\delta^{15}\text{N}$ values of 0.91, 0.73, -0.04, and -0.42‰ at 5, 20, 40, and 60°C, respectively. Nitrogen isotope fractionation depending on

temperature is more significant than previously published results, showing an isotopic 'crossover' at 40°C. A kinetic incorporation of ^{14}N into water is enhanced by rising temperatures could explain the steep temperature dependence. In hydrothermal systems, small negative $\delta^{15}\text{N}$ values could be attributed to kinetic fractionation between dissolved N_2 and N_2 in air.

Chapter 2 (published in *Nature Geoscience*) is the first estimation of diffuse CO_2 degassing (“Tectonic Degassing”) along faults which are away from active volcanic centers in the East African Rift. We used results of diffuse soil CO_2 measurements combined with carbon isotopic compositions to quantify the flux of CO_2 and constrain CO_2 sources. This study reports that 4.05 mega tons per year of mantle-derived CO_2 is released by faults penetrating the lower crust in the Magadi-Natron Basin. Extrapolated CO_2 flux (71 ± 33 mega tons per year) of the entire Eastern rift (~3,000 km long from Afar to Mozambique) is comparable to CO_2 emission from the entire mid-ocean ridge system (53-97 mega tons per year). Therefore, widespread continental rifting and super-continent breakup could result in massive and long-term CO_2 emissions, contributing prolonged greenhouse conditions likely during the Cretaceous.

Chapter 3 (published in *Journal of Volcanology and Geothermal Research*) reports new results of gas compositions, stable isotopes (O, H, N, and C), and noble gas isotopes (He and Ar) of hot spring samples from the Magadi and Natron basin in the East African Rift (EAR). In dissolved gases, CO_2 is the most abundant component. Deep and shallow sources are mixed based on the N_2 -He-Ar abundances. $\delta^{18}\text{O}$ and δD values of the spring waters indicate that the local meteoric water is dominant with minor evaporation. Most of $\delta^{15}\text{N}$ and $\delta^{13}\text{C}$ values and $^3\text{He}/^4\text{He}$ ratios suggest that Subcontinental Lithospheric Mantle (SCLM) is the major mantle source. The ^4He flux values, significantly greater than the reported mean of global continental flux values, imply that elevated mantle ^4He flux is due to magmatism and related heating, and crustal ^4He is released by fracturing of old rocks in the Tanzanian craton and Mozambique belt.

SCLM-derived volatiles can be ascribed to that a relatively small volume of lithospheric mantle has been replaced by asthenosphere during incipient rifting (<10 Ma).

Chapter 4 (in preparation) shows new results of gas compositions, nitrogen, and helium isotopes of springs at forearc and arc front areas in Costa Rica. Nitrogen isotope compositions ($9-11\text{‰}$) with less pelagic sediment contribution compared to further north (Guatemala and Nicaragua) result in insufficient nitrogen output to the atmosphere. This work supports the subduction erosion model in conjunction with seamount subduction. The overlying forearc crustal materials incorporated into the Costa Rican subduction zone dilute sediment-derived nitrogen signals. These results support the deep recycling of N into the deep mantle.

TABLE OF CONTENTS

PREFACE.....	1
CHAPTER 1. KINETIC NITROGEN ISOTOPE FRACTIONATION BETWEEN AIR AND DISSOLVED N ₂ IN WATER: IMPLICATIONS FOR HYDROTHERMAL SYSTEMS.....	
1. ABSTRACT.....	4
2. INTRODUCTION.....	4
3. EXPERIMENTAL METHOD.....	5
4. RESULTS.....	10
5. DISCUSSION.....	10
6. CONCLUSIONS.....	11
7. REFERENCES.....	12
CHAPTER 2. MASSIVE AND PROLONGED DEEP CARBON EMISSIONS ASSOCIATED WITH CONTINENTAL RIFTING.....	
1. ABSTRACT.....	13
2. INTRODUCTION.....	14
3. METHODS.....	17
3.1. CO ₂ gas accumulation chamber method.....	17
3.2. Field sampling strategy.....	18
3.3. Laboratory analyses of gas compositions and C isotopes.....	18
3.4. Analysis of broadband seismic data.....	20

4. RESULTS AND DISCUSSION.....	24
5. REFERENCES.....	30

CHAPTER 3. INCIPIENT RIFTING ACCOMPANIED BY THE RELEASE OF
SUBCONTINENTAL LITHOSPHERIC MANTLE VOLATILES

IN THE MAGADI AND NATRON BASIN, EAST AFRICA.....	36
1. ABSTRACT.....	36
2. INTRODUCTION.....	37
3. REGIONAL SETTING.....	39
4. SAMPLES AND ANALYTICAL METHODS.....	46
5. RESULTS.....	49
6. DISCUSSION.....	57
6.1. Gas geochemistry.....	57
6.2. Gas geothermometry.....	60
6.3. Stable isotopes.....	66
6.3.1. O and H isotopes.....	66
6.3.2. N ₂ sources.....	66
6.3.3. CO ₂ sources.....	76
6.4. Helium sources.....	82
6.5. Continental ⁴ He flux.....	84
6.6. Mantle-derived volatile fluxes in the MNB hydrothermal system.....	86
6.7. Geochemical implications for continental rifting.....	88
7. CONCLUSIONS.....	89
8. REFERENCES.....	95

CHAPTER 4. NITROGEN RECYCLING AT THE COSTA RICAN SUBDUCTION ZONE: THE ROLE OF INCOMING PLATE STRUCTURE.....	111
1. ABSTRACT.....	111
2. INTRODUCTION.....	112
3. EXPERIMENTAL METHODS.....	115
4. RESULTS.....	121
5. DISCUSSION.....	128
6. CONCLUSIONS.....	132
7. REFERENCES.....	134
 APPENDIX 1: SUPPLEMENTARY INFORMATION FOR CHAPTER 2.....	 144
A.1.1. SUPPLEMENTARY TEXT.....	144
A.1.1.1. Definition of tectonic degassing.....	144
A.1.1.2. Definition of structural zones from field-based analyses and aerial mapping.....	144
A.1.1.3. Structural controls on CO ₂ degassing.....	145
A.1.1.4. Estimating CO ₂ flux in the Magadi-Natron basin and Eastern rift of the EAR.....	145
A.1.1.5. Sources of CO ₂ in the Magadi-Natron basin.....	149
A.1.2. SUPPLEMENTARY FIGURES AND TABLES.....	151
A.1.3. SUPPLEMENTARY REFERENCES.....	164
 APPENDIX 2: SUPPLEMENTARY INFORMATION FOR CHAPTER 3.....	 170
APPENDIX 3: SUPPLEMENTARY INFORMATION FOR CHAPTER 4.....	172

PREFACE

This dissertation is made up of four chapters. Chapters 1, 2, and 3 have been published in relevant scientific journals. Chapter 4 is under the peer review process for submitting soon. Hyunwoo Lee holds a first and corresponding authorship for all chapters. Unpublished data for Chapters 2, 3, and 4 is reported in Appendices 1, 2, and 3, respectively.

Chapter 1. This chapter has been published in *Geochemical Journal* (2015). Hyunwoo Lee conducted an experiment to measure nitrogen isotope fractionation factors of air-water transfer at various water temperatures based on the design from Tobias Fischer. Under the guidance of Zachary Sharp, nitrogen isotope compositions of bubbling water samples were measured by Isotope Ratio Mass Spectrometer at the Center for Stable Isotopes (CSI), University of New Mexico (UNM). The manuscript was collaborated written by Hyunwoo Lee, Zachary Sharp, and Tobias Fischer.

Chapters 2 and 3 are studies on the Magadi and Natron basin in the East African Rift. The Magadi and Natron basin is a young section in the rift (< 10 Ma), located in southern Kenya and northern Tanzania. The field works have been conducted in 2013 and 2014 to measure diffuse CO₂ flux of fault zones in the Magadi and Natron basin and collect fumarole and hot spring samples in the area and the Kenya Rift Valley.

Chapter 2 has been published in *Nature Geoscience* (2016), reporting the results of diffuse CO₂ flux. This study was the first attempt to quantify the amount of diffuse CO₂ along faults away from active volcanoes in continental rifts and suggested a new CO₂ input to

the atmosphere. Hyunwoo Lee, James Muirhead, Tobias Fischer, and Cynthia Ebinger joined the field campaign. Gladys Kianji from University of Nairobi, Kenya supported the field trip. Hyunwoo Lee, James Muirhead, and Tobias Fischer measured CO₂ flux and collected gas samples. Hyunwoo Lee analyzed gas compositions at the Volatiles Laboratory (UNM) and carbon isotope compositions of CO₂ at CSI (UNM). Carbon isotope analyses were supported by Zachary Sharp and Nicu-Viorel Atudorei. James Muirhead and Cynthia Ebinger interpreted geophysical results from seismic stations and calculated the extrapolated CO₂ flux for the entire Eastern rift of the East African Rift. Hyunwoo Lee, James Muirhead, Tobias Fischer, Cynthia Ebinger, and Simon Kattenhorn collaboratively wrote the manuscript.

Chapter 3 is a subsequent work and has been published in *Journal of Volcanology and Geothermal Research* (2017). Hyunwoo Lee and Tobias Fischer collected fumarole and hot spring samples in the Kenya Rift Valley in 2013. Hyunwoo Lee, Tobias Fischer, and James Muirhead sampled hot springs in the Magadi and Natron basin in 2014. Hyunwoo Lee analyzed gas compositions, argon isotopes, and stable isotopes (O, H, C, and N) at the Volatiles Lab and CSI of UNM. Helium isotope ratios were measured by Hyunwoo Lee at the Atmosphere and Ocean Research Institute (AORI) of University of Tokyo supported by Naoto Takahata and Yuji Sano. The manuscript was written by Hyunwoo Lee, Tobias Fischer, and James Muirhead with feedback from Cynthia Ebinger, Simon Kattenhorn, and Zachary Sharp.

Chapter 4 is a manuscript under the peer review process, which contains results of gas compositions, nitrogen isotopes, and noble gas geochemistry from samples collected in Costa Rica (2014). Hyunwoo Lee, Tobias Fischer, and Maarten de Moor collected spring samples in the Nicoya and Santa Elena forearc areas as well as a hot spring near the Rincon de la Vieja volcano. Laura Clor collected arc front spring samples in 2012. Hyunwoo Lee measured gas compositions, argon isotopes, and nitrogen isotope compositions the Volatiles Lab and CSI of UNM. Helium isotope ratios were measured by Hyunwoo Lee with supports from Naoto Takahata and Yuji Sano at AORI. Hyunwoo Lee and Tobias Fischer wrote the manuscript which will be submitted to a relevant journal.

CHAPTER 1

KINETIC NITROGEN ISOTOPE FRACTIONATION BETWEEN AIR AND DISSOLVED N₂ IN WATER: IMPLICATIONS FOR HYDROTHERMAL SYSTEMS

Citation: Lee, H., Sharp, Z. D., and Fischer, T. P. (2015). Kinetic nitrogen isotope fractionation between air and dissolved N₂ in water: Implications for hydrothermal systems. *Geochemical Journal* 49 (5), 571-573.

1. ABSTRACT

Nitrogen isotopes are widely used to trace volatile sources in volcanic/hydrothermal systems. However, the nitrogen isotope composition of dissolved N₂ may not be the same as N₂ gas, due to minor isotope fractionation. In order to evaluate N isotope fractionation during dissolution of N₂ gas in water as a function of temperature, we measured $\delta^{15}\text{N}$ values of dissolved N₂ over a temperature range of 5 to 60°C. Our experiments show that $\delta^{15}\text{N}$ values are 0.91, 0.73, -0.04, and -0.42‰ at 5, 20, 40, and 60°C, respectively. The temperature dependent fractionation is stronger than published results and indicates an isotopic 'crossover' at 40°C. A possible explanation for the steep temperature dependence is that a kinetic-based incorporation of the light isotope (¹⁴N) into water increases as temperature rises. We show that small negative $\delta^{15}\text{N}$ values in natural springs could be due to kinetic fractionation between dissolved N₂ and N₂ in air.

2. INTRODUCTION

N is the most abundant gas in the atmosphere (78%), with two isotopes, ¹⁴N (99.63%) and ¹⁵N (0.37%). The isotope composition of N₂ dissolved in ocean water equilibrated with the atmosphere is +0.6‰ (Sigman et al., 2009). However, N also occurs naturally as NH₃,

NO, and NO₂. N isotopes are fractionated by fixation, nitrification, denitrification, and other biological processes, resulting in a wide range of isotope compositions ($\delta^{15}\text{N} = -16$ to $+30\%$, Sigman et al., 2009). For investigations regarding mantle geochemistry and global volatile cycles, N isotopes are commonly used to trace the source in terms of atmosphere ($\delta^{15}\text{N} = 0\%$), the mantle ($\delta^{15}\text{N} = -5 \pm 2\%$), and organic sediments in subduction zones ($\delta^{15}\text{N} = 0$ to $+10\%$) (Sano et al., 1998; Fischer et al., 2002). As a nonreactive volatile component, dissolved N₂ is commonly measured in springs at various water temperatures in order to identify N sources. However, its fractionation process during dissolution of N₂ in water has not yet been systematically investigated. There are a few studies that experimentally determined $\delta^{15}\text{N}$ values during N₂ gas transfer between water and air at ambient temperature (Klotts and Benson, 1963; Knox et al., 1992). However, isotopic fractionation at higher water temperature (e.g., $> 30\sim 40^\circ\text{C}$), i.e. representing a hydrothermal system, has not been yet considered. Here we report the result of an experiment, where N₂ with $\delta^{15}\text{N}$ value of 0% (air which is the N₂ source used) was dissolved in water at 5, 20, 40 and 60°C , and show how the N isotope composition is fractionated during dissolution in water.

3. EXPERIMENTAL METHOD

To conduct the experiment, 1L beakers filled with distilled water and exposed to air were heated with a hot plate and cooled down with ice to reach the desired temperatures (5, 20, 40, and 60°C). After the water samples had reached the desired temperatures, they were continuously aerated with ambient air that had a $\delta^{15}\text{N}$ value of 0.0% by an aquarium air pump (Aqua Culture, flow rate: 1.2L/minute) for 20~30 minutes. 20mL glass vials

equipped with rubber septa and metal caps were used to sample the water. It was critical that vials were filled and capped underwater in order to prevent any ambient air contamination. Sampling was repeated until there were no air bubbles observed in the vials. After collection, the vials were flushed with helium (He) in order to obtain a headspace (8ml). The flushing was performed by a 5cm long needle with two holes inserted through the septum. The needle was used to inject He and extract water simultaneously. Each vial was filled with the same amount of He gas as recorded by the displacement of the water, which was approximately 5ml. Then the vial was shaken by hand for 15 minutes and left overnight at 20°C to ensure equilibration following the same method of McCarty and Blicher-Mathiesen (1996), who let their vials equilibrate for 24 hours at room temperature. We measured vial headspaces by a Finnigan Delta XL stable isotope mass spectrometer with a gas bench in the Center for Stable Isotopes, University of New Mexico. For each analysis, we performed two injections of N₂ reference gas and five injections of sample headspaces. N isotope compositions are expressed as $\delta^{15}\text{N}$ (‰), the standard is air (0.0‰). In order to determine the air standard, empty vials were exposed to room air for a minute and then measured for $\delta^{15}\text{N}$ by the same method. The mean $\delta^{15}\text{N}$ value of 20 measurements of room air is -0.60‰ ($2\sigma = \pm 0.22\%$). All data were corrected to our air standard, assuming it had a $\delta^{15}\text{N}$ value of 0.0‰. Even if this assumption is not exact, the measurement of the N isotopic fractionation (i.e., relative differences) which we calculated relative to our measured air standard, is accurate.

Table 1. Experimental results of each temperature.

temperature °C	solubility (mole fraction x 10 ⁵)	N ₂ peak intensity		δ ¹⁵ N	
		(mV)	2σ	(‰ vs. air)	2σ
5	1.695	3218	60	0.91	0.22
20	1.274	2589	196	0.73	0.17
40	0.998	2104	7	-0.04	0.36
60	0.886	1795	421	-0.42	0.42

Note: solubility data from Battino et al. (1984); N₂ peak intensity and δ¹⁵N values

are mean values.

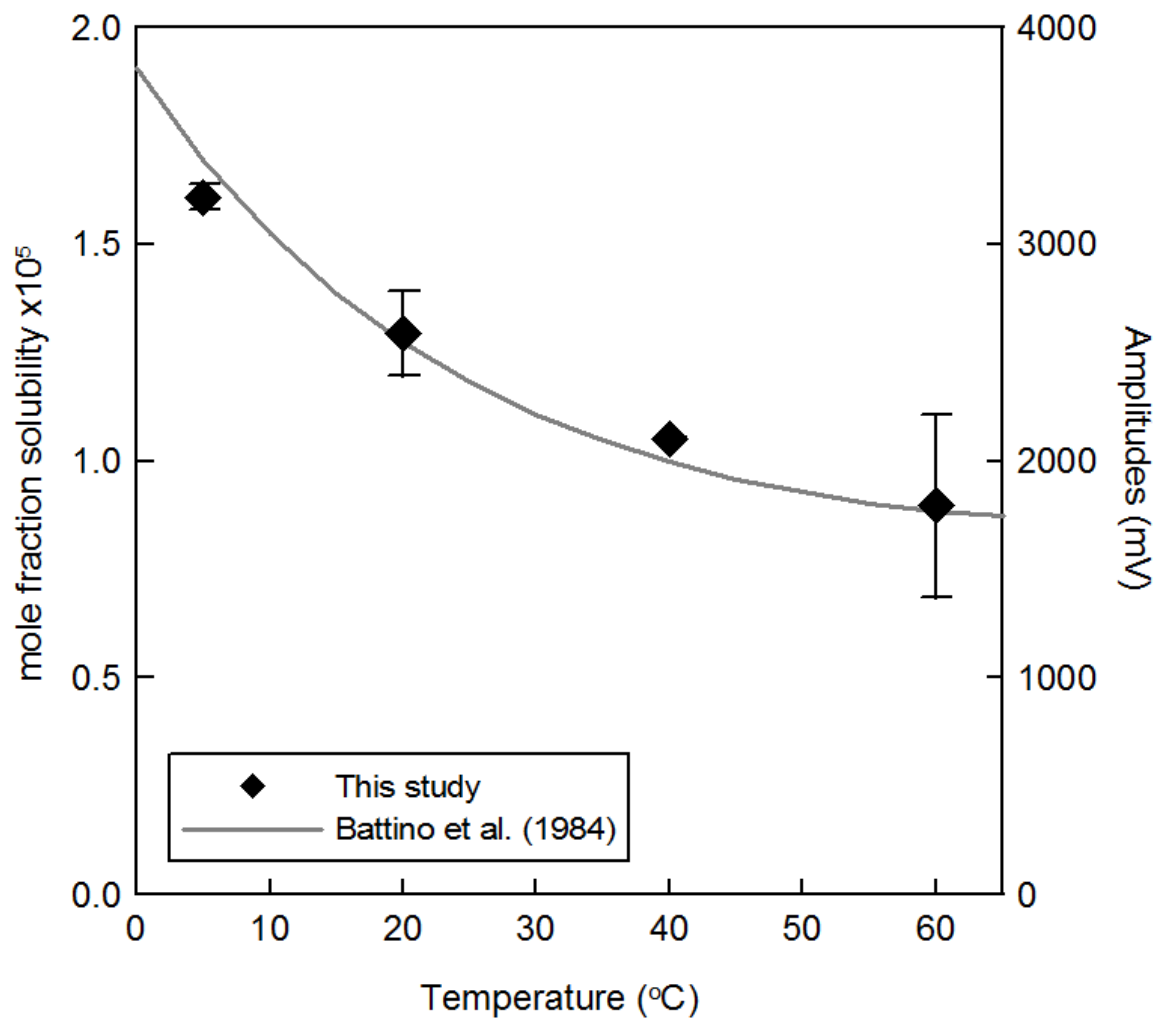


Fig. 1. Intensities (mV) of four sample headspace injections at 5, 20, 40, and 60°C, respectively (black diamonds). Error bars are 2σ of intensities (Table 1). Gray curve indicates solubility (mole fraction $\times 10^5$) of N_2 in water at 1atm (Battino *et al.*, 1984).

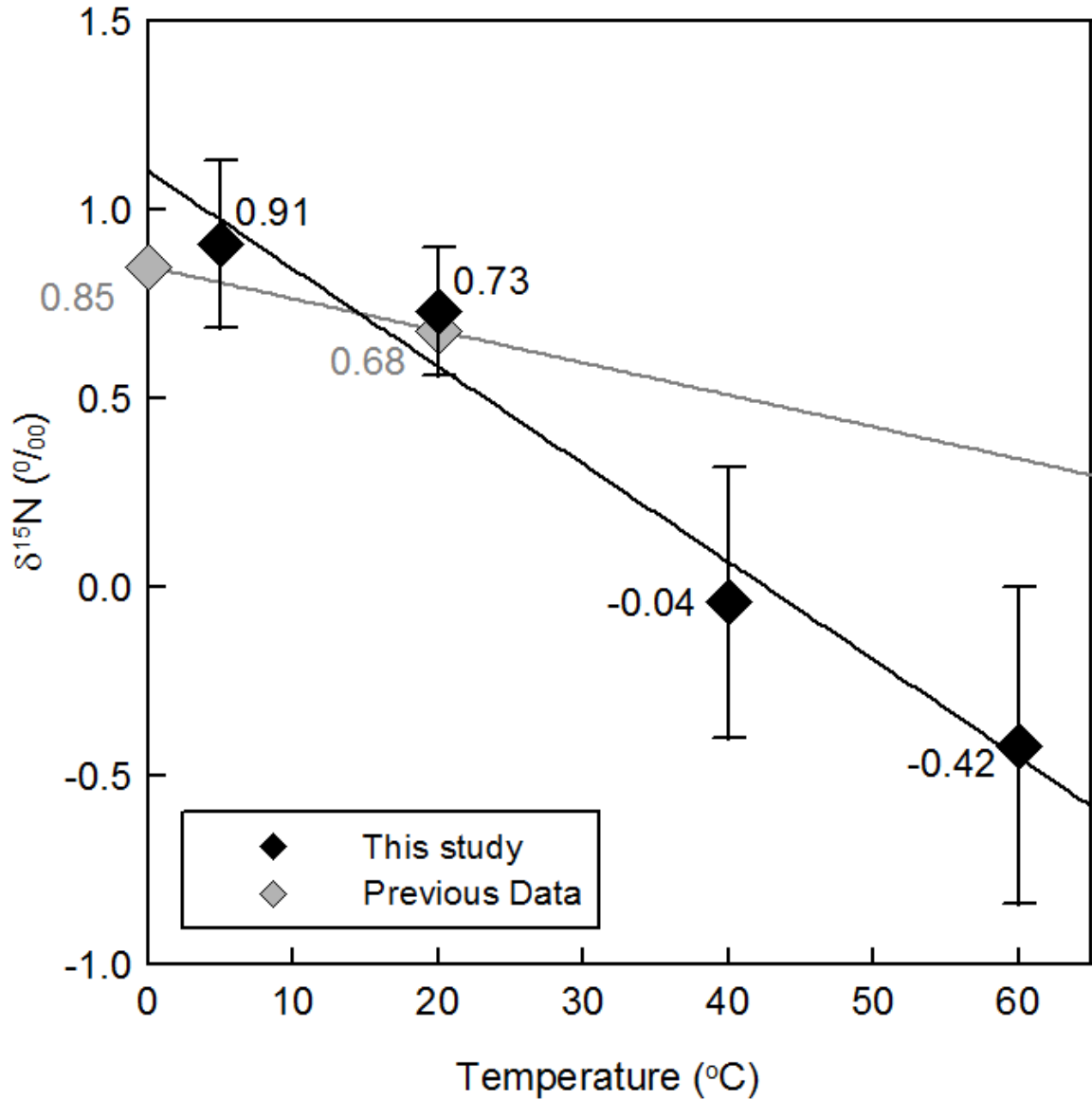


Fig. 2. $\delta^{15}\text{N}$ values between dissolved N_2 and air with $\delta^{15}\text{N}$ values of samples measured at 5, 20, 40, and 60 $^{\circ}\text{C}$ (black diamonds). Labels of mean $\delta^{15}\text{N}$ values (black diamonds) at each temperature and the regression line are shown. Error bars are 2σ of mean $\delta^{15}\text{N}$ values (Table 1). Previous published values (gray diamonds) of 0.85 ‰ at 0 $^{\circ}\text{C}$ (Klots and Benson, 1963) and 0.68‰ at 20 $^{\circ}\text{C}$ (Knox *et al.*, 1992) are displayed as well as the regression line.

4. RESULTS

Mean values of N_2 amounts are expressed as peak intensities (mV) from the mass spectrometer (Table 1). The inverse relationship between N_2 amounts and temperature is in good agreement with the N_2 solubility in water (Battino et al., 1984) at each temperature (Fig. 1). Measured mean $\delta^{15}N$ values of headspaces are 0.91, 0.73, -0.04, and -0.42‰ at 5, 20, 40, and 60°C, respectively. Although headspaces have been equilibrated with water at 20°C for 24 hours, an additional fractionation process between headspaces and residual water is negligible because virtually all of the N_2 gas is transferred to the headspace. Also, the relationship between sample intensities and $\delta^{15}N$ values is not attributed to mass fractionation in the mass spectrometer because our air-standards show constant N isotope compositions (-0.60 ± 0.22 ‰) at different intensities (3535 to 8971 mV; mass spectrometer source pressures).

The previously reported $\delta^{15}N$ value of equilibrium isotope fractionation at 20°C is 0.68‰ (Knox et al., 1992), in good agreement with our measured value of 0.73 ± 0.17 ‰ (Fig. 2). At higher temperatures, our measured isotope compositions decrease distinctly with temperature, reaching a crossover at 40°C and negative fractionation due to preferential incorporation of ^{14}N in water.

5. DISCUSSION

Our fractionation data at low temperatures overlap with previous estimates by Klots and Benson (1963) and Knox et al. (1992), but show stronger temperature dependence. At 60°C the data of Klots and Benson (1963) extrapolate to $\delta^{15}N$ of ~ -0.5 ‰, whereas our measured

$\delta^{15}\text{N}$ value is -0.42‰ (Fig. 2). We interpret the difference to a substantial kinetic effect in our experimental setup.

Knox et al. (1992) showed that there is a preference for the light isotope during the early stages of N_2 incorporation into N-free water. At 10 and 20°C, the maximum enrichment was about 0.1‰. Our data suggest a far stronger enrichment, which is probably due to the turbulent mixing during the bubbling of air through our water samples. Our experiments lasted only 30 minutes; whereas Knox et al. (1992) showed that full equilibration in a non-turbulent system took between 15 and 20 days. Presumably, in our high temperature experiments, there was a preferential incorporation of the light isotope. Given that the initial concentration of dissolved nitrogen in the water was presumably at saturation, our data suggest that this kinetic effect may be at steady state, although additional experiments run for different amounts of time are necessary to confirm this hypothesis.

6. CONCLUSIONS

The equilibrium fractionation between N_2 dissolved in water and air is fairly constant at 0.5 to 0.9‰, depending on the temperature. We have shown that in a turbulent system, equilibrium may not be reached, and reverse fractionation can occur even when solubilities appear to have reached saturation. In a turbulent hydrothermal or volcanic system, boiling and bubbling of gases through water could lead to negative isotope fractionation. A negative $\delta^{15}\text{N}$ value of a sample from a bubbling spring is normally considered to be indicative of a mantle nitrogen component (e.g., Sano et al., 1998; Fischer et al., 2002). The results of our present experiments demonstrate that slightly negative $\delta^{15}\text{N}$ values of about -1‰ may result from non-equilibrium exchange with air. Nitrogen isotope values in

natural samples from springs should, therefore, always be combined with $N_2/{}^3He$ $N_2/{}^{36}Ar$ (Sano et al., 1998) or N_2/He (Fischer et al., 2002) to adequately characterize the potential mantle signature of gas discharges.

7. REFERENCES

- Battino, R., Rettich, T. R. and Tominaga, T. (1984) The solubility of Nitrogen and Air in liquids. *J. Phys. Chem. Ref. Data* **13**, 563-600.
- Fischer, T. P., Hilton, D. R., Zimmer, M. M., Shaw, A. M., Sharp, Z. D. and Walker, J. A. (2002) Subduction and recycling of nitrogen along the Central American margin. *Science* **297**, 1154-1157.
- Klots, C. E. and Benson, B. B. (1963) Isotope effect in the solution of oxygen and nitrogen in distilled water. *J. Chem. Phys.* **38**, 890-892.
- Knox, M., Quay, P. D. and Wilbur, D. (1992) Kinetic isotopic fractionation during air-water gas transfer of O_2 , N_2 , CH_4 , and H_2 . *J. Geophys. Res.* **97**, 20335-20343.
- McCarty, G.W. and Blicher-Mathiesen, G. (1996) Automated chromatographic analysis of gases in soil and water. *Soil Sci. Soc. Am. J.* **60**, 1439-1442.
- Sano, Y., Takahata, N., Nishio, Y. and Marty, B. (1998) Nitrogen recycling in subduction zones. *Geophys. Res. Lett.* **25**, 2289-2292.
- Sigman, D. M., Karsh, K.L. and Casciotti, K. L. (2009), Ocean Process tracers: Nitrogen isotopes in the ocean. *Encyclopedia of Ocean Sciences* (update from 2001), academic press, London, 4138-4153.

CHAPTER 2

MASSIVE AND PROLONGED DEEP CARBON EMISSIONS ASSOCIATED WITH CONTINENTAL RIFTING

Citation: Lee, H., Muirhead, J. D., Fischer, T. P., Ebinger, C. J., Kattenhorn, S. A., Sharp, Z. D., and Kianji, G. (2016). Massive and prolonged deep carbon emissions associated with continental rifting. *Nature Geoscience* 9, 145-149.

1. ABSTRACT

Carbon from Earth's interior is thought to be released to the atmosphere mostly via degassing of CO₂ from active volcanoes (Marty and Tolstikhin, 1998; Pérez et al., 2011; Burton et al., 2013; Kagoshima et al., 2015). CO₂ can also escape along faults away from active volcanic centers, but such tectonic degassing is poorly constrained (Burton et al., 2013). Here we use measurements of diffuse soil CO₂, combined with carbon isotopic analyses to quantify the flux of CO₂ through fault systems away from active volcanoes in the East African Rift system. We find that about 4 megatons per year of mantle-derived CO₂ is released in the Magadi-Natron Basin, at the border between Kenya and Tanzania. Seismicity at depths of 15 to 30 km implies that extensional faults in this region may penetrate the lower crust. We therefore suggest that CO₂ is transferred from upper mantle or lower crustal magma bodies along these deep faults. Extrapolation of our measurements to the entire Eastern rift of the rift system implies a CO₂ flux on the order of tens of megatons per year, comparable to emissions from the entire mid-ocean ridge system (Marty and Tolstikhin, 1998; Kagoshima et al., 2015) of 53 to 97 Mt yr⁻¹. We conclude that widespread continental rifting and super-continent breakup could produce massive, long-

term CO₂ emissions and contribute to prolonged greenhouse conditions like those of the Cretaceous.

2. INTRODUCTITON

Emissions of mantle-derived CO₂ are thought to be sourced primarily at volcanic centers, where it is currently estimated that ~90% of Earth's natural CO₂ is released through active degassing of volcanic plumes or passive, diffuse emissions around volcanic edifices, mid-ocean ridges, and volcanic lakes (Marty and Tolstikhin, 1998; Pérez et al., 2011; Burton et al., 2013; Kagoshima et al., 2015). One major source of discrepancy in global flux estimates relates to sparse sampling of diffuse CO₂ flux in fault systems away from volcanic centers (Seward and Kerrick, 1996). These areas of tectonic degassing (e.g., Apennines, Italy; Chiodini et al., 2004) exhibit high surface CO₂ fluxes sourced from deep magma bodies, yet have no expression of recently active volcanism (e.g., composite volcanoes or calderas, see Supplementary Information). Although magma-rich continental rifts (e.g., East African and Rio Grande rifts) represent prime targets to test and quantify this mode of CO₂ transfer, gross estimates of CO₂ flux within areas of tectonic degassing are currently restricted to only a few localities globally (Italy and Pacific Rim; Seward and Kerrick, 1996; Chiodini et al., 2004). Consequently, global CO₂ flux estimates from natural systems are likely underestimated (Seward and Kerrick, 1996).

The East African Rift (EAR) is the world's largest active continental rift, comprising distinct western and eastern sectors with a cumulative length of > 3,000 km (Ebinger and Scholz, 2012). Active volcanoes in the EAR emit large volumes of CO₂, such as

Nyiragongo ($\geq 3.4 \text{ Mt yr}^{-1}$; Sawyer et al., 2008) and Oldoinyo Lengai (2.42 Mt yr^{-1} ; Brantley and Koepenick, 1995), and significant amounts of CO_2 are stored in large anoxic lakes (e.g., Lake Kivu; Pasche et al., 2011). Fault systems dissecting active volcanic centers in the EAR (e.g., Aluto complex, Ethiopia) have been shown to provide local pathways through which CO_2 -rich fluids are transported from shallowly degassing magma chambers (Hutchison et al., 2015). However, earthquake swarms spanning the crustal depth range, interpreted as the release and rise of CO_2 -rich fluids through faults, are also observed in EAR basins away from active volcanic centers (e.g., Albertine basin; Lindenfeld et al., 2012). Despite these findings, no study has tested the volumetric capacity of rift-wide fault systems in the EAR to transport deeply-derived CO_2 . Here we provide strong evidence that significant volumes of CO_2 , likely sourced from upper mantle and/or lower crustal magma bodies, are emitted through fault systems positioned away from active volcanic centers in the EAR.

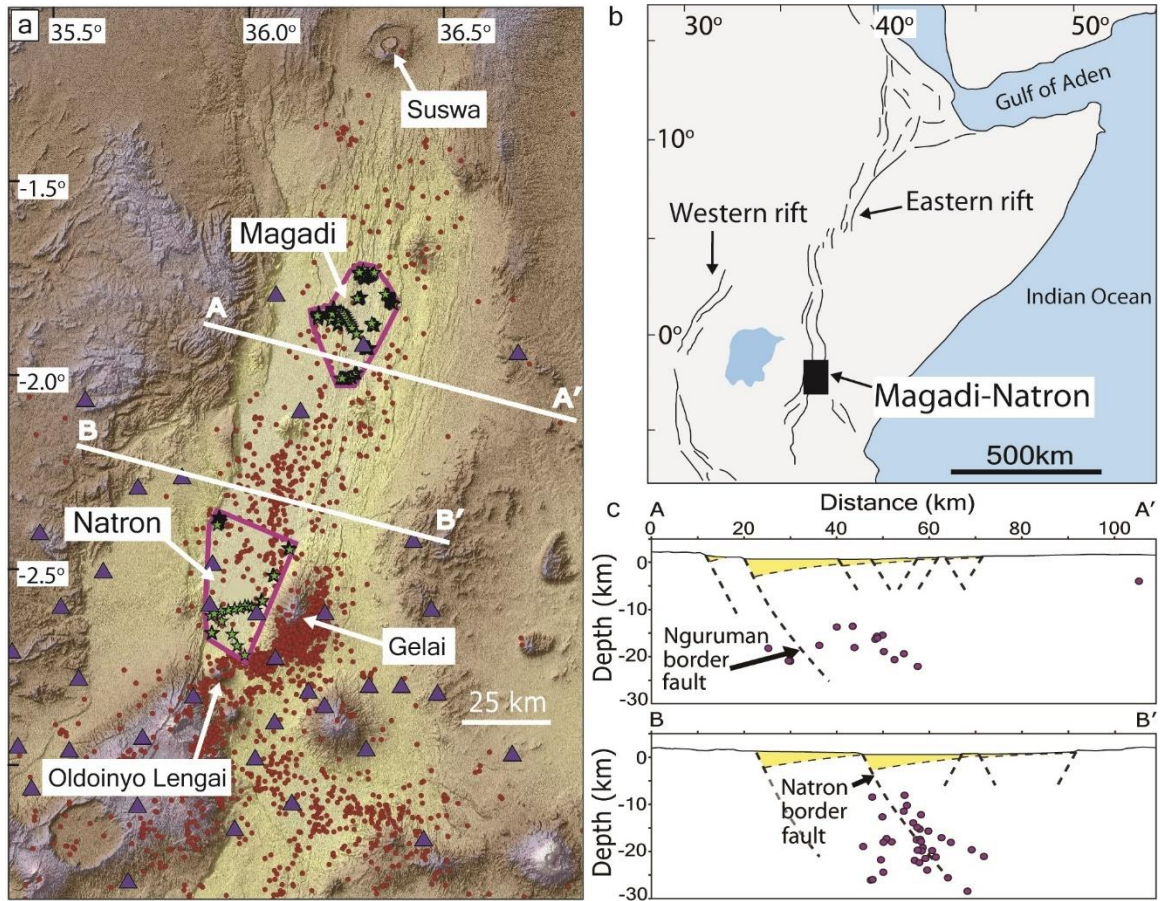


Figure 1. Distribution of CO₂ flux samples and seismicity. a, SRTM map of the Magadi-Natron basin. Active volcanic centers (Suswa, Gelai, and Oldoinyo Lengai) are annotated. Green stars show CO₂ measurements locations. Red circles show earthquake epicenters from the CRAFTI seismic network (purple triangles). b, Location of the study area. c, Cross-sections from A-A' and B-B' in (a). Purple circles represent earthquake foci 2 km from each section. Yellow fill represents basin sediments (Birt et al., 1997; Foster et al., 1997). Border faults are projected to lower crustal seismicity using surface and seismic observations.

3. METHODS

The volume of CO₂ released diffusively at any volcanic-tectonic setting can be estimated from soil CO₂ flux measurements, whereas CO₂ sources (mantle and/or biogenic, for example) may be characterized by carbon isotope compositions (Lewicki and Brantley, 2000; Chiodini et al., 2008). We investigated diffuse CO₂ emissions within fault populations in the Magadi-Natron basin at the Kenya-Tanzania border (Fig. 1 and Table 1). Diffuse CO₂ flux was measured with an accumulation chamber (Chiodini et al., 2008) at the base of fault scarps (termed here fault zones) and compared with background values in hanging walls and footwalls across horst and graben structures (see Supplementary Information). Gas samples were collected by diverting gas from the chamber into pre-evacuated glass vials during flux measurements (Parks et al., 2013). These samples were analyzed in the laboratory for $\delta^{13}\text{C-CO}_2$ and CO₂ concentrations, and compared with samples collected on Oldoinyo Lengai, an active volcano at the southern terminus of the Natron basin (Fig. 1a). Seismicity data were collected on the 38-station CRAFTI broadband seismic array.

3.1. CO₂ gas accumulation chamber method

The diffuse CO₂ flux survey was performed using the accumulation chamber method described in detail by ref. 31. We used an EGM-4 CO₂ Gas Analyzer (PP Systems), which has a cylindrical chamber with a volume of $1.18 \times 10^{-3} \text{ m}^3$, and an infra-red gas analyzer with a measurement range of 0 to 30,000 ppm and <1% error. For each field measurement, the accumulation chamber was pressed firmly into the ground (~2 cm deep) to form a tight

seal. Diffuse CO₂ flux was then calculated in the field based on changes in CO₂ concentration (ppm) through time over a 120 second time period.

3.2. Field sampling strategy

Owing to the large number of fault systems and eruptive centers in the 184 km-long, 50 km-wide Magadi-Natron basin system, we employed a modified version of the dense grid sampling approach for small sample areas (1-20 km²; Werner and Cardellini, 2006; Chiodini et al., 2008). In contrast to these studies, our analyses focused on understanding CO₂ flux with respect to the location of visible faults (see also Supplementary Information). Where access allowed, CO₂ flux measurements were taken along 500 m to 4,000 m-long transects either parallel or perpendicular to fault strike, with sample spacing varying between 20 m and 200 m depending on the length of the transect. In addition to targeting faults, broad transects (4,000 m to 20,000 m long) were taken across the Magadi and Natron basins, with sample spacing between 400 m and 4,000 m. In total, 565 flux measurements were taken over the 960 km² survey area during 18 days of field work in June and July, 2014.

3.3. Laboratory analyses of gas compositions and C isotopes

We collected 115 gas samples, each with an accompanying duplicate sample, for isotope analyses in the Magadi-Natron basin and on Oldoinyo Lengai volcano (Table S1 in Supplementary Information). CO₂ concentrations and $\delta^{13}\text{C}$ values were assessed using the method of ref. 15. A T-shaped connector, attached to the gas analyzer, was used to divert gas into pre-evacuated Labco 12 ml Borosilicate Vials during flux measurements. CO₂

concentrations in the vials were determined at the University of New Mexico (UNM) by a Gow-Mac series G-M 816 Gas Chromatograph (GC) and a Pfeiffer Quadrupole Mass Spectrometer (QMS), which has a mass range from 0 to 120 amu. The Volcanic and Geothermal Fluid Analysis Laboratory (UNM) has a combination system of GC and QMS that enables measurement of gas species at the same time. Relative abundances of CO₂, CH₄, H₂, Ar+O₂, N₂, and CO in the vials were measured on the GC using a He carrier gas. Gas species were separated on the GC using a Hayes Sep pre-column and 5Å molecular sieve columns. A discharge ionization detector was used for CO₂, CH₄, H₂, Ar+O₂, N₂ and CO, respectively (Giggenbach and Goguel, 1989). He, Ar, O₂, and N₂ in the vials were also analyzed for their relative abundances on the QMS with a secondary electron multiplier detector in dynamic mode. These data were processed using the Quadstar software, which corrects possible mass interferences (de Moor et al., 2013). Combining the data from GC and QMS, the relative abundances of CO₂, CH₄, H₂, Ar, O₂, N₂ and CO were acquired (see Supplementary Information). Our $\delta^{13}\text{C-CO}_2$ values were measured by Isotope Ratio Mass Spectrometer (Finnigan Delta XL) with a gas bench and auto-sampler at the Center for Stable Isotopes, UNM (see Supplementary Information). The $\delta^{13}\text{C-CO}_2$ values are presented as per mil (‰) against the standard, Pee Dee belemnite (PDB). Only $\delta^{13}\text{C-CO}_2$ values that have higher peak amplitudes of mass 44 (906 to 10,111mV) than blank tests (average of 805mV) were taken. Using the Oztech isotope ratio reference gas, the standard error of analyses is $\pm 0.2\text{‰}$ (1σ). All reported CO₂ data are presented in the main text and Supplementary Information.

3.4. Analysis of broadband seismic data

Continuous waveforms from the 38-station CRAFTI (Continental Rifting in Africa: Fluid-Tectonic Interaction) broadband seismic array and GEOFON stations KMBO and KIBK in Kenya were analyzed using the Seismic Handler Motif (SHM) program (Stammler, 1993) (Fig. S1). P- and S-wave arrival times were picked manually on Butterworth filtered (1-10 Hz) vertical and horizontal components. P phase arrival times were assigned quality factors of 0, 1, 2 or 3 according to estimated measurement errors of 0.05s, 0.1s, 0.15s, and 0.3s, respectively. S-wave quality factors of 0, 1, 2, and 3 were assigned to arrivals with estimated measurement errors of 0.1s, 0.175s, 0.25s, and 0.3s, respectively. Only events with a minimum of 6 phases, including at least 3 P-arrivals, were used in the locations; most events had 20 or more phases. The initial locations of earthquakes were found assuming the local velocity model of Albaric et al. (2010) and using a hypoinverse absolute location algorithm (Klein, 1978). Progressive GPS timing failures at 32 sites led to changing the network in January and February, 2013 and then a gap between March and January, 2014. Data used in this study (3,274 events) span January 13 to February 28, 2013, and December 15, 2013 to November 1, 2014. Excluding a few mine blast events and earthquakes at Oldoinyo Lengai volcano, earthquakes are tectonic with impulsive P- and S-arrivals and peak frequencies $> 5\text{Hz}$. Earthquakes presented along profiles A-A' and B-B' represent a small, representative proportion of Magadi-Natron data set, consistent with depth histograms of all Natron and Magadi basin earthquakes, which show significant populations at depths between 15 and 27 km (Fig. S2). A subset of these earthquakes was relocated using a 3D tomography model of the study area Roecker et al., (2015). Depth histograms for earthquakes in the Natron and Magadi basins (excluding Gelai

volcano) and those relocated from the 3D tomography model show no systematic variations (Fig. S2). The same earthquakes were re-located using the double difference algorithm of Waldhauser and Ellsworth (2000). Double difference locations for earthquakes along A-A' and B-B' have formal position errors of ≤ 1.5 km and depth errors ≤ 3.9 km determined by singular value decomposition (errors increase with depth), with additional but small errors associated with 3D velocity variations. Local magnitudes range between 1 and 4.5.

Table 1. CO₂ fluxes, mean CO₂ concentrations and δ¹³C from the Magadi-Natron basin.

		area (km ²)	mean flux (g m ⁻² d ⁻¹)	total flux (t d ⁻¹)	annual flux (Mt yr ⁻¹)	CO ₂ (ppm)	δ ¹³ C-CO ₂ (‰ vs. PDB)
Magadi	Fault zones	72.9	36.6 ± 11.0	2,672 ± 804	0.98 ± 0.29	1,056 ± 581	-7.8 ± 1.3
	Background§	334.6	4.9 ± 1.9	1,650 ± 649	0.61 ± 0.24	789 ± 209	-8.1 ± 1.4
	Sum	407.5		4,327 ± 1453	1.59 ± 0.53		
Natron	Fault zones	33.1	17.2 ± 5.0	570 ± 166	0.21 ± 0.06	944 ± 158	-8.1 ± 2.0
	Background§	540.9	11.4 ± 6.6	6,176 ± 3592	2.25 ± 1.31	837 ± 108	-8.5 ± 1.3
	Sum	574.0		6,746 ± 3758	2.46 ± 1.37		
Total		981.5			4.05 ± 1.90	929 ± 386	-8.0 ± 1.3

Fluxes are ± 95% confidence. Mean values of CO₂ concentrations and δ¹³C are ± 1σ.

Fault zones occur adjacent to fault scarps, extending outward on the downthrown side a distance equal to the maximum throw. Faults were mapped from aerial photos and throws were estimated using a measured throw/length ratio of 0.0061. Background values represents the combined CO₂ flux from hanging walls (downthrown sediments) and footwalls (uplifted lavas) measured from aerial photos and LandSat imagery, and validated in the field. See also Supplementary Information (Fig. S1 and Table S3).

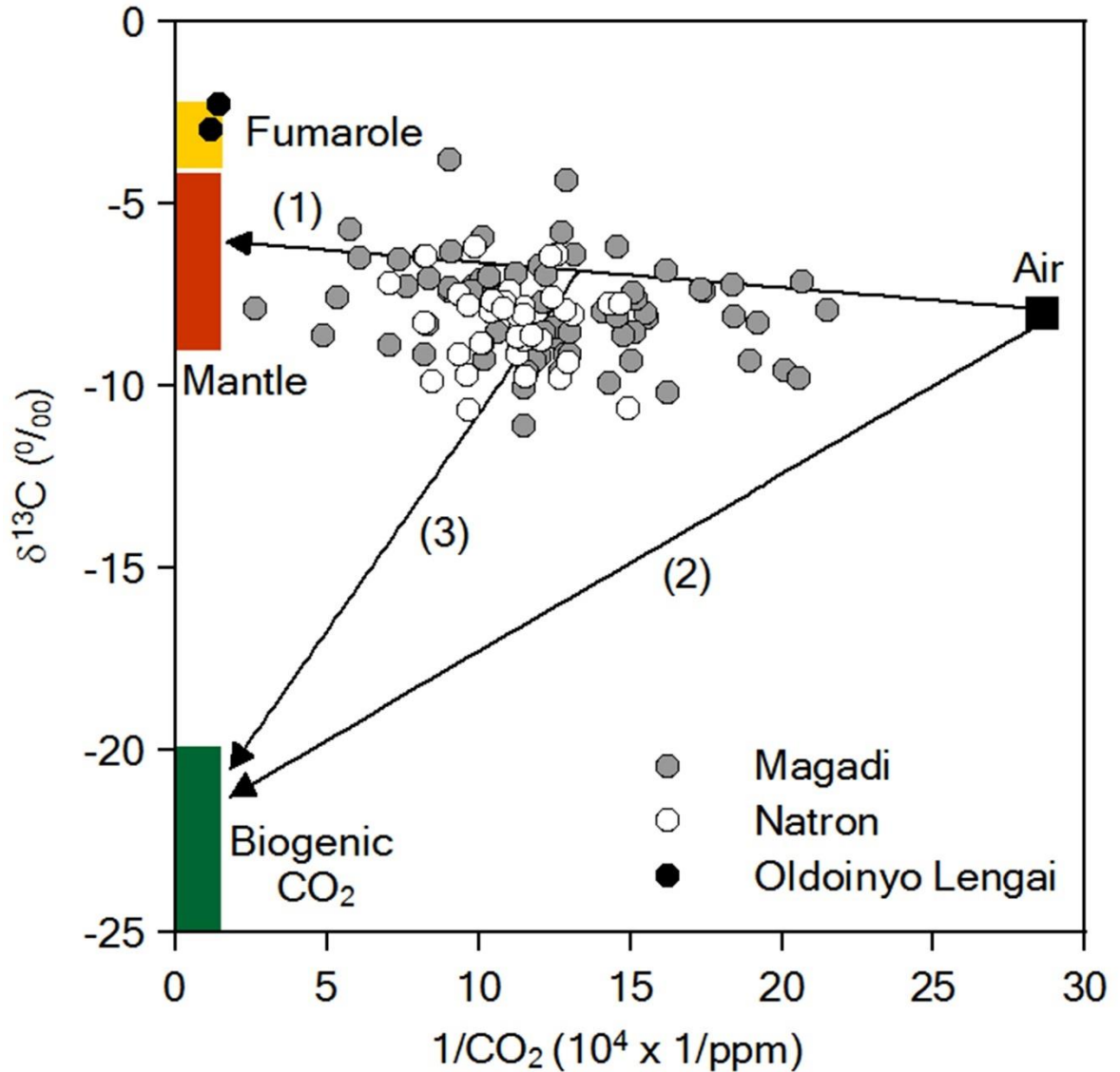


Figure 2. Carbon isotope compositions and concentrations of diffuse CO_2 in the Magadi-Natron basin. $\delta^{13}\text{C}$ - CO_2 vs the reciprocal of CO_2 concentration ($\times 10^4$). Mantle $\delta^{13}\text{C}$ values (red box) are -6.5 ± 2.5 ‰ (Sano and Marty, 1995). $\delta^{13}\text{C}$ values of fumaroles (yellow bar) are from Fischer et al. (2009). Biogenic CO_2 (green bar) ranges from -20 ‰ to -25 ‰ of $\delta^{13}\text{C}$ (ref. 14). Values for air (Lewicki and Brantley, 2000) are represented by the black square. Arrows show mixing lines between mantle and air (1), biogenic CO_2 and air (2), and mixtures of mantle/air and biogenic CO_2 (3).

4. RESULTS AND DISCUSSION

Carbon isotope compositions indicate a strong mantle contribution to the observed CO₂ (Fig. 2). Measured $\delta^{13}\text{C-CO}_2$ values range from -3.8 to -11.7‰ with a mean value of -8.0 ± 1.3 ‰ (Table 1), and 78% of values fall within the mantle range (-6.5 ± 2.5 ‰; Sano and Marty, 1995). All $\delta^{13}\text{C-CO}_2$ values are distinctively heavier than biogenic $\delta^{13}\text{C}$ values from soil CO₂ studies along transform plate boundaries elsewhere, such as the San Andreas fault (-21.6‰ to -23.7‰; Lewicki and Brantley, 2000). Although two samples have similar $\delta^{13}\text{C-CO}_2$ values (-3.8‰ and -4.3‰, respectively) to fumaroles on Oldoinyo Lengai volcano (-2.36‰ to -4.01‰; Fischer et al., 2009), they are within the range of isotope values from mantle-derived CO₂ collected in volcanic and geothermal areas in the Kenya rift (-1.7‰ to -6.9‰; Darling et al., 1995). CO₂ concentrations of our samples (< 0.4%; Table S1) are lower than typical magmatic and hydrothermal gases (0.5%-11.9%; Fischer and Chiodini, 2015), which may be attributed to dilution of mantle-derived CO₂ by air during diffuse degassing (Fig. 2). For example, following the approach of ref. 15, plots of $\delta^{13}\text{C}$ and CO₂ concentrations fit on a mantle-air mixing line (Fig. 2). Samples with lighter $\delta^{13}\text{C}$ values (< -9‰) are possibly affected by minor contributions of biogenic CO₂ to a predominantly mantle-derived CO₂ and air mixture.

An elevated CO₂ flux in fault zones of the Magadi-Natron basin (Table 1; Fig. 3) provides strong evidence that faults act as permeable pathways that facilitate the ascent of the deeply-derived CO₂ (see also Supplementary Information). Mean values of diffuse CO₂ flux in fault zones of the Magadi and Natron study areas (36.6 ± 11.0 g m⁻² d⁻¹ and 17.2 ± 5.0 g m⁻² d⁻¹, respectively) are higher than background values in graben sediments and uplifted

rift lavas (Table 1). The highest individual CO₂ flux measurements (up to 533.5 g m⁻² d⁻¹) occur along large faults (throws >150 m), which occasionally exhibit aligned hot springs along them (Fig. 3a). Some of these large faults bound the >2-km-deep rift basins (Birt et al., 1997; Foster et al., 1997) and are underlain by lower crustal earthquake swarms (Fig. 1).

Diffuse CO₂ flux from tectonic degassing in the Magadi and Natron basin study areas equates to estimated CO₂ outputs of 1.59±0.53 Mt yr⁻¹ and 2.46±1.37 Mt yr⁻¹, respectively (Table 1) (see Supplementary Information). These values represent tectonic degassing of mantle-derived CO₂ through fault systems away from active volcanic centers, and thus omit CO₂ flux values from volcanoes at the northern (Suswa) and southern (Oldoinyo Lengai) extents of the Magadi-Natron basin. The combined study area represents only ~10% of the entire 9,200 km², pervasively faulted basin area; therefore, our flux values represent a conservative minimum estimate for the basin. Despite this cautious approach, the total CO₂ flux from tectonic degassing along fault systems in the Magadi-Natron basin is an order of magnitude greater than the mean diffuse CO₂ flux of reported historically active volcanoes (0.21 Mt yr⁻¹; Burton et al., 2013) (Fig. S3). We acknowledge, however, that diffuse CO₂ flux occurs passively over wide areas, and thus CO₂ contributions from diffuse degassing at many volcanoes may be underestimated as a result of sparse sampling and the large study areas required to accurately constrain flux.

CO₂ is extracted from the mantle by the generation and ascent of magma. It exsolves from magma during cooling, crystallization, and decompression. Where extensional fracture systems exist, as in rift zones, exsolved CO₂ has a permeable network through which it

may rise to the surface (Reyners et al., 2007; Lindenfeld et al., 2012; Burton et al., 2013). Seismic and magnetotelluric studies provide evidence for volumetrically significant accumulations of magma trapped within the crust and upper mantle beneath the Eastern rift (Birt et al., 1997; Keranen et al., 2004). These magma bodies provide the likely source for massive CO₂ emissions. Although CO₂ in the Magadi-Natron basin may in part be sourced by upper crustal dikes (Calais et al., 2008), the flux of CO₂ is significant, and requires degassing from the large magma volumes in the crust and mantle (see also Supplementary Information). The association of mantle-derived CO₂ and fault zones provides compelling evidence that CO₂ released from these intrusions into rift-wide fault systems rivals degassing at rift volcanoes. These assertions are further supported by lower crustal earthquakes in the region, which are shown at some rift settings to represent the transport of volatiles exsolved from upper mantle (Reyners et al., 2007; Lindenfeld et al., 2012) and/or lower crustal intrusions (Keir et al., 2009). Well-located seismicity occurs at depths of 15-27 km (Fig. S2) and in some instances can be projected along subsurface border faults (Albaric et al., 2014) (Fig. 1). Steep, rift-parallel zones of lower crustal to near-surface earthquakes beneath the central Magadi and Natron basins may also mark zones of repeated dike intrusion within incipient magmatic segments (e.g., Keranen et al., 2004) (Fig. 1), providing a potential source for massive CO₂ emissions through rift-wide fault systems.

Although CO₂ flux from tectonic degassing in the Magadi-Natron basin may be higher than other sectors, the growing evidence of CO₂ degassing from even the magma-poor Albertine system (Lindenfeld et al., 2012) suggests the process may apply to other EAR

basins. These considerations imply that faults in the EAR likely contribute a significant portion of CO₂ to the global budget. We provide first-order estimates of the total CO₂ flux from tectonic degassing in the Eastern rift using flux measurements from the Magadi-Natron basin (see also Supplementary Information). The ~184 x 50 km Magadi-Natron basin emits a minimum of 4.05±1.90 Mt yr⁻¹ of diffuse CO₂ over its areal extent (Table 1), equating to a mean 4.4 x 10² t km⁻² yr⁻¹. If we applied this flux to the 3,240 x 50 km Eastern rift⁷, we would obtain a value of 71±33 Mt yr⁻¹ of CO₂, which could potentially increase the global flux from natural systems (637 Mt yr⁻¹; Burton et al., 2013) by 11% to 708 Mt yr⁻¹. Although this total CO₂ flux represents only degassing along fault systems away from volcanic centers, it is still of the same order as the total CO₂ output from mid-ocean ridges (53-97 Mt yr⁻¹; Marty and Tolstikhin, 1998; Kagoshima et al., 2015). The significance of these flux estimates highlights the important contributions of the East African Rift to the deep carbon cycle, as well as the potential role of deeply-derived fluids in assisting rift processes generally (e.g., lower crustal faulting; Lindenfeld et al., 2012; Albaric et al., 2014). However, further diffuse CO₂ surveys across fault systems in Tanzania, Kenya and Ethiopia are required to test whether our flux estimates can be confidently applied to the entire Eastern rift.

Understanding the causes of atmospheric CO₂ variations over geologic timescales is important for reconstructing Earth's climate. For example, baseline greenhouse conditions of the Cretaceous to early Paleogene were characterized by 4-8 times higher *p*CO₂ than the Holocene, requiring a 2-2.8 times increase in global CO₂ input to the atmosphere (Lee et al., 2013). The exact cause of this increase is poorly constrained, although it has been

linked previously to increased rates in arc and/or flood basalt volcanism (Kidder and Worsley, 2010; Lee et al., 2013). Our CO₂ emission estimates (tens of Mt yr⁻¹) from tectonic degassing in the EAR show that long-lived (> 5 Myr), magma-assisted rifting could produce 10⁴ Gt Myr⁻¹ of CO₂, after an initial spike of ~1 Gt yr⁻¹ associated with flood basalt eruptions (Courtillot et al., 1999; Self et al., 2006). During the Cretaceous and Paleogene, widespread flood basalt volcanism and continental breakup events occurred in association with the Greenland (60-53 Ma), Deccan (65-60 Ma), and Parana (138-125 Ma) large igneous provinces (Courtillot et al., 1999). Based on our estimates, each of these rifting events would be the equivalent of doubling current mid-ocean ridge CO₂ emissions and releasing 10⁴ Gt Myr⁻¹ of greenhouse gases over the lifetime of rifting. Although this may not be sufficient to achieve the required 4-8 times increase in atmospheric CO₂ compared to the Holocene, widespread continental rift formation, like the recently proposed ubiquitous continental arc volcanism (Lee et al., 2013), provides a compelling and previously unquantified source of massive, long-term CO₂ input to the atmosphere.

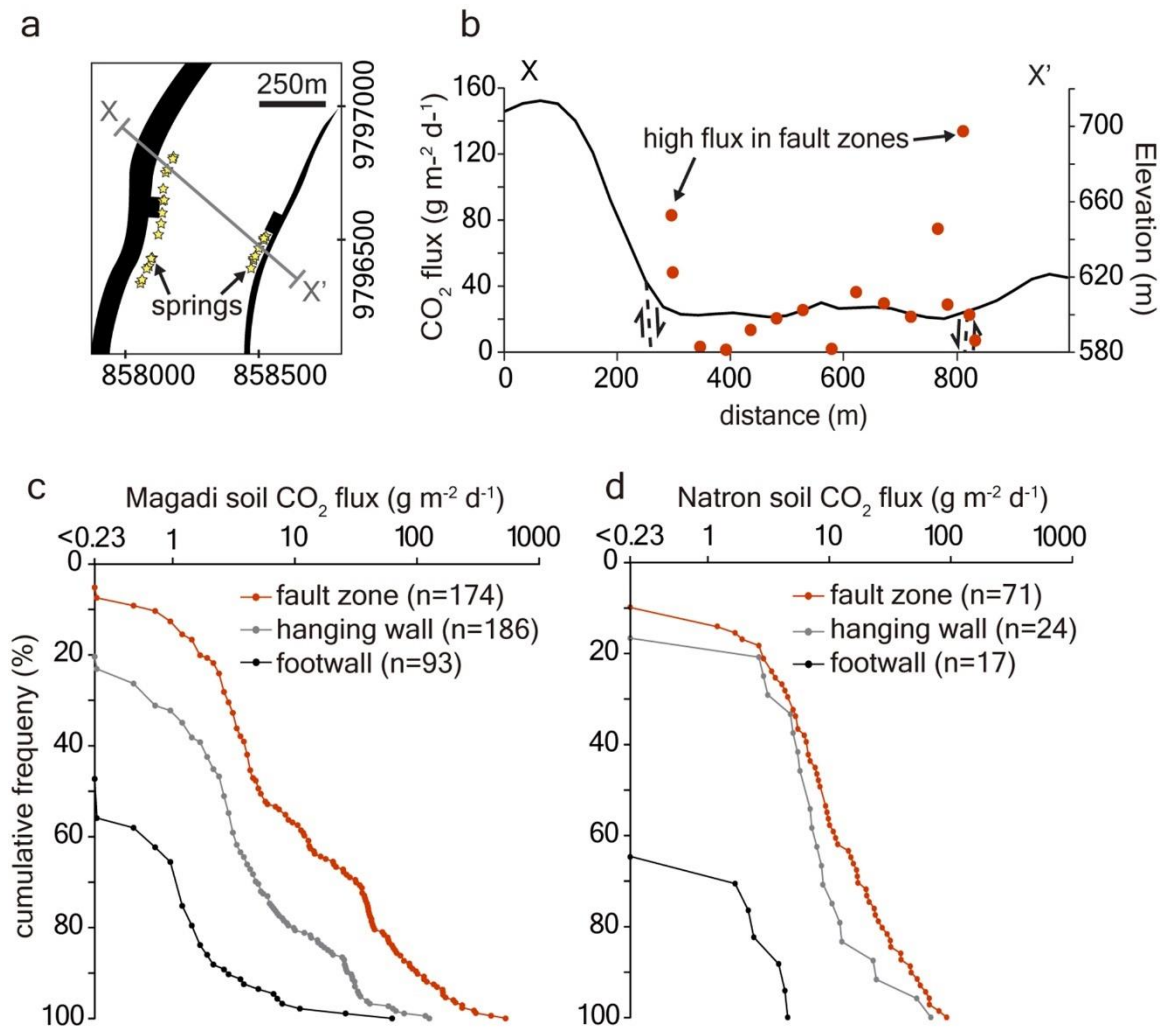


Figure 3. Summary of CO₂ fluxes throughout the Magadi-Natron basin. a, Simplified structural map of a faulted graben in Magadi basin. Black lines represent faults and yellow stars the location of springs. b, Cross-section (X-X' in a) showing the distribution of CO₂ flux (red circles). c & d, Cumulative frequency plots of diffuse CO₂ flux from all transects across faulted grabens in the study area. Hanging wall represents downthrown sediments, footwalls are uplifted lavas, and fault zones occur adjacent to fault scarps, extending outward on the downthrown side a distance equal to the maximum throw (refer to Supplementary Information).

5. REFERENCES

- Albaric, J., Déverchère, J., Perrot, J., Jakovlev, A., and Deschamps, A. (2014) Deep crustal earthquakes in North Tanzania, East Africa: interplay between tectonic and magmatic processes in an incipient rift. *Geochem. Geophys. Geosyst.* **15**, 374–394.
- Albaric, J., Perrot, J., Déverchère, J., Deschamps, A., Le Gall, B., Ferdinand, R. W., Tiberi, C., Sue, C., and Songo, M. (2010) Contrasted seismogenic and rheological behaviours from shallow and deep earthquake sequences in the North Tanzanian Divergence, East Africa. *J. Afr. Earth Sci.* **58**, 799–811.
- Birt, C. S., Maguire, P. K. H., Khan, M. A., Thybo, H., Keller, G. R., and Patel, J. (1997) The influence of pre-existing structures on the evolution of the southern Kenya rift valley – Evidence from seismic and gravity studies. *Tectonophysics* **278**, 211–242.
- Brantley, S. L. and Koepnick, K. W. (1995) Measured carbon dioxide emissions from Oldoinyo Lengai and the skewed distribution of passive volcanic fluxes. *Geology* **23**, 933–936.
- Burton, M. R., Sawyer, G. M., and Granieri, D. (2013) Deep carbon emission from volcanoes. *Rev. Mineral. Geochem.* **75**, 323–354.

- Calais, E., d Oreye, N., Albaric, J., Deschamps, A., Delvaux, D., Deverchere, J., Ebinger, C., Ferdinand, R.W., Kervyn, F., Macheyeke, A.S., Oyen, A., Perrot, J., Saria, E., Smets, B., Stamps, D.S., and Wauthier, C. (2008) Aseismic strain accommodation by slow slip and dyking in a youthful continental rift, East Africa. *Nature* **456**, 783-787.
- Chiodini, G., Cioni, R., Guidi, M., Raco, B., and Marini, L. (1998) Soil CO₂ flux measurements in volcanic and geothermal areas. *Appl. Geochem.* **13**, 543–552.
- Chiodini, G., Cardellini, C., Amato, A., Boschi, E., Caliro, S., Frondini, F., and Ventura, G. (2004) Carbon dioxide Earth degassing and seismogenesis in central and southern Italy. *Geophys. Res. Lett.* **31**, L07615.
- Chiodini, G., Caliro, S., Cardellini, C., Avino, R., Granieri, D., and Schmidt, A. (2008) Carbon isotopic composition of soil CO₂ efflux, a powerful method to discriminate different sources feeding soil CO₂ degassing in volcanic hydrothermal areas. *Earth Planet. Sci. Lett.* **274**, 372–379.
- Courtillot, V., Jaupart, C., Manighetti, I., Tapponnier, P., and Besse, J. (1999) On causal links between flood basalts and continental breakup. *Earth Planet. Sci. Lett.* **166**, 177–195.
- Darling, W. G., Greisshaber, E., Andrews, J. N., Armannsson, H., and O'Nions, R. K. (1995) The origin of hydrothermal and other gases in the Kenya Rift Valley. *Geochim. Cosmochim. Acta.* **59**, 2501–2512.

- de Moor, J. M. Fischer, T. P., Sharp, Z. D., Hilton, D. R., Barry, P. H., Mangasini, F., and Ramirez, C. (2013) Gas chemistry and nitrogen isotope compositions of cold mantle gases from Rungwe Volcanic Province, southern Tanzania. *Chem. Geol.* **339**, 30–42.
- Ebinger, C. J. and Scholz, C. A. (2012) Continental Rift Basins: The East African Perspective. in *Tectonics of sedimentary basins: recent advances Ch. 9* (eds. Busby, C. & Azor, A.) (John Wiley & Sons, Chichester, UK).
- Fischer, T. P. and Chiodini, G. (2015) Volcanic, magmatic and hydrothermal gases. in *The encyclopedia of volcanoes, Ch. 45* (eds. Sigurdsson, H., Houghton, B., McNutt, S., Rymer, H., & Stix, J.) (Academic Press, San Diego, USA).
- Fischer, T. P., Burnard, P., Marty, B., Hilton, D. R., Furi, E., Palhol, F., Sharp, Z. D., and Mangasini, F. (2009) Upper mantle volatile chemistry at Oldoinyo Lengai volcano and the origin of carbonatites. *Nature* **459**, 77–80.
- Foster, A., Ebinger, C., Mbede, E., and Rex, D. (1997) Tectonic development of the northern Tanzanian sector of the east African rift system. *J. Geol. Soc.* **154**, 689–700.
- Giggenbach, W. F. and Goguel, R. L. (1989) Methods for the collection and analysis of geothermal and volcanic water and gas samples. *Tech. Rep. CD2387, Dept. Scient. Indust. Res., Petone, New Zealand.*
- Hutchison, W., Mather, T. A., Pyle, D. M., Biggs, J., and Yirgu, G. (2015) Structural controls on fluid pathways in an active rift system: A case study of the Aluto volcanic complex. *Geosphere* **11**, 542-562.

- Kagoshima, T., Sano, Y., Takahata, N., Maruoka, T., Fischer, T.P., and Hattori, K. (2015) Sulphur geodynamic cycle. *Sci. Rep.* **5**, 8330.
- Keir, D., Bastow, I. D., Whaler, K. A., Daly, E., Cornwell, D. G., and Hautot, S. (2009) Lower crustal earthquakes near the Ethiopian rift induced by magmatic processes. *Geochem. Geophys. Geosyst.* **10**, Q0AB02.
- Keranen, K., Klempere, S., and Gloaguen, R. (2004) EAGLE Working Group, Three dimensional seismic imaging of a proto-ridge axis in the Main Ethiopian Rift, *Geology* **39**, 949–952.
- Kidder, D. L. and Worsley, T. R. (2010) Phanerozoic Large Igneous Provinces (LIPs), HEATT (Haline Euxinic Acidic Thermal Transgression) episodes, and mass extinctions. *Palaeogeogr. Palaeoclimatol. Palaeoecol.* **295**, 162–191.
- Klein, F. W. (1978) Hypocenter location program HYPOINVERSE. *Tech. Rep. 78-698*, U.S. Geol. Surv..
- Lee, C.-T. A., Shen, B., Slotnick, B.S., Liao, K., Dickens, G.R., Yokoyama, Y., Lenardic, A., Dasgupta, R., Jellinek, M., Lackey, J.S., Schneider, T., and Tice, M.M. (2013) Continental arc–island arc fluctuations, growth of crustal carbonates, and long-term climate change. *Geosphere* **9**, 1–36.
- Lewicki, J. L. and Brantley, S. L. (2000) CO₂ degassing along the San Andreas fault, Parkfield, California. *Geophys. Res. Lett.* **27**, 5–8.
- Lindenfeld, M., Rumpker, G., Link, K., Koehn, D., and Batte, A. (2012) Fluid-triggered earthquake swarms in the Rwenzori region, East African Rift - evidence for rift initiation. *Tectonophysics* **566**, 95-104.

- Marty, B. and Tolstikhin, I. N. CO₂ fluxes from mid-ocean ridges, arcs and plumes. *Chem. Geol.* **145**, 233–248 (1998).
- Parks, M.M., Caliro, S., Chiodini, G., Pyle, D.M., Mather, T.A., Berlo, K., Edmonds, M., Biggs, J., Nomikou, P., and Raptakis, C. (2013) Distinguishing contributions to diffuse CO₂ emissions in volcanic areas from magmatic degassing and thermal decarbonation using soil gas ²²²Rn–δ¹³C systematics: application to Santorini volcano, Greece. *Earth Planet. Sci. Lett.* **377–378**, 180–190.
- Pasche, N., Schmid, M., Vazquez, F., Schubert, C.J., Wuest, A., Kessler, J.D., Pack, M.A., Reeburgh, W.S., and Burgmann, H. (2011) Methane sources and sinks in Lake Kivu, *J. Geophys. Res.* **116**, G03006.
- Pérez, N.M., Hernández, P.A., Padilla, G., Nolasco, D., Barrancos, J., Melían, G., Padrón, E., Dionis, S., Calvo, D., Rodríguez, F., Notsu, K., Mori, T., Kusakabe, M., Arpa, C., Reniva, P., and Ibarra, M. (2011) Global CO₂ emission from volcanic lakes. *Geology* **39**, 235–238.
- Reyners M., Eberhart-Phillips, D., and Stuart, G. (2007) The role of fluids in lower-crustal earthquakes near continental rifts. *Nature* **446**, 1075–1079.
- Roecker, S. W., Ebinger, C. J., Tiberi, C., Mulibo, G. D., Ferdinand-Wambura, R., Muzuka, A., Khalfan, M., Gautier, S., Albaric, J., and Peyrat, S. (2015) Images of the East Africa Rift System from the Joint Inversion of Body Waves, Surface Waves, and Gravity: Investigating the Role of Magma in Early-Stage Continental Rifting. *Am. Geophys. Union Fall Meeting*, T51G-3013.
- Sano, Y. and Marty, B. (1995) Origin of carbon in fumarolic gas from island arcs. *Chem. Geol.* **119**, 265–274.

- Sawyer, G. M., Carn, S. A., Tsanev, V. I., Oppenheimer, C., and Burton, M. R. (2008) Investigation into magma degassing at Nyiragongo volcano, Democratic Republic of the Congo. *Geochem. Geophys. Geosyst.* **9**, Q02017.
- Self, S., Widdowson, M., Thordarson, T., and Jay, A. E. (2006) Volatile fluxes during flood basalt eruptions and potential effects on the global environment: a Deccan perspective. *Earth Planet. Sci. Lett.* **248**, 518–532.
- Seward, T. M., and Kerrick, D. M. (1996) Hydrothermal CO₂ emission from the Taupo Volcanic Zone, New Zealand. *Earth Planet. Sci. Lett.* **139**, 105–113.
- Stammler, K. (1993) SeismicHandler - programmable multichannel data handler for interactive and automatic processing of seismological analysis. *Comp. Geosci.* **19**, 135–140.
- Waldhauser, F. and Ellsworth, W. A. (2000) double-difference earthquake location algorithm: Method and application to the northern Hayward fault, California. *Bull. Seism. Soc. Amer.* **90**, 1353-1368.
- Werner, C. and Cardellini, C. (2006) Comparison of carbon dioxide emissions with fluid upflow, chemistry, and geologic structures at the Rotorua geothermal system, New Zealand. *Geothermics* **35**, 221–238.

CHAPTER 3

INCIPIENT RIFTING ACCOMPANIED BY THE RELEASE OF SUBCONTINENTAL LITHOSPHERIC MANTLE VOLATILES IN THE MAGADI AND NATRON BASIN, EAST AFRICA

Citation: Lee, H., Fischer, T.P., Muirhead, J.D., Ebinger, C.J., Kattenhorn, S.A., Sharp, Z.D., Kianji, G., Takahata, N., and Sano, Y. (2017). Incipient rifting accompanied by the release of subcontinental lithospheric mantle volatiles in the Magadi and Natron basin, East Africa. *Journal of Volcanology and Geothermal Research* (In press).

1. ABSTRACT

Geochemical investigations of volatiles in hydrothermal systems are used to understand heat sources and subsurface processes occurring at volcanic-tectonic settings. This study reports new results of gas chemistry and isotopes (O, H, N, C, and He) of thermal spring samples ($T = 36.8 - 83.5^{\circ}\text{C}$; $\text{pH} = 8.5 - 10.3$) from the Magadi and Natron basin (MNB) in the East African Rift (EAR). Although a number of thermal springs are shown to ascend along normal faults and feed into major lakes (Magadi, Little Magadi, and Natron), volatile sources and fluxes of these fluids are poorly constrained. CO_2 is the most abundant phase (up to 996.325 mmol/mol), and the N_2 -He-Ar abundances show a mixture of dissolved gases from deep (mantle-derived) and shallow (air/air saturated water) sources. The H_2 -Ar- CH_4 - CO_2 geothermometers indicate that equilibrium temperatures range from ~ 100 to $\sim 150^{\circ}\text{C}$. $\delta^{18}\text{O}$ (-4.4 to -0.2‰) and δD (-28.9 to -3.9‰) values of the MNB thermal waters still lie slightly to the right of the local meteoric water lines, reflecting minor evaporation. Each mixing relationship of N_2 ($\delta^{15}\text{N} = -1.5$ to 0.4‰; $\text{N}_2/{}^3\text{He} = 3.92 \times 10^6 - 1.33 \times 10^9$, except for an anomalous biogenic sample ($\delta^{15}\text{N} = 5.9\text{‰}$)) and CO_2 ($\delta^{13}\text{C} = -5.7$ to 1.6‰; $\text{CO}_2/{}^3\text{He} = 7.24 \times 10^8 - 1.81 \times 10^{11}$) suggests that the predominant mantle component of

the MNB volatiles is Subcontinental Lithospheric Mantle (SCLM). However, N₂ is mostly atmospheric, and minor CO₂ is contributed by the limestone end-member. ³He/⁴He ratios (0.64 - 4.00 Ra) also indicate a contribution of SCLM (R/Ra = 6.1 ± 0.9), with radiogenic ⁴He derived from a crustal source (R/Ra = 0.02). The MNB ⁴He flux rates (3.64 x 10¹¹ to 3.34 x 10¹⁴ atoms/m² sec) are significantly greater than the reported mean of global continental flux values (4.18 x 10¹⁰ atoms/m² sec), implying that magma intrusions could supply mantle ⁴He, and related heating and fracturing release crustal ⁴He from the Tanzanian craton and Mozambique belt. Total flux values (mol/yr) of ³He, N₂, and CO₂ are 8.18, 4.07 x 10⁷, and 5.31 x 10⁹, which are 1.28%, 2.04%, and 0.24% of global fluxes, respectively. Our results suggest that the primary source of magmatic volatiles in the MNB is SCLM, with additional crustal contributions, which is different from the KRV volatiles that have more asthenospheric mantle components. Volatiles from SCLM in magmas stall in the crust to heat and fracture country rock, with accompanying crustal volatile release. These volatile signatures reveal that MORB-type mantle replaces a relatively small volume of SCLM during incipient rifting (<10 Ma) in the EAR.

2. INTRODUCTION

Magmatic volatile percolation plays a key role in assisting continental rifting processes. Recent studies illustrate the potential for massive volatile fluxes at magma-rich settings like the East African Rift (EAR), highlighting continental rifts as significant contributors to Earth's carbon cycle (Lee et al., 2016). Additionally, volatile release is inferred to initiate swarms of earthquake activity in the lower crust (Reyners et al., 2007; Lindenfeld et al., 2012; Albaric et al., 2014), and localize upper crustal strain as continental rifts evolve to

sea-floor spreading ridges (Muirhead et al., 2016). Constraining the sources, transport mechanism, and volumetric fluxes of magmatic volatiles at continental rift settings therefore provides important insights into how continental rifting initiates and evolves.

Geochemistry and isotopes of volatiles (N₂, CO₂, and He) from volcanic and hydrothermal systems allow tracing of their sources in the Earth system (Sano and Fischer, 2013; Fischer and Chiodini, 2015). Active volcanism is the primary source of volatile emissions to the atmosphere, via volcanic eruption and diffuse degassing (Burton et al., 2013). Mantle-derived volatiles are also transported by fluids along extensional and compressional faults which are known as permeable pathways through the ductile-brittle transition zone (Kennedy et al., 1997; Kennedy and van Soest, 2007; Lee et al., 2016). In the East African rift (EAR), a number of currently active volcanoes (e.g., Erta Ale, Nyiragongo, Nyamuragira, and Oldoinyo Lengai) are emitting volatiles (Sawyer et al., 2008a, b; Fischer et al., 2009; de Moor et al., 2013). The EAR hydrothermal areas also release mantle-derived volatiles, which have been reported at the Lake Kivu, Kenya rift valley (KRV), and Rungwe regions (Darling et al., 1995; Tedesco et al., 2010; Barry et al., 2013; de Moor et al., 2013). Helium isotope ratios indicate mantle plume components in the Afar, Ethiopian, and Rungwe areas ($^3\text{He}/^4\text{He} = 9 - 20 \text{ Ra}$; Marty et al., 1996; Hilton et al., 2011; Darrah et al., 2013), yet no mantle plume signature is observed in other parts of the EAR such as the Kivu and KRV regions (e.g., Darling et al., 1995; Tedesco et al., 2010; Fischer et al., 2009). Despite these findings the sources and fluxes of volatiles from hydrothermal systems along much of the > 3,000 km-long EAR are yet to be investigated.

The present study focuses on the sources and fluxes of volatiles from hydrothermal systems in the Magadi-Natron basin (MNB) at the border of Kenya and Tanzania (Fig. 1).

Although volatile geochemistry has been reported previously for the area (Crane, 1981; Crane and O'Connell, 1983; Barry et al., 2013; Lee et al., 2016; Muirhead et al., 2016), little is currently known about possible volatile sources for the MNB hydrothermal system, because geochemistry and isotopes of dissolved gases (N₂, CO₂, and He) in the MNB thermal springs have not been investigated nor have fluxes of volatiles transported by hydrothermal systems been studied in detail. Here, we report results of gas chemistry, isotope compositions, and fluxes of volatiles from thermal spring samples in order to constrain volatile sources and fluxes through the MNB. In addition, this study first reports nitrogen isotope values of the KRV samples as well as contents of H₂S, HF, and HCl, which provide insights into better understanding of volatile sources and processes in the KRV.

3. REGIONAL SETTING

The EAR is the largest and most active continental rift in the world, extending from Afar to Mozambique (>3,000km), and bifurcating into western and eastern rifts (Ebinger and Scholz, 2012). Although related volcanism in the eastern rift is oldest at its northern extent in Afar (~30-45Ma; Baker, 1987; Ebinger et al., 1989; George et al., 1998; Nyblade and Brazier, 2002), rifting is thought to have initiated at ~25Ma in both the Afar and Lake Turkana regions (Ebinger et al., 2000). The youngest basins in the eastern rift occur in the south, where it reaches the Archean Tanzanian craton in northern Tanzania (Foster et al., 1997; Le Gall et al., 2008; Macheyeke et al., 2008). By comparison, the western rift, composed of the Toro-Ankolean, Virunga, Kivu, Mwenga-Kamituga, and Rungwe provinces, initiated after the eastern rift, with basins dated between 24 and 1 Ma (Ebinger, 1989; Pasteels et al., 1989; Kampunzu et al., 1998; Roberts et al., 2012).

Current models for rift development in the eastern rift suggest that, during the earliest stage of continental rifting (< 10 Ma), a relatively small volume of the stretched and heated subcontinental lithospheric mantle (SCLM) is replaced by the asthenosphere, accompanied by decompression melting and release of magmatic fluids, making the overlying lithosphere thinner and hotter (Ebinger, 2005; Corti, 2009). As rifting process continued, the asthenosphere rose upward and decompression melting occurred, leading to volumetric increase in volcanism. Magmatism accommodated a larger proportion of the plate boundary strain, finally resulting in the formation of sea-floor spreading ridges (e.g., Buck, 2004; Ebinger, 2005).

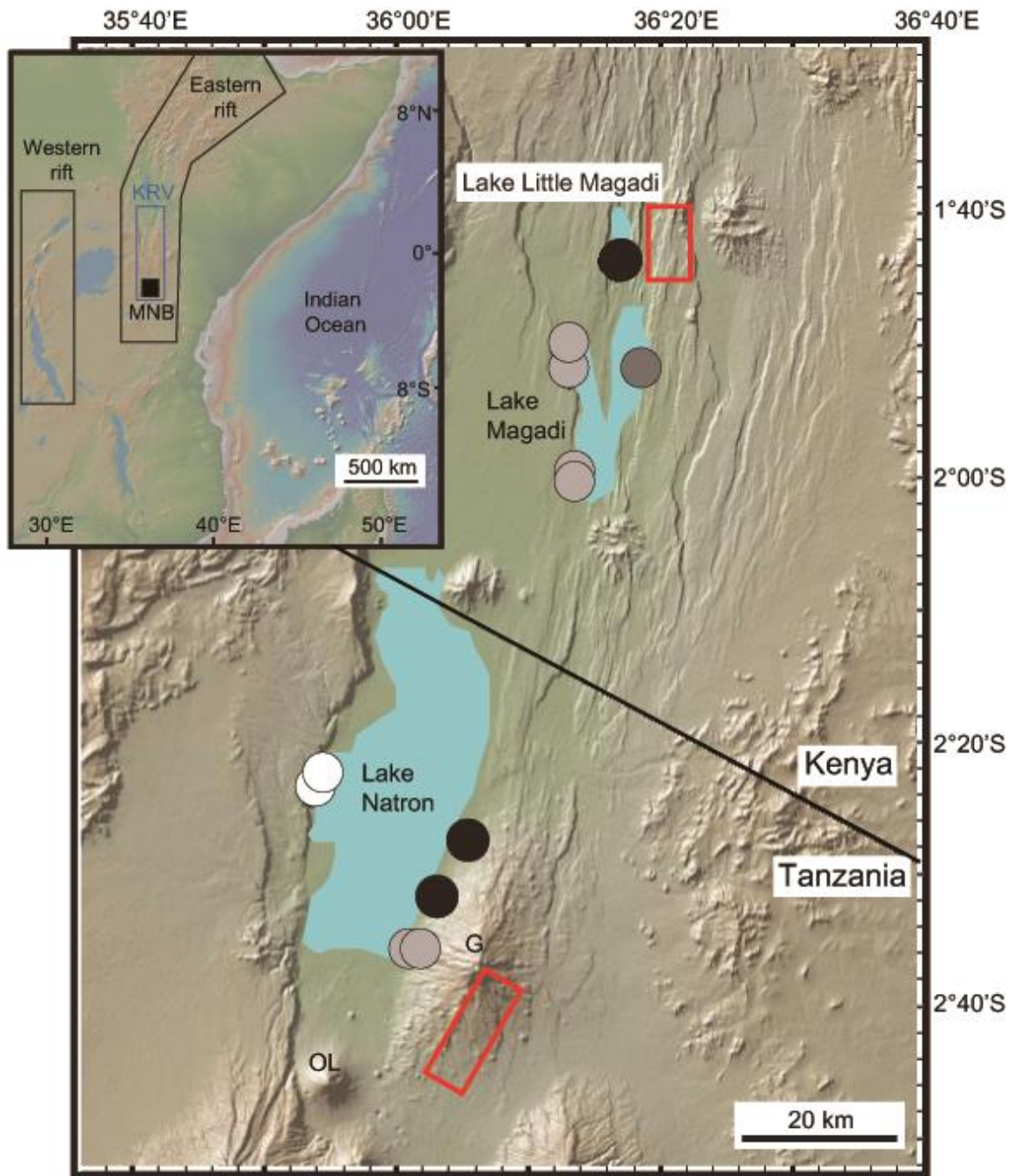
The Kenya Rift Valley (KRV) extends from the Turkana region to Northern Tanzania (Fig. 1), and exhibits a series of lakes within the subsiding basins (Turkana, Baringo, Bogoria Elementeita, Nakuru, Naivasha, Magadi and Natron) (Darling et al., 1995). In addition, a number of volcanic centers (Barrier, Namarunu, Emuruangogorak, Silali, Paka, Korosi, Menengai, Eburru, Longonot, Olkaria domes, Suswa, and Oldoinyo Lengai) and related geothermal areas are utilized for geothermal exploration (Hochstein et al., 2000). Darling et al. (1995) noted that the KRV releases mantle-derived gases via fumaroles, boreholes and seeps associated with volcanic centers. Recently magmatic volatile release has been quantified at Longonot volcano (Robertson et al., 2016).

The Magadi and Natron basin (MNB) is located in the southern section of the eastern rift (KRV), at the border of southern Kenya and Tanzania and are partly filled by lakes Magadi, Little Magadi, and Natron. The MNB hereafter will be distinguished from northern areas of the KRV as the Magadi and Natron basins are in an earlier stage of continental rifting (Muirhead et al., 2016), with rifting initiating at ca. 7 and 3 Ma, respectively (Crossley,

1979; Baker et al., 1987; Foster et al., 1997). The rift developed in Archean and Late Proterozoic crust, and the ~N-S suture between the two crustal provinces lies ~50 km west of the Eastern rift. Crystalline basement is overlain by widespread Miocene trachytes and recent sediments (e.g., Baker et al., 1987; Ebinger et al., 1997). Several volcanoes lie within the MNB: Lenderut, Shompole, Gelai, Oldoinyo Lengai, and Karisimbi volcanoes, with historic eruptions at Oldoinyo Lengai volcano, and a dike intrusion along the southern flank of Gelai volcano in a broad monogenetic cone complex (Muirhead et al., 2015). Several other Quaternary volcanoes lie on the uplifted western footwall (Muirhead et al., 2016; Weinstein et al., submitted). In addition, the area is tectonically active, with seismic swarm events in 1997-1998 and 2007 at northern Magadi and eastern Natron (near Gelai volcano) areas (Ibs-von Seht et al., 2001; Calais et al., 2008) (Fig. 1). Lakes Magadi, Little Magadi, and Natron are fed by hot springs ($T < 86^{\circ}\text{C}$) which discharge saline alkaline fluids (Eugster, 1970; Hochstein et al., 2000). Lake Magadi has a thick trona ($\text{Na}_2\text{CO}_3 \cdot \text{NaHCO}_3 \cdot 2\text{H}_2\text{O}$) deposit that resulted from evaporation of saline alkaline waters (Jones et al., 1977). The hydrology of lake Magadi is subdivided into dilute streamflow, dilute groundwater, saline groundwater, saturated brines, and remain brines on the basis of water chemistry (Jones et al., 1977). It has been reported that the saline spring waters of both the Magadi and Natron regions are Na- HCO_3 waters (Jones et al., 1977; Hochstein et al., 2000).

Several geothermal exploration studies have been previously conducted in the MNB (Crane, 1981; Crane and O'Connell, 1983). Additionally, Barry et al. (2013) reported on two spring samples at the western side of Lake Natron, giving radiogenic ^4He -rich isotope values ($^3\text{He}/^4\text{He} = 0.61 - 0.67 \text{ Ra}$), as well as flux of total CO_2 and ^3He , of $5.0 \times 10^8 \text{ mol/yr}$

and 0.46 mol/yr, respectively. Muirhead et al. (2016) also reported data from 5 thermal springs in the MNB which show a two-component mixing relationship between the mantle and air. Lee et al. (2016) made the first measurements of diffuse CO₂ emission in the MNB and analyzed carbon isotopes, proposing that 4.05 Mt/yr of the mantle-derived CO₂ degasses along faults that penetrate to lower crustal levels (Weinstein et al., submitted). A recent study of Muirhead et al. (2016) also suggest that these areas of magmatic volatile release in the MNB coincide with zones of high fault strain. However, sources as well as the flux of volatiles from hydrothermal systems in the MNB is poorly known, despite having important implications for the role of volatile release in early-stage rifting processes.



KRV: Kenya rift valley
MNB: Magadi and Natron basin
OL: Oldoinyo Lengai
G: Gelai

Seismic swarm

- $R/Ra > 3$
- $2 < R/Ra < 3$
- $1 < R/Ra < 2$
- $R/Ra < 1$

Fig. 1. Map of the Magadi and Natron basin (MNB), made by GeoMapApp (Ryan et al., 2009). The inset displays the western and eastern rifts as well as the Kenya rift valley (KRV) and the study area (MNB). Locations of the 15 sampled thermal springs show different color based on $^3\text{He}/^4\text{He}$ isotope ratios. Also, seismic swarms reported in (Ibs-von Seht et al., 2001; Calais et al., 2008) are highlighted.

Table 1. Field data of the MNB thermal springs and the KRV samples.

area	ID	type	method	Date (month-year)	latitude (S°)	longitude (E°)	T (°C)	pH
Magadi W	KN14-S01	Spring	empty	Jun-14	1.85744	36.219	48.4	8.9
Magadi W	KN14-S02	Spring	empty	Jun-14	1.86319	36.21983	47.7	9.3
Magadi W	KN14-S03	Spring	empty	Jun-14	1.83581	36.21839	46.4	9.1
Magadi S	KN14-S05	Spring	empty	Jun-14	2.00228	36.23148	44.7	9.8
Magadi S	KN14-S06	Spring	empty	Jun-14	1.99825	36.23131	44.6	9.9
Magadi S	KN14-S07	Spring	empty	Jun-14	2.00284	36.22848	39	9.8
Little Magadi	KN14-S08	Spring	empty	Jun-14	1.72756	36.28086	83.5	9.5
Little Magadi	KN14-S09	Spring	empty	Jun-14	1.72547	36.27828	82.3	9.3
Magadi E	KN14-S11	Spring	empty	Jun-14	1.85989	36.30636	35	10
Natron W	TZ14-S01	Spring	empty	Jul-14	2.37314	35.90581	50.7	10.3
Natron W	TZ14-S02	Spring	empty	Jul-14	2.39228	35.89828	51.2	10.3
Natron E	TZ14-S03	Spring	empty	Jul-14	2.45581	36.08842	43.1	9.5
Natron E	TZ14-S04	Spring	empty	Jul-14	2.45411	36.08567		
Natron E	TZ14-S05	Spring	empty	Jul-14	2.52733	36.04928	38.1	9.3
Natron E	TZ14-S06	Spring	empty	Jul-14	2.59283	36.01597	36.8	9.2
Silali	KN13-F01	Fumarole	NaOH	Jun-13	1.13947 (N°)	36.23688	95.5	
Paka	KN13-F03	Fumarole	NaOH	Jun-13	0.91958 (N°)	36.18822	95.4	
Eburru	KN13-F05	Fumarole	NaOH	Jun-13	0.64005	36.24897	92.5	
Menengai	KN13-F08	Fumarole	NaOH	Jun-13	0.2061	36.0667	120.2	
Longonot	KN13-F13	Fumarole	empty	Jun-13	0.90757	36.455	83.1	
Suswa	KN13-F14	Fumarole	NaOH	Jun-13	1.11108	36.34873	93.7	
Lorusio	KN13-S01	Bubbling spring	NaOH	Jun-13	1.25480 (N°)	36.11558	79.6	8.5
Lorusio	KN13-S02			Duplicate sample				
Bogoria	KN13-S03	Bubbling spring	NaOH	Jun-13	1.16848 (N°)	36.10502	79.5	8.5
Bogoria	KN13-S04			Duplicate sample				

4. SAMPLES AND ANALYTICAL METHODS

The thermal spring samples in the MNB ($T = 36.8 - 83.5^{\circ}\text{C}$) and the KRV ($T = 40.0 - 79.6^{\circ}\text{C}$) were collected in pre-evacuated Giggenbach bottles. Gas samples from fumaroles and bubbling thermal springs from Silali to Suswa in the KRV were collected in pre-evacuated Giggenbach bottles filled with 4N-NaOH solution. Locations and types of samples are summarized in Table 1. Dissolved gas compositions in the thermal waters and solutions were determined in the Volatiles Laboratory at the University of New Mexico (UNM) generally following the procedures of Giggenbach and Goguel (1989). Concentrations of CO_2 , CH_4 , H_2 , $\text{Ar}+\text{O}_2$, N_2 , and CO were measured on a Gow-Mac series G-M 816 Gas Chromatograph (GC) using a helium carrier gas, with experimental errors of $< 2\%$. Gas species were separated on the GC using a Hayes Sep pre-column and 5\AA molecular sieve columns. A discharge ionization detector was used for CO_2 , CH_4 , H_2 , $\text{Ar}+\text{O}_2$, N_2 and CO , respectively. He, Ar, O_2 , and N_2 were also measured in dynamic mode on a Pfeiffer Quadrupole Mass Spectrometer (QMS) with a mass range from 0 to 120 amu and a secondary electron multiplier detector. Analytical errors on the QMS are $< 1\%$. Concentrations of all gas components were acquired after merging the data from GC and QMS. Concentrations of CO_2 and total sulfur (SO_2 and H_2S) in the NaOH solution was determined by CO_2 titration and BaSO_4 precipitation/alkaline iodine titration methods, respectively (Giggenbach and Goguel, 1989). Argon isotope ratios ($^{40}\text{Ar}/^{36}\text{Ar}$) were determined in static mode on QMS. Hydrogen (δD) and oxygen ($\delta^{18}\text{O}$) isotopes in water samples were simultaneously analyzed by a Los Gatos Research (LGR) liquid water isotopic analyzer in the Center for Stable Isotopes (CSI), at UNM. Total dissolved inorganic carbon (TDIC) contents including HCO_3^- and CO_3^{2-} were obtained by titration

using 0.1N or 0.01N-H₂SO₄ solution. Because we assumed that extensive dissolution of CO₂ occurs in the alkaline spring waters, the total CO₂ contents in Table 2 were calculated by taking TDIC and gaseous CO₂ contents. Nitrogen isotope and carbon isotope compositions were analyzed on an Isotope Ratio Mass Spectrometer (Thermo Delta V Plus) with a gas bench in CSI at UNM, following methods described in Fischer et al. (2002), Zimmer et al. (2004), Elkins et al. (2006), Newell et al. (2008), and de Moor et al. (2013). Experimental errors for both $\delta^{15}\text{N}$ and $\delta^{13}\text{C}$ are 0.1‰ (1 σ). For helium isotope analyses, copper tubes were used to collect fumarole and thermal spring samples. $^3\text{He}/^4\text{He}$ ratios were analyzed on noble gas mass spectrometers (Helix-SFT and VG-5400) at the Atmosphere and Ocean Research institute of the University of Tokyo (AORI). He and Ne were purified using hot titanium getters (at 400°C) and charcoal traps (at liquid nitrogen temperature). The $^4\text{He}/^{20}\text{Ne}$ ratios were acquired by an on-line QMS. Neon was removed using a cryogenic trap (at 40°K). Experimental errors for $^3\text{He}/^4\text{He}$ and $^4\text{He}/^{20}\text{Ne}$ ratios are about 1% and 5% (1 σ , SFT-Helix) and about 3.5% and 5% (1 σ , VG5400), respectively (Sano et al., 2008). The correction of $^3\text{He}/^4\text{He}$ ratios for atmospheric helium used measured $^4\text{He}/^{20}\text{Ne}$ ratios (Craig et al., 1975) because ^{20}Ne is assumed as almost atmospheric. Accordingly:

$$\text{Rc/Ra} = (^3\text{He}/^4\text{He})_{\text{measured}} / (1 - ((^4\text{He}/^{20}\text{Ne})_{\text{ASW}} / (^4\text{He}/^{20}\text{Ne})_{\text{measured}})) \quad (1)$$

where Rc/Ra denotes the air-corrected $^3\text{He}/^4\text{He}$ ratio, and $(^4\text{He}/^{20}\text{Ne})_{\text{ASW}}$ is the $^4\text{He}/^{20}\text{Ne}$ of ASW (air-saturated water) ratio.

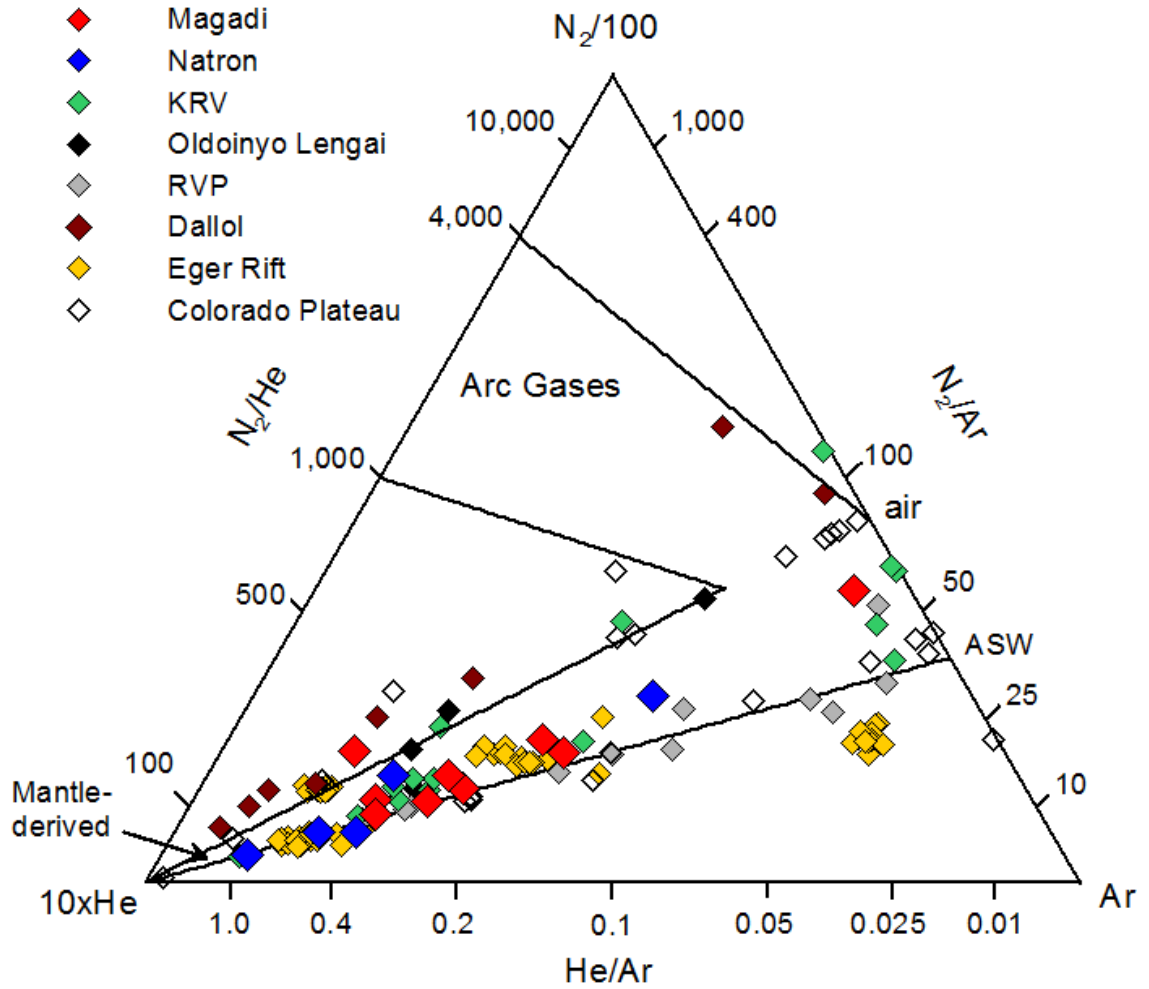


Fig. 2. N₂-He-Ar ternary plot. Solid lines represent mixing lines between MORB and air/ASW and Arc gases and air/ASW. Compositions of MORB, air, and ASW are from Marty and Zimmermann (1999), Fischer et al. (2002), and Fischer et al. (2009). KRV and RVP represent Kenya Rift Valley and Rungwe Volcanic Province, respectively. The Oldoinyo Lengai, Rungwe volcanic province, and Dallol data points are previously reported in the EAR (Fischer et al., 2009; de Moor et al., 2013; Darrah et al., 2013). Eger rift and Colorado Plateau values are from Bräuer et al. (2004) and Crossey et al. (2009), respectively.

5. RESULTS

Chemistry of dissolved gases is summarized in Table 2. CO₂ is the major volatile component (966-996 mmol/mol) of the MNB thermal springs like the KRV samples (up to 981 mmol/mol), followed by N₂. Most of the samples show minor O₂ concentration (< ~16 mmol/mol) except for KN13-F13, KN13-F14, and KN13-F15 which reflect significant air contribution (> ~114 mmol/mol). The KRV fumarole samples contain H₂S (up to 108 mmol/mol) without SO₂ and minor amount of HF and HCl, but the bubbling springs have lower concentrations of H₂S (< 1 mmol/mol). CH₄ and H₂ are minor in the MNB in comparison with the KRV samples, which have CH₄ up to 47mmol/mol and H₂ up to 28 mmol/mol. Ar is also minor (< 1 mmol/mol), but the samples with severe air contribution display higher Ar contents (e.g., KN13-F13, KN13-F14, and KN13-F15), indicating such Ar is mostly derived from air. Helium and CO are minor too, but most of He/Ar ratios are greater than 0.01 distinguished from air (Table 2).

$\delta^{18}\text{O}$ and δD values of the MNB and KRV waters average -4.4 to -0.2‰ and -28.9 to -3.9‰, respectively (Table 3). KRV springs have $\delta^{18}\text{O}$ and δD values of (-3.4 to -0.2‰) and δD (-19.0 to -4.2‰), respectively (Table 3). $\delta^{15}\text{N-N}_2$ values of all samples (MNB and KRV) show a narrow range (-1.6 to +2.6‰) except for KN14-S11 (+5.9‰) that likely reflects a locally biogenic N₂-rich sampling site (Table 4). $\delta^{13}\text{C}_{\text{T DIC}}$ values of the MNB thermal springs range from -0.4 to +3.7‰ (Table 4). $^{40}\text{Ar}/^{36}\text{Ar}$ ratios of the MNB springs range from 303.5 to 451.9 (Table 4) which are two orders of magnitude lower than the MORB value ($^{40}\text{Ar}/^{36}\text{Ar} = 44,000$, Moreira et al., 1998). The highest value comes from samples from Oldoinyo Lengai fumaroles (947, Fischer et al., 2009), indicating that they

are significantly affected by air ($^{40}\text{Ar}/^{36}\text{Ar} = 295.5$). The range of $^{40}\text{Ar}/^{36}\text{Ar}$ ratios in the KRV are 273.2 to 322.0, and show less ^{40}Ar than the MNB samples. They are consistent with measurements of Darling et al. (1995) who proposed Ar is mainly atmospheric.

$\delta^{13}\text{C}-\text{CO}_2$ values of the MNB thermal springs are calculated based on two equilibrium reactions (HCO_3-CO_2 and CO_3-HCO_3) in alkaline aquifer systems, following the approaches of Allard et al. (1997) and Gilfillan et al. (2009):

$$\delta^{13}\text{C}-\text{CO}_2 = \delta^{13}\text{C}_{\text{TDIC}} - \varepsilon_{\text{HCO}_3-\text{CO}_2} + f_{\text{HCO}_3/\text{TDIC}} \times \varepsilon_{\text{CO}_3-\text{HCO}_3} \quad (2)$$

where $\varepsilon_{\text{HCO}_3-\text{CO}_2}$ and $\varepsilon_{\text{CO}_3-\text{HCO}_3}$ are the fractionation factors (as ‰) during gas-water transfer and dissolution of CO_2 (Zhang et al. 1995), respectively, and $f_{\text{HCO}_3/\text{TDIC}}$ is the molar fraction of HCO_3 relative to TDIC. $\delta^{13}\text{C}-\text{CO}_2$ values of both the MNB and KRV samples (-7.1 to -3.1‰) are generally within the range of previously reported values (-6.9 to -1.7‰, Darling et al., 1995), except for two samples at Little Magadi (-0.9 and +1.6‰) (Table 4). $\text{CO}_2/{}^3\text{He}$ ratios of the MNB and KRV samples range from 0.7×10^8 to 1.84×10^{11} (Table 4). The MNB thermal springs have higher ${}^3\text{He}/{}^4\text{He}$ ratios (0.64 and 4.00 Ra) than the crustal end-member (0.02 Ra; Ozima and Podosek, 1983) (Table 4). ${}^3\text{He}/{}^4\text{He}$ ratios of the KRV samples range from 2.13 to 7.49 Ra, which are similar as Darling et al. (1995) have reported. In Table 4, the corrected ${}^3\text{He}/{}^4\text{He}$ ratios (R_c/R_a) are similar to R/R_a values because ${}^4\text{He}/{}^{20}\text{Ne}$ ratios of the MNB thermal springs (mean = 218.7) and the KRV samples (mean = 127.3) are much greater than those of ASW (0.273) or air (0.318), indicating minor air contribution to the samples. Some samples, such as KN14-S1, TZ14-S6, KN13-F13, and KN13-F14, show somewhat higher air contributions based on ${}^4\text{He}/{}^{20}\text{Ne}$ ratios. (Table 4). As shown in Fig. 1 and Table 4, higher ${}^3\text{He}/{}^4\text{He}$ ratios are observed at the Little Magadi

(up to 3.51 Ra) and eastern Natron (up to 4.00 Ra) areas. The lowest $^3\text{He}/^4\text{He}$ ratios are 0.64 and 0.70 Ra (this study) at western Natron where lower $^3\text{He}/^4\text{He}$ ratios (0.61 - 0.67 Ra) have also been reported by Barry et al. (2013). Amounts of ^4He in all waters range from 1.59×10^{-4} to 3.55×10^{-6} ccSTP/g (Table 4).

Table 2. Results of gas chemistry and elemental ratios.

Sample ID	CO ₂	N ₂	Ar	He	O ₂	H ₂	CH ₄	CO
	mmol/mol							
KN14-S01 ^a	989.644	10.012	0.241	0.052	0.002	0.003	0.045	0.0008
KN14-S02	994.567	5.262	0.103	0.024	0.004	0.002	0.038	0.0001
KN14-S03	993.504	6.274	0.119	0.017	0.069	0.0003	0.016	-
KN14-S05	991.799	7.921	0.201	0.052	0.001	0.0014	0.025	-
KN14-S06 ^a	994.383	5.424	0.103	0.037	0.026	0.0011	0.026	-
KN14-S07	992.019	7.778	0.178	0.023	0.002	-	-	-
KN14-S08	996.325	2.279	0.055	0.019	0.004	0.002	1.316	-
KN14-S09	995.485	2.758	0.024	0.012	0.003	0.001	1.718	-
KN14-S11 ^a	991.965	7.324	0.117	0.001	0.591	-	-	-
TZ14-S01 ^a	989.706	9.817	0.248	0.126	0.0003	0.003	0.101	-
TZ14-S02	985.252	14.007	0.434	0.166	0.001	0.003	0.138	-
TZ14-S03	994.251	5.449	0.143	0.137	0.001	0.0002	0.019	0.0001
TZ14-S05	978.477	19.751	0.3	0.1	1.37	-	0.002	-
TZ14-S06 ^a	966.371	28.9	0.535	0.043	4.152	-	-	-
Sample ID	CO ₂	N ₂	Ar	He	O ₂	H ₂	CH ₄	CO
	mmol/mol							
KN13-F01	928.105	7.579	0.164	0.042	0.001	10.354	7.705	-
KN13-F02	915.678	16.224	0.307	0.079	0.274	14.742	11.682	-
KN13-F03	883.634	6.095	0.13	0.04	n.d	7.948	16.323	-
KN13-F04	945.043	2.919	0.051	0.015	-	4.841	9.059	-
KN13-F05	845.902	3.086	0.068	0.008	-	6.207	35.855	-
KN13-F07	811.562	11.72	0.267	0.105	-	21.483	47.066	-
KN13-F08	875.919	5.983	0.105	0.034	0.008	28.106	26.784	0.0354
KN13-F09	942.535	5.061	0.135	0.141	0.008	15.623	19.502	0.0387
KN13-F13	177.638	699.67	5.984	0.01	114.116	-	2.582	-
KN13-F14	448.974	353.698	5.615	0.004	119.225	0.05	2.223	-
KN13-F15	431.298	357.673	5.51	0.004	137.802	0.069	2.66	-
KN13-S01	949.604	32.435	0.787	0.007	15.777	0.0016	1.081	0.0029
KN13-S02	980.723	13.036	0.254	0.002	5.306	0.0007	0.381	0.0009
KN13-S03	981.64	12.986	0.14	0.013	0.311	0.0001	4.593	-
KN13-S04	955.112	33.801	0.388	0.103	0.998	0.0005	9.328	-

Table 2. (continued).

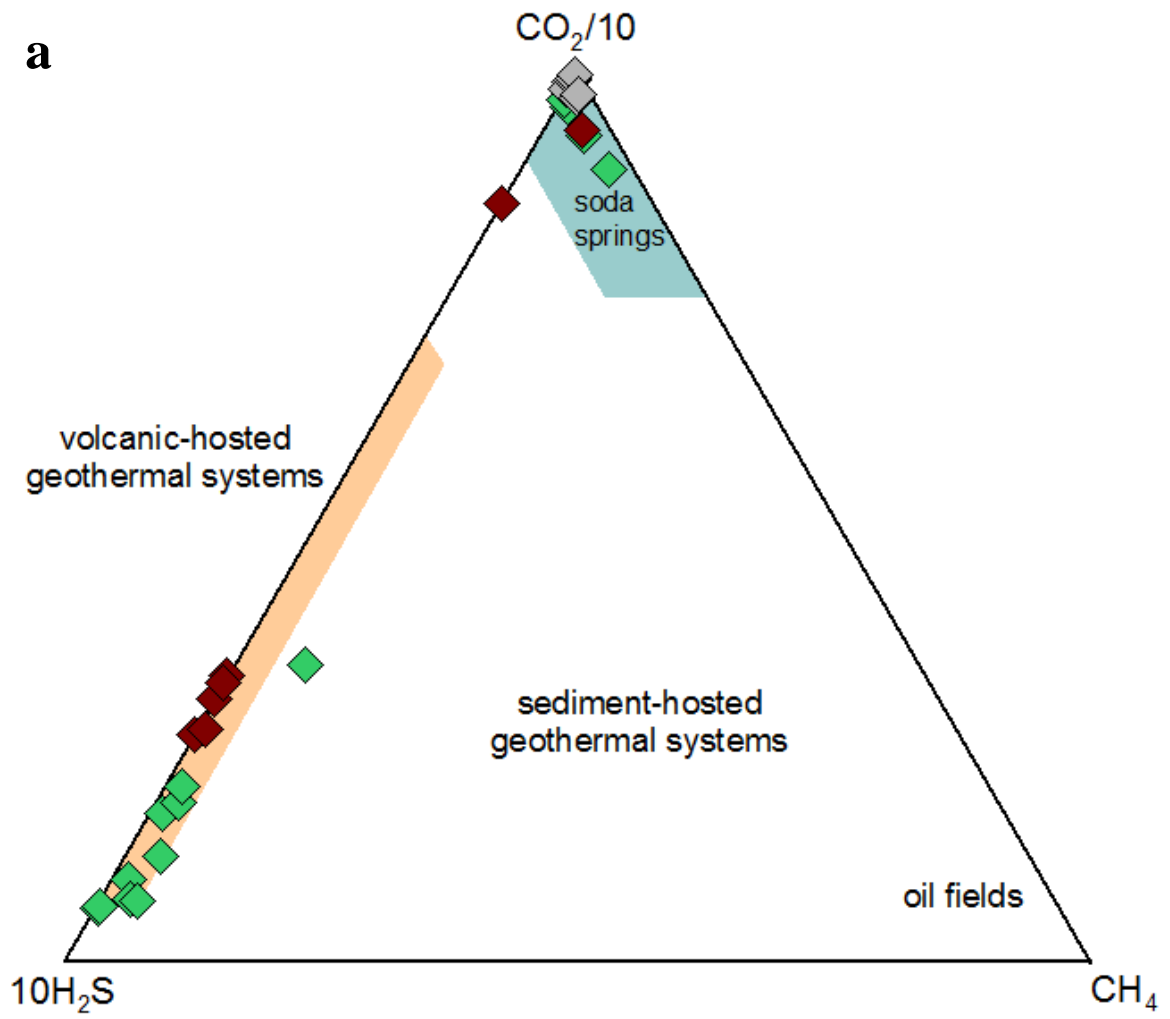
Sample ID				N ₂ /He	N ₂ /Ar	He/Ar
KN14-S01 ^a				194	41.5	0.21
KN14-S02				217	51.1	0.24
KN14-S03				363	52.6	0.14
KN14-S05				154	39.4	0.26
KN14-S06 ^a				146	52.6	0.36
KN14-S07				342	43.7	0.13
KN14-S08				119	41.7	0.35
KN14-S09				235	115	0.49
KN14-S11 ^a				6,039	62.5	0.01
TZ14-S01 ^a				78	39.6	0.51
TZ14-S02				84	32.3	0.38
TZ14-S03				40	38	0.96
TZ14-S05				197	65.8	0.33
TZ14-S06 ^a				679	54	0.08
Sample ID	H ₂ S	HF	HCl	N ₂ /He	N ₂ /Ar	He/Ar
	mmol/mol					
KN13-F01	46.022	-	0.029	180	46.2	0.26
KN13-F02	40.991	0.0104	0.014	205	52.8	0.26
KN13-F03	85.806	0.0071	0.018	152	46.9	0.31
KN13-F04	38.064	-	0.01	195	57.2	0.29
KN13-F05	108.783	0.0219	0.07	386	45.4	0.12
KN13-F07	107.635	0.0601	0.102	112	43.9	0.39
KN13-F08	63.009	0.007	0.01	176	57	0.32
KN13-F09	16.934	0.0058	0.016	36	37.5	1.04
KN13-F13	-	-	-	69,967	116.9	0.002
KN13-F14	69.855	-	0.357	88,425	63	0.001
KN13-F15	64.705	-	0.279	89,418	64.9	0.001
KN13-S01	0.29	0.0043	0.011	4,634	41.2	0.01
KN13-S02	0.286	0.0041	0.006	6,518	51.3	0.01
KN13-S03	0.304	0.0039	0.009	999	92.8	0.09
KN13-S04	0.254	0.0038	0.011	328	87.1	0.27

Table 3. Results of O-H isotopes of thermal spring waters.

Sample ID	$\delta^{18}\text{O}$	δD
	‰ vs VSMOW	
KN14-S01	-3.0	-18.6
KN14-S02	-2.8	-17.1
KN14-S03	-3.2	-19.3
KN14-S05	-2.6	-18.2
KN14-S06	-2.8	-18.4
KN14-S07	-3.0	-19.5
KN14-S08	-0.3	-3.9
KN14-S09	-0.2	-4.6
KN14-S11	-0.3	-8.2
TZ14-S01	-4.0	-27.1
TZ14-S02	-4.4	-28.9
TZ14-S03	-3.7	-21.5
TZ14-S05	-4.2	-23.8
TZ14-S06	-4.3	-25.2
Lorusio^a	-1.9	-14.1
Kapedo^b	-0.2	-4.2
Bogoria^a	-3.4	-19.0

^aInformation of the Lorusio and Bogoria springs are in Table 1.

^bLocation of the Kapedo spring (T = 51.7°C and pH = 9.0) is N1.16848° and E36.10501°.



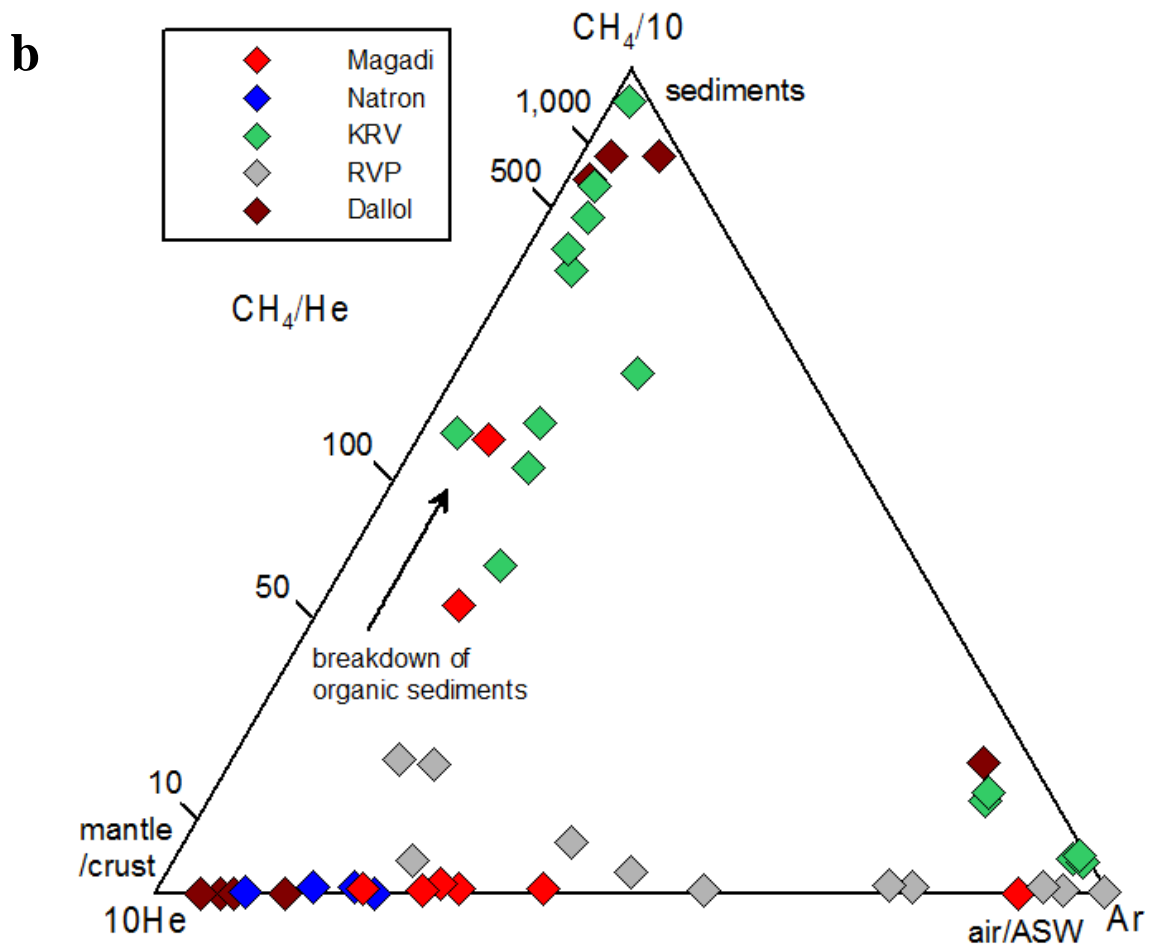


Fig 3. a. CO₂-H₂S-CH₄ ternary plot with fields of volcanic/sediment-hosted geothermal systems, soda springs, and oil fields (after Goff and Janik, 2000) of the EAR gas samples (KRV, RVP, and Dallol). **b.** CH₄-He-Ar ternary plot (after Goff and Janik, 2002) of the EAR gas samples (MNB, KRV, RVP, and Dallol). The higher CH₄/He ratios reflect the contribution by breakdown of organic sediments (Goff and Janik, 2002). The RVP and Dallol gases are reported in de Moor et al. (2013) and Darrah et al. (2013), respectively.

6. DISCUSSION

6.1. Gas geochemistry

The N₂-He-Ar relative abundances of the MNB samples (Fig. 2) show a two-component mixing relationship between deep (mantle-derived) and shallow (air/ASW) sources (Fig. 2). This is consistent with other areas in the EAR, for example, the KRV (Darling et al., 1995; Muirhead et al., 2016; this study), Oldoinyo Lengai fumaroles (Fischer et al., 2009), the Rungwe volcanic province (RVP, de Moor et al., 2013), and the Dallol region (Darrah et al., 2013) as well as other continental areas, such as the Eger rift (Bräuer et al., 2004) and the Colorado Plateau (Crossey et al., 2009). Some of the MNB samples have lower N₂/He ratios (40 - 84, Table 2) than the MORB value (150; Marty and Zimmermann, 1999). High He concentrations (up to 10.2 vol%) were observed in central Tanzania (Macheyeki et al., 2008), and this is ascribed to release of radiogenic He from the Archean Tanzanian Craton and Proterozoic Mozambique belt composed of plutonic and metamorphic rocks by heating and fracturing (Danabalan et al., 2016). Similarly, lower N₂/He ratios than MORB are observed in the Eger rift samples, ranging from 20 to 6,500 (Weinlich et al., 1999; Bräuer et al., 2004). The MNB and Eger rift areas are both continental rifts, associated with old plutonic and metamorphic rocks (Tanzanian craton and Variscan massif, respectively) which likely contain abundant U and Th rich rocks to produce and release radiogenic ⁴He. Detailed crustal He degassing is discussed in section 6.5.

CO₂, CH₄, H₂S, He, and Ar data indicate that the gases are affected by both magmatic and thermogenic processes, and suggest that CH₄ is mainly produced by thermogenesis. CH₄ and H₂S are observed in the KRV samples (Table 2) as observed in the RVP (de Moor et al., 2013) and Dallol (Darrah et al., 2013) gases. The CO₂-H₂S-CH₄ relationships (Fig. 3a)

show that the KRV fumaroles are in the field of volcanic-hosted geothermal systems like the majority of Dallol gases, with $\text{CO}_2/\text{H}_2\text{S}$ ratios ranging from 6.4 to 55.7. The KRV bubbling springs are all associated with soda springs, coinciding with the RVP and several Dallol gases, which are related to travertine depositing springs (Crossey et al., 2009; de Moor et al., 2013). In comparison with other MNB springs, CH_4 is relatively more abundant in the Little Magadi springs (Table 2), with CH_4/He ratios higher than 50 as well as the KRV samples with the CH_4/He ratios ranging from 91 to 4,482 (Fig. 3b). These CH_4/He ratios likely reflect CH_4 addition because they are significantly higher than the ratios of Oldoinyo Lengai fumaroles (0.1 - 8.5, Fischer and Lee unpublished), which could represent more mantle-like compositions. Darling et al. (1995) proposed that CH_4 in the KRV is derived from thermogenic decomposition of organic matter. In the Dallol bubbling springs, several samples have abundant CH_4 that is associated with thermogenic production (Darrah et al., 2013). In Fig. 3b, two Little Magadi springs and the majority of KRV and Dallol samples reflect the contribution by organic sediments to increase CH_4/He ratios. Other MNB springs, RVP, and a few of KRV and Dallol samples show two component mixing relationship between mantle/crust and air/ASW.

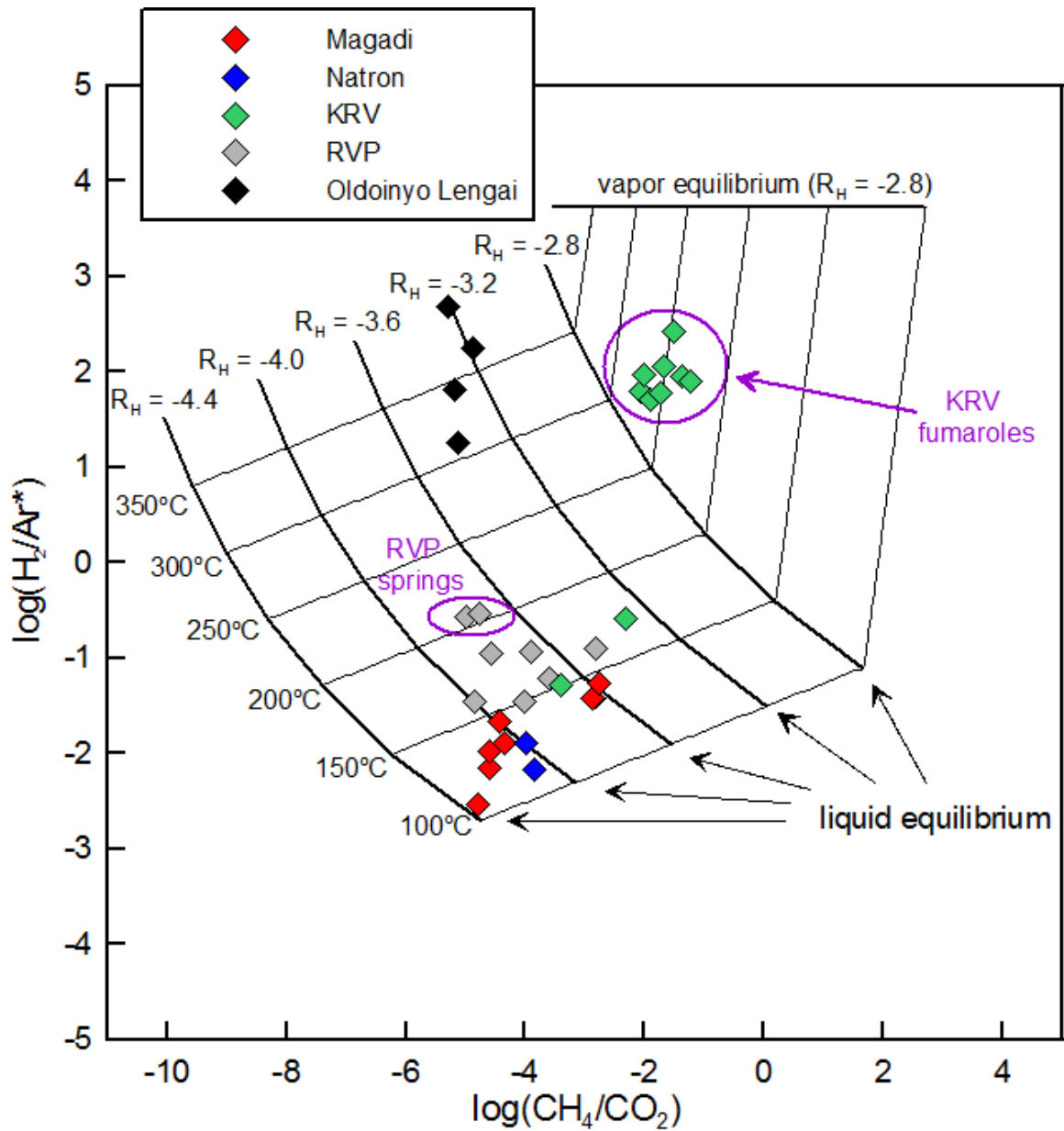


Fig. 4. $\log(\text{H}_2/\text{Ar}^*)$ versus $\log(\text{CH}_4/\text{CO}_2)$ binary plot. Vapor and liquid equilibrium curves are displayed with isotherms ($T = 100 - 350^\circ\text{C}$). R_H is $\log(\text{H}_2/\text{H}_2\text{O})$ (Giggenbach, 1987). The RVP data of gas vents and springs is reported in de Moor et al. (2013). The Oldoinyo Lengai values are from unpublished data which were sampled in July 2005.

6.2. Gas geothermometry

Gas geothermometers are well constrained by the H₂O-CO₂-H₂-CO-CH₄ abundances in hydrothermal fluids, which are utilized in gas geothermometry (Chiodini and Marini, 1998). Using molar fractions of H₂, Ar, CO₂, and CH₄ (Table 2), the CO₂-H₂-CH₄ equilibria of the MNB and KRV samples as well as the RVP samples (reported in de Moor et al., 2013) are defined using the approaches of Tassi et al. (2010) and Benavente et al. (2016) as follows:

$$\log(\text{H}_2/\text{Ar}^*)_{\text{vapor}} = R_H + 6.52 \quad (3)$$

$$\log(\text{H}_2/\text{Ar}^*)_{\text{liquid}} = R_H - \log(B_{\text{H}_2}) + 6.52 \quad (4)$$

$$\text{Ar}^* = \text{Ar} - \text{O}_2/22 \quad (5)$$

$$\log(\text{CH}_4/\text{CO}_2)_{\text{vapor}} = 4R_H + 5.181/ T(\text{K}) \quad (6)$$

$$\log(\text{CH}_4/\text{CO}_2)_{\text{liquid}} = 4R_H + 5.181/ T(\text{K}) + \log(B_{\text{CO}_2}) - \log(B_{\text{CH}_4}) \quad (7)$$

where R_H is $\log(\text{H}_2/\text{H}_2\text{O})$, and B_{H_2} , B_{CO_2} , and B_{CH_4} are distribution coefficients depending on temperature between vapor and liquid phases (Giggenbach, 1980; 1987). Assuming hydrothermal fluids are O₂-free, Ar* is a value taking into account air contamination at the surface (Tassi et al., 2010; Benavente et al., 2016). The R_H of the Fe(II)-Fe(III) redox buffer is -2.8, which represents typical hydrothermal fluids (Giggenbach, 1987).

Using this approach, gas geothermometry of the MNB thermal springs indicates low temperatures, suggesting that magmatic volatiles were cooled down and oxidized in the shallow subsurface. The KRV fumarolic gases are clearly distinguished from other samples, implying that the fumaroles are a mixture of vapor and liquid phases in the hydrothermal systems (Fig. 4). R_H values of the KRV fumaroles (-2.4 to -2.8) show that the equilibrium conditions are more reduced than the Fe(II)-Fe(III) buffer, with equilibrium

temperatures ranging from ~280 to ~340°C. This could indicate magmatic volatiles discharging at the fumaroles are reduced, coinciding with H₂S dominated sulfur species (Table 2). The Oldoinyo Lengai fumaroles show hotter (T = ~300 to ~400°C) and more oxidized (R_H = -3.2 to -3.4) equilibrium conditions than the buffer and KRV fumaroles (Fig. 4). SO₂ flux at Oldoinyo Lengai measured by Fischer et al. (2006) supports the release of oxidized magmatic fluids. The MNB spring gases are oxidized (R_H = -3.6 to -4.4), similar to the KRV springs (R_H = -3.2 to -3.8) and RVP samples that include samples from both gas vents and springs (R_H = -3.6 to -4.0). Hence, equilibrated temperatures of the MNB springs range from ~100 to ~150°C. However, the temperature range is colder than the ranges of RVP gas vents and springs (up to ~230°C) and KRV springs (up to ~180°C) (Fig. 4) as well as the calculated maximum temperature (255°C) at the RVP using the CO₂-CH₄ geothermometer (de Moor et al., 2013). Thus, the dissolved gases are likely magmatic, but masked by shallow re-equilibration processes associated with crustal material and groundwater.

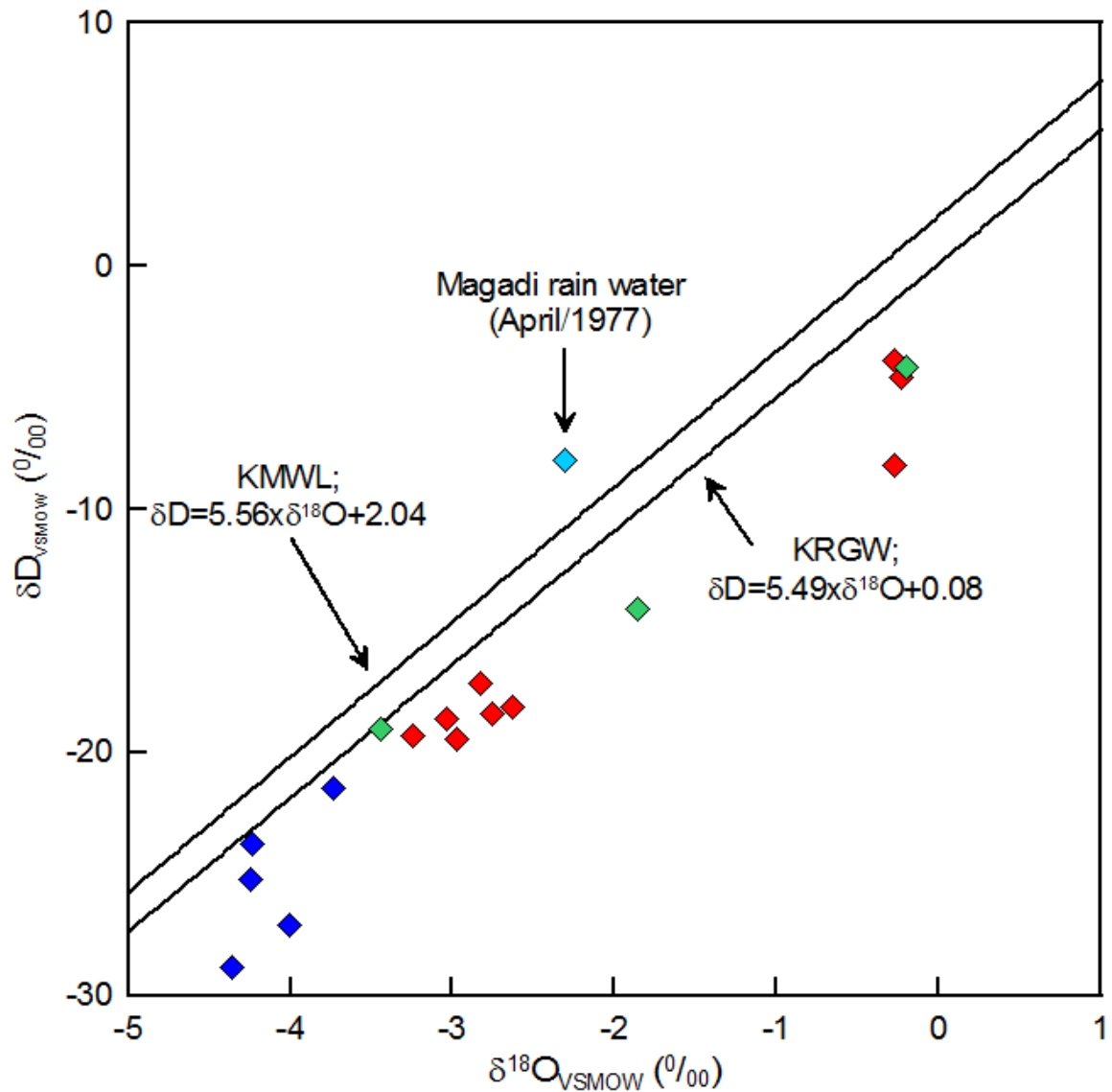


Fig. 5. Plot of $\delta^{18}\text{O}$ and δD values of the MNB and KRV spring waters (symbols as in Fig. 4). Two solid lines represent Kenya Meteoric Water Line (KMWL) and Kenya Regional Groundwater (KRGW) defined by Allen et al. (1989). The light blue diamond shows isotope values of rainfall in the Magadi area (April in 1977, Levin et al., 2009).

Table 4. Results of isotopes (N₂, Ar, CO₂, and He).

sample	$\delta^{15}\text{N}-\text{N}_2^a$	\pm	$\text{N}_2/\beta\text{He}$	$^{40}\text{Ar}/^{36}\text{Ar}$	\pm
ID	% vs air		(x 10 ⁸)		
KN14-S01 ^c	-1.1	< 0.1	1.47	308	0.2
KN14-S02	-1.0	< 0.1	0.62	303.5	0.2
KN14-S03	-1.2	< 0.1	0.7	313.2	0.1
KN14-S05	-0.5	0.1	0.36	310.2	0.1
KN14-S06 ^c	-0.6	< 0.1	0.39	321.2	0.1
KN14-S07	0.4	< 0.1	0.91	331.1	0.1
KN14-S08	-1.2	< 0.1	0.16	346.8	0.1
KN14-S09	-0.2	< 0.1	0.69	345.2	0.1
KN14-S11 ^c	5.9	0.1	13.27	320.5	0.2
TZ14-S01 ^c	-0.8	< 0.1	0.53	340.6	0
TZ14-S02	-1.0	< 0.1	1.06	345.8	0.1
TZ14-S03	-1.5	< 0.1	0.04	451.9	0.1
TZ14-S04					
TZ14-S05	-1.0	< 0.1	0.17	337.1	0.1
TZ14-S06 ^c	-0.7	< 0.1	0.94	327.1	0.1
KN13-F01	-1.6	0.5	0.17	308.8	1.3
KN13-F02				298.9	1.6
KN13-F03	1.7	0.2		306.6	0.9
KN13-F04				303.9	0.8
KN13-F05	-0.4	0.3	0.64	294.2	2.2
KN13-F07				290.9	2.2
KN13-F08	1.5	0.4	0.27	281.9	2.1
KN13-F09				273.2	2.1
KN13-F13	-1.3	0.5	196.97	293.7	0.7
KN13-F14	1.4	0.5	323.8	298	0.6
KN13-F15	-0.2	0.2		299.3	0.5
KN13-S01	-0.6	0.3		293.9	0.7
KN13-S02	0.5	0.7	14.29	299.3	0.7
KN13-S03	2.6	0.4	2.03	303.1	0.7
KN13-S04				322	0.9

^a $\delta^{15}\text{N}$ (‰) = $[(^{15}\text{N}/^{14}\text{N})_{\text{measured}}/(^{15}\text{N}/^{14}\text{N})_{\text{air}} - 1] \times 1000$.

Table 4. (continued).

sample	$\delta^{13}\text{C-TDIC}^b$	\pm	$\delta^{13}\text{C-CO}_2^b$	\pm	$\text{CO}_2/\beta\text{He}^*$
ID	% vs PDB				(x 10 ⁹)
KN14-S01 ^c	0.8	< 0.1	-3.8	< 0.1	15.8
KN14-S02	1	0.1	-3.7	0.1	11.9
KN14-S03	0.7	< 0.1	-4.1	< 0.1	11.2
KN14-S05	1.5	< 0.1	-3.2	< 0.1	4.6
KN14-S06 ^c	1.7	< 0.1	-3.1	< 0.1	7.2
KN14-S07	0.8	< 0.1	-4.5	< 0.1	11.8
KN14-S08	3.7	< 0.1	1.6	< 0.1	6.9
KN14-S09	1.4	< 0.1	-0.9	< 0.1	25.2
KN14-S11 ^c	2.3	< 0.1	-3.2	< 0.1	184.1
TZ14-S01 ^c	1	< 0.1	-3.3	< 0.1	5.4
TZ14-S02	1	< 0.1	-3.2	< 0.1	7.4
TZ14-S03	0.5	< 0.1	-4.5	< 0.1	0.7
TZ14-S04					
TZ14-S05	-0.4	< 0.1	-5.7	< 0.1	0.8
TZ14-S06 ^c	-0.4	< 0.1	-5.7	< 0.1	4.3
KN13-F01			-4.3	0.1	2.1
KN13-F02			-4.1	0.1	
KN13-F03					
KN13-F04			-3.3	0.1	
KN13-F05			-3.6	0.1	17.6
KN13-F07			-3.7	0.1	
KN13-F08			-5.3	0.1	3.9
KN13-F09			-4.7	0.3	
KN13-F13			-7.1	0.4	5
KN13-F14			-6.2	0.1	41.1
KN13-F15			-4.6	0.1	
KN13-S01					
KN13-S02			-5.5	0.1	107.5
KN13-S03			-3.3	0.2	15.3
KN13-S04			-4.8	0.4	

^b $\delta^{13}\text{C} (\text{‰}) = [((^{13}\text{C}/^{12}\text{C})_{\text{measured}}/(^{13}\text{C}/^{12}\text{C})_{\text{PDB}}) - 1] \times 1000$.

^cData reported in Muirhead et al. (2016).

Table 4. (continued).

sample ID	$^3\text{He}/^4\text{He}^d$				$^4\text{He}/^{20}\text{Ne}$
	R/Ra	\pm	Rc/Ra	\pm^e	
KN14-S01 ^c	1.65	0.02	1.78	0.009	1.9
KN14-S02	1.81	0.02	1.81	0.004	379
KN14-S03	1.88	0.02	1.89	0.003	139
KN14-S05	1.94	0.02	1.94	0.004	499
KN14-S06 ^c	1.90	0.02	1.9	0.003	338
KN14-S07	1.65	0.02	1.65	0.003	115
KN14-S08	3.51	0.04	3.51	0.002	194
KN14-S09	3.43	0.04	3.43	0.003	229
KN14-S11 ^c	2.22	0.02	2.25	0.003	11
TZ14-S01 ^c	0.64	0.01	0.64	0.006	377
TZ14-S02	0.70	0.01	0.70	0.005	28
TZ14-S03	4.00	0.04	4.00	0.003	880
TZ14-S04	3.98	0.04	4.03	0.003	18
TZ14-S05	3.30	0.03	3.31	0.002	72
TZ14-S06 ^c	1.45	0.02	1.96	0.058	0.6
KN13-F01	7.49	0.24	7.53	0.01	50
KN13-F02					
KN13-F03					
KN13-F04					
KN13-F05	4.39	0.11	4.4	0.01	
KN13-F07					
KN13-F08	4.74	0.11	4.75	< 0.001	
KN13-F09					
KN13-F13	2.63	0.08	3.24	0.03	
KN13-F14	2.13	0.09	4.5	0.01	
KN13-F15					
KN13-S01					
KN13-S02	2.87	0.09		< 0.001	
KN13-S03	3.50	0.02		0.18	
KN13-S04					

^dRc/Ra=($^3\text{He}/^4\text{He}$)measured / ($^3\text{He}/^4\text{He}$)air. $^3\text{He}/^4\text{He}$ air= 1.39×10^{-6} .

^eThe total error of the corrected $^3\text{He}/^4\text{He}$ ratio is defined in Sano et al. (2006).

6.3. Stable isotopes

6.3.1. O and H isotopes

$\delta^{18}\text{O}$ and δD values of the MNB spring waters all plot slightly to the right of both the Kenyan Meteoric Water Line (KMWL, $\delta\text{D} = 5.56 \times \delta^{18}\text{O} + 2.04$) and Kenyan Rift Ground Water (KRGW, $\delta\text{D} = 5.49 \times \delta^{18}\text{O} + 0.08$) which already reflected evaporative trends compared to the Global meteoric water line (Allen et al., 1989) (Fig. 4). $\delta^{18}\text{O}$ and δD values are consistent with those reported by Allen et al. (1989), which show a slightly positive O-isotope shift. The isotopic shift could be attributed to mixing between meteoric and magmatic waters, water-rock interactions, or evaporation. It is unlikely that meteoric water is mixed with basaltic waters because the $\delta^{18}\text{O}$ values are still lighter than the proposed basaltic magmatic waters ($\delta^{18}\text{O} = 6$ to 10‰ , Allard, 1983) or even Oldoinyo Lengai rocks ($\delta^{18}\text{O} = 7.4$ to 24.1‰ , Mangler et al., 2014). Also, the reservoir temperatures ($T = \sim 100 - \sim 150^\circ\text{C}$) based on the geothermometers are insufficient to reach at O-isotope exchange according to Truesdell and Hulston (1980) and Capaccioni et al. (2014). Lastly, Allen et al. (1989) noted that the KMWL and KRGW already reflect evaporative trends in this area. Moreover, they suggested that the O-H isotopes of the Magadi hot springs represent unaltered meteoric water (local rivers). Hence, it is unlikely that isotope exchange could occur with host rocks.

6.3.2. N₂ sources

N₂ is one of the major dissolved gases in both the MNB and KRV regions and susceptible to air contamination due to abundance in air (78 %). As nitrogen isotopes are contributed

by air, mantle, and sediment, many studies have used $\delta^{15}\text{N}$ versus $^{40}\text{Ar}/^{36}\text{Ar}$ (Marty and Humbert, 1997), $\text{N}_2/^{36}\text{Ar}$ (Sano et al., 1998; 2001), N_2/He (Fischer et al., 2002; Zimmer et al., 2004; Clor et al., 2005; Elkins et al., 2006; de Moor et al., 2013), and $\text{N}_2/^{3}\text{He}$ (Sano et al., 1998; 2001; Bräuer et al., 2004; 2016) values to constrain N_2 sources. In Fig. 6, the relationships between $\delta^{15}\text{N}$ and $^{40}\text{Ar}/^{36}\text{Ar}$ values show that most of the MNB and KRV samples plot near values of air ($\delta^{15}\text{N} = 0\text{‰}$; $^{40}\text{Ar}/^{36}\text{Ar} = 295.5$). However, $\delta^{15}\text{N}$ values decrease as $^{40}\text{Ar}/^{36}\text{Ar}$ values increase, implying both N and Ar are derived in part from the mantle and sediment compositions.

To constrain mixing relationships between mantle, ASW/air, and sediment-derived- N_2 , we apply the approach of Sano et al. (2001), using $\delta^{15}\text{N}$ and $\text{N}_2/^{3}\text{He}$ values after consideration of the lower N_2/He ratios of the samples (section 6.1) and lack of reported $^{40}\text{Ar}/^{36}\text{Ar}$ values in the RVP and Eger rift regions for comparison:

$$\delta^{15}\text{N}_{\text{measured}} = \delta^{15}\text{N}_{\text{air}} \times f_{\text{air}} + \delta^{15}\text{N}_{\text{mantle}} \times f_{\text{mantle}} + \delta^{15}\text{N}_{\text{sediment}} \times f_{\text{sediment}} \quad (8)$$

$$1/(\text{N}_2/^{3}\text{He})_{\text{measured}} = f_{\text{air}}/(\text{N}_2/^{3}\text{He})_{\text{air}} + f_{\text{mantle}}/(\text{N}_2/^{3}\text{He})_{\text{mantle}} + f_{\text{sediment}}/(\text{N}_2/^{3}\text{He})_{\text{sediment}} \quad (9)$$

$$f_{\text{air}} + f_{\text{mantle}} + f_{\text{sediment}} = 1 \quad (10)$$

where f is a fraction of each component. $\delta^{15}\text{N}_{\text{air}}$, $\delta^{15}\text{N}_{\text{mantle}}$, and $\delta^{15}\text{N}_{\text{sediment}}$ are 0‰, $-5 \pm 2\text{‰}$, and $7 \pm 4\text{‰}$, and $(\text{N}_2/^{3}\text{He})_{\text{air}}$, $(\text{N}_2/^{3}\text{He})_{\text{mantle}}$ and $(\text{N}_2/^{3}\text{He})_{\text{sediment}}$ are 1.1×10^{11} , and 8.9×10^5 , and 1.4×10^{12} , respectively (Sano and Wakita, 1985; Marty, 1995; Marty and Humbert, 1997; Sano et al., 2001). In Fig. 7a, the majority of the MNB $\delta^{15}\text{N}$ values are on the mixing line between mantle and air, and are similar to the KRV samples.

However, most of the data plot left of the mantle-air mixing line on the $\delta^{15}\text{N}$ and N_2/He diagram as was seen in previously reported data from Central America, Indonesia, and

RVP (Zimmer et al., 2004; Clor et al., 2005; Elkins et al., 2006; de Moor et al., 2013). We identify three possible scenarios to account for this observation. First, the $\delta^{15}\text{N}$ values could be negatively shifted due to fractionation between gases and water depending on water temperature. In order to resolve this issue, Lee et al. (2015) proposed that $\delta^{15}\text{N}$ values of dissolved gases in water are negatively fractionated as water temperature increases compared to ambient air (25°C) based on a modelling experiment at temperatures between 5°C and 60°C. Temperatures of the MNB thermal springs range from 36.8 to 83.5°C, which is likely to cause the negative N isotope shift from the mixing line by up to about 1‰. However, most of the corrected $\delta^{15}\text{N}$ values still plot to the left of the mixing line (Fig. 7a), and thus do not fully resolve this issue. Second, the $\delta^{15}\text{N}$ value of MORB ($-5 \pm 2\text{‰}$, Marty and Humbert, 1997) could be inappropriate as an end-member for the mixing lines. Clor et al. (2005) and Elkins et al. (2006) have alternatively taken the extreme $\delta^{15}\text{N}$ values of -15‰ (Mohapatra and Murty, 2004) to resolve this mantle end-member issue. In Fig. 7b, some of the $\delta^{15}\text{N}$ and $\text{N}_2/{}^3\text{He}$ values still plot near the mixing lines with the -15‰ mantle value, suggesting that an extreme mantle end-member is not present beneath the MNB and KRV areas. Finally, the $\text{N}_2/{}^3\text{He}$ ratio of the mantle beneath the MNB may be different from MORB. Bräuer et al. (2004) observed that all of their data ($\delta^{15}\text{N} = -4.4$ to -1.1‰ , $\text{N}_2/{}^3\text{He} = 8.21 \times 10^6 - 3.92 \times 10^8$) from the Cheb basin in the Eger rift plot left of the mantle-air mixing line on a $\delta^{15}\text{N}$ and $\text{N}_2/{}^3\text{He}$ diagram. To resolve this issue, they applied an alternative $\text{N}_2/{}^3\text{He}$ (5×10^6) for the mantle source, European Subcontinental Mantle (ESCM, assumed $R/R_a = 6.5$), which is similar to the upper limit of $\text{N}_2/{}^3\text{He}$ (3.76×10^6) for MORB reported by Marty and Zimmermann (1999). Using the $\text{N}_2/{}^3\text{He}$ of 5×10^6 as the SCLM end member

instead of MORB, the values still show a negative shift of $\delta^{15}\text{N}$ values (Fig. 7c). In Fischer et al. (2009), $\text{N}_2/{}^3\text{He}$ values of Oldoinyo Lengai fumaroles range from 1.88×10^7 to 4.02×10^7 , which is higher than that of ESCM, although $\text{CO}_2/{}^3\text{He}$ ratios (3.6×10^9 to 4.1×10^9) fall in the MORB range (Fischer et al., 2009). Taking the Oldoinyo Lengai values into consideration, we suggest alternative values ($\delta^{15}\text{N} = -5\text{‰}$; $\text{N}_2/{}^3\text{He} = 1.5 \times 10^7$) of the SCLM component beneath the MNB region. Using this end-member, most of the EAR and Cheb basin values are included in the mixing lines (Fig. 7c), which indicates the SCLM beneath the MNB may have a higher $\text{N}_2/{}^3\text{He}$ ratio than ESCM. Also, Mana et al. (2014) proposed that magmatism occurs in lithosphere beneath the northern Tanzania. Overall, these observations are consistent with Lee et al. (2016) who proposed that the volatiles in the MNB are derived from the lower crust and upper mantle, which implies the SCLM could be the source for the mantle-derived volatiles. According to the theoretical mixing equations with the SCLM end-member ($\delta^{15}\text{N} = -5\text{‰}$, $\text{N}_2/{}^3\text{He} = 1.5 \times 10^7$), atmospheric N_2 is significant for both the MNB (up to 90.7% of f_{air}) and KRV (up to 99.9% of f_{air}) (Table 5), as originally noted by Darling et al. (1995) for the KRV. Atmospheric N_2 is dissolved in ASW and dilutes deeper N_2 sources at shallow levels (Giggenbach and Poreda, 1993). However, in Table 5, a component of SCLM-derived N_2 is still significant for some samples in both the MNB (up to 64.9% of f_{mantle}) and KRV (up to 69.0% of f_{mantle}). This is consistent with the N_2 -He-Ar relative abundances showing mantle-derived volatile release in the MNB (Fig. 2), which indicates that SCLM is the likely predominant mantle end-member in this region.

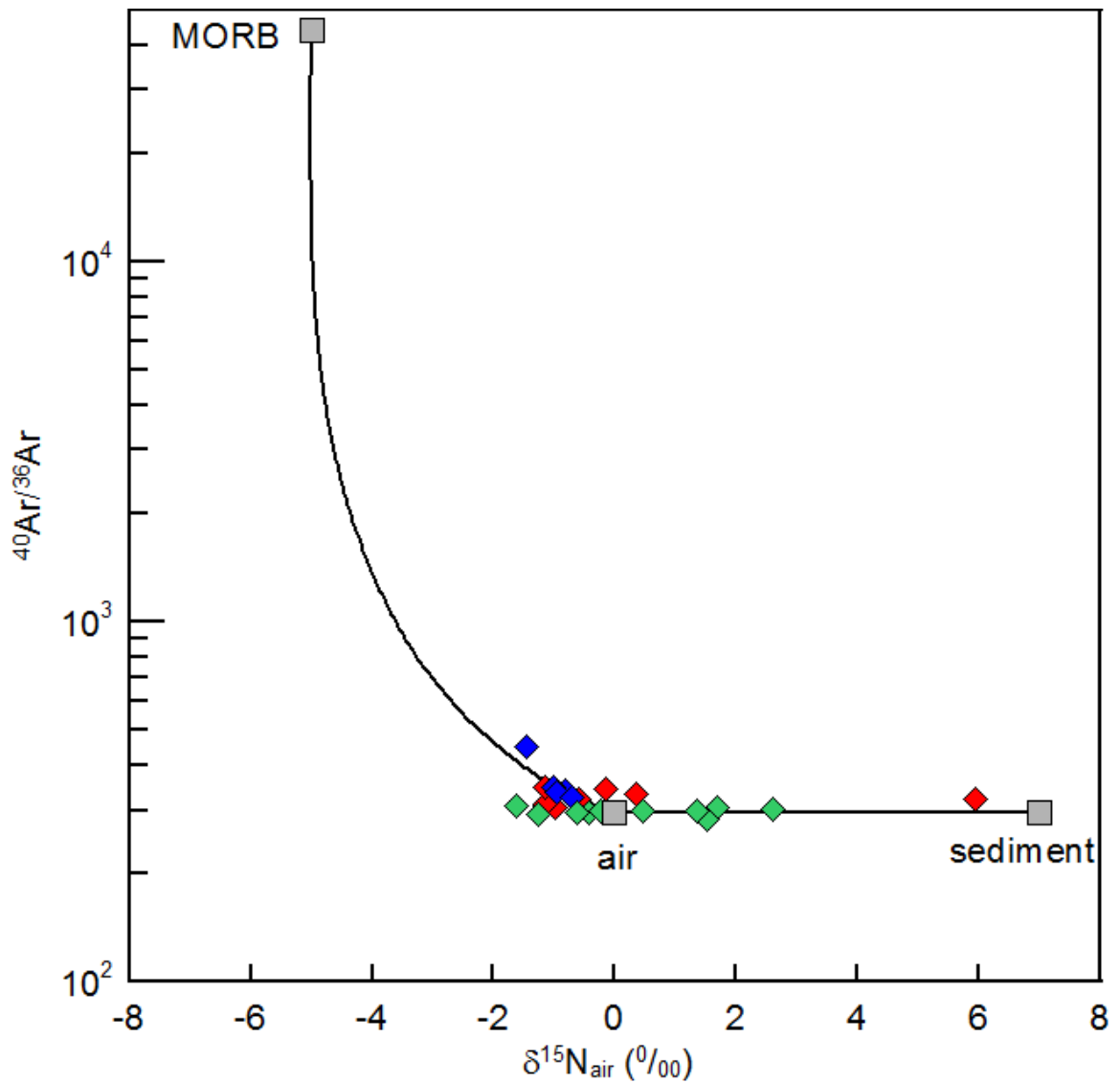
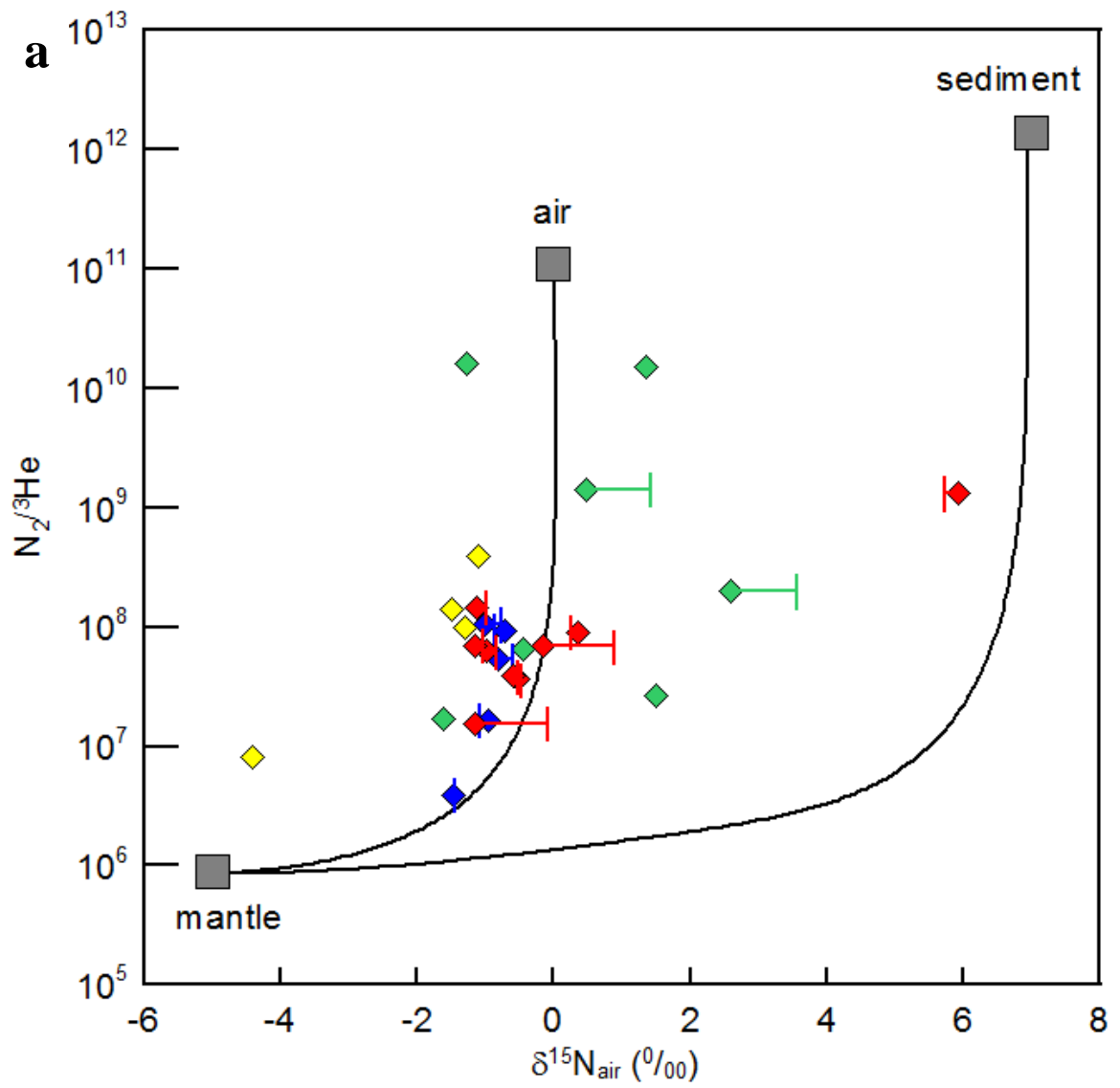
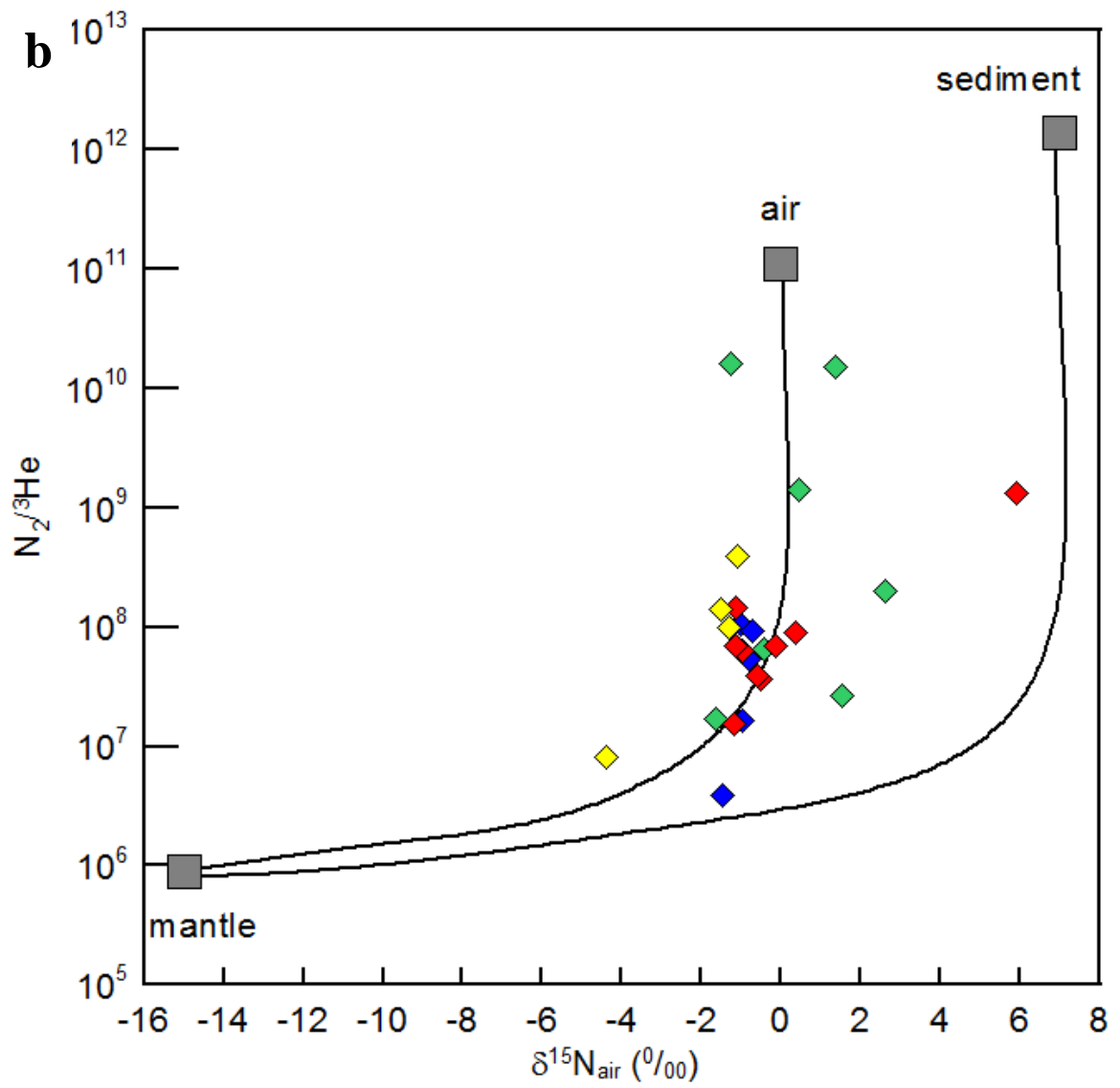


Fig. 6. Plot of $\delta^{15}\text{N}$ and $^{40}\text{Ar}/^{36}\text{Ar}$ values (symbols as in Fig. 4). $\delta^{15}\text{N}$ values of MORB, air, and sediments are -5‰ , 0‰ , $+7\text{‰}$, respectively. The $^{40}\text{Ar}/^{36}\text{Ar}$ value of MORB is 44,000 (Moreira et al., 1998). The $^{40}\text{Ar}/^{36}\text{Ar}$ value of sediment is assumed as the same as air (295.5).





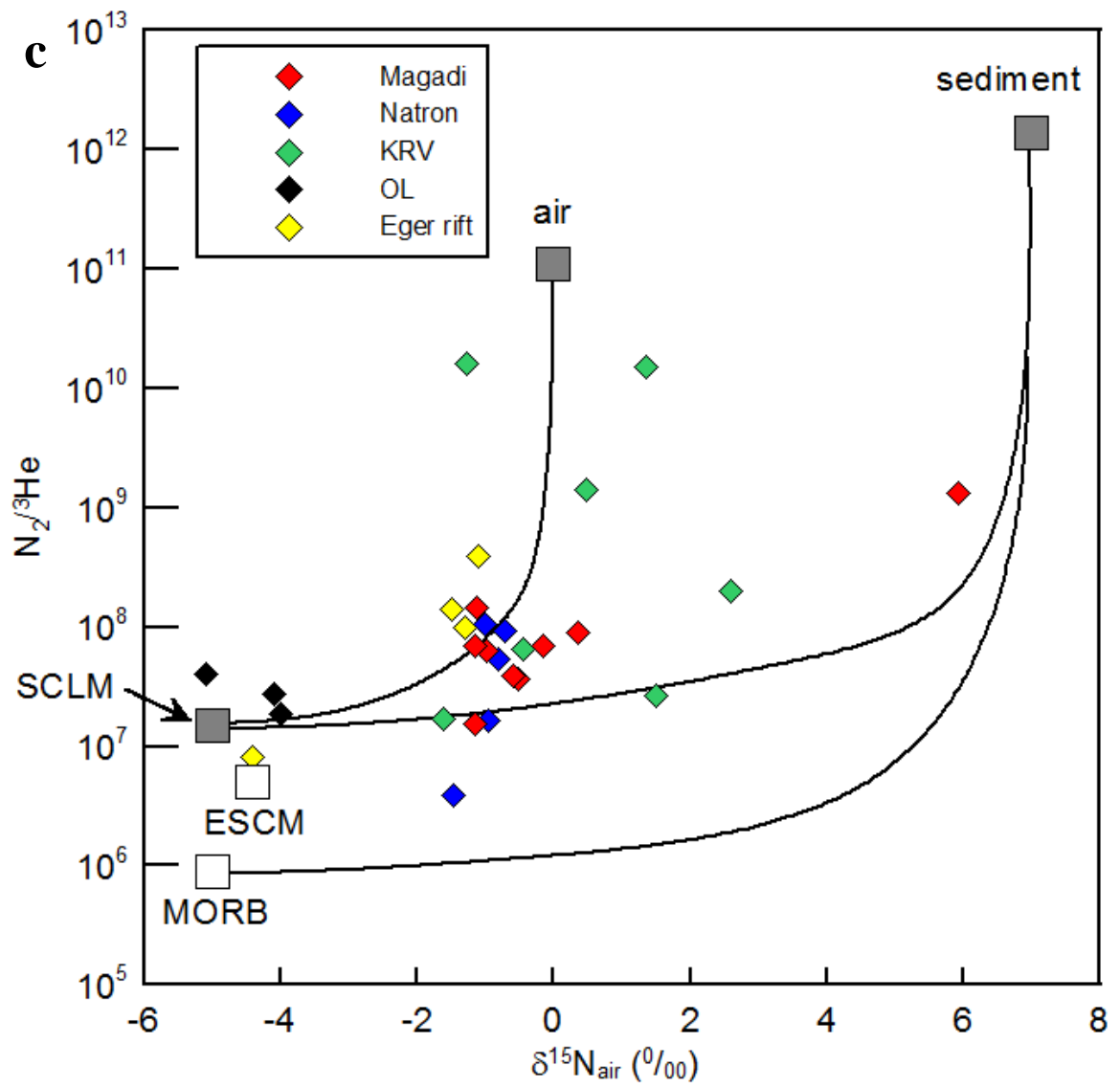


Fig. 7. a. Plot of $\delta^{15}\text{N}$ and $\text{N}_2/{}^3\text{He}$ values. Each mixing line is defined by equations described in section 6.3.2. Yellow diamonds are data from the Cheb basin, Eger rift (Bräuer et al., 2004). Horizontal bars represent corrections considering isotope fractionation between gases and water depending on temperatures as suggested by Lee et al. (2015). Only spring samples ($T < 90^\circ\text{C}$) were corrected. b. Plot of $\delta^{15}\text{N}$ and $\text{N}_2/{}^3\text{He}$ values with the alternative mantle component ($\delta^{15}\text{N} = -15\%$, Mohapatra and Murty, 2004). c. Plot of ${}^{15}\text{N}$ and $\text{N}_2/{}^3\text{He}$ values with the Subcontinental Lithospheric Mantle (SCLM) as a mantle end-member ($\text{N}_2/{}^3\text{He} = 1.5 \times 10^7$). OL means average of Oldoinyo Lengai values represented as black diamonds ($\text{N}_2/{}^3\text{He} = 2.87 \times 10^7$, Fischer et al., 2009).

Table 5. Results of calculated end-member contributions for N₂ and CO₂.

sample ID	N ₂			CO ₂ ^b		
	%f _{mantle} ^a	%f _{sediment}	%f _{air}	%f _{mantle}	%f _{sediment}	%f _{limestone}
KN14-S01	9.3	0.0	90.7	12.7	10.1	77.3
KN14-S02	24.1	3.2	72.8	16.8	8.6	74.6
KN14-S03	21.2	0.0	78.8	17.8	9.7	72.5
KN14-S05	41.1	21.9	37.0	43.3	1.4	55.3
KN14-S06	38.5	19.2	42.3	27.7	4.3	68.0
KN14-S07	16.4	16.8	66.8	17.0	11.2	71.9
KN14-S08	64.9	35.1	0.0	25.9	0.0	74.1
KN14-S09	21.6	13.3	65.1	7.9	1.2	90.9
KN14-S11	1.1	85.5	13.4	1.1	10.5	88.4
TZ14-S01	28.1	8.5	63.4	36.8	2.9	60.4
TZ14-S02	13.6	0.0	86.4	26.9	4.8	68.3
TZ14-S03	60.2	39.8	0.0	93.6	0.0	6.4
TZ14-S05	64.1	35.9	0.0	97.3	0.0	2.7
TZ14-S06	15.9	1.2	82.9	46.2	8.9	44.9
KN13-F01	69.0	31.0	0.0	89.6	0.0	10.4
KN13-F05	23.3	10.5	66.2	11.3	9.6	79.1
KN13-F08	47.7	52.3	0.0	51.4	6.5	42.1
KN13-F13	0.1	0.0	99.9	40.0	14.9	45.2
KN13-F14	0.0	19.3	80.7	4.8	19.7	75.5
KN13-S02	1.0	7.4	91.5	1.8	18.0	80.2
KN13-S03	7.4	42.5	50.1	13.0	8.0	78.9

^aA fraction of SCLM instead of MORB.

^bCO₂/³He ratios of TZ14-S03 and TZ14-S05 are assumed as 2 x 10⁹.

6.3.3. CO₂ sources

$\delta^{13}\text{C}_{\text{CO}_2}$ values of the MNB thermal springs (-5.7 to -3.1‰), except for two Little Magadi thermal springs (1.6 and -0.9‰), overlap with the KRV samples (-7.1 to -3.3‰) (Table 4) and RVP values (-6.45 to -2.79‰, Barry et al., 2013). Darling et al. (1995) suggested that CO₂ from the KRV is derived from the mantle, with $\delta^{13}\text{C}_{\text{CO}_2}$ values ranging from -7.1 to -1.7‰. According to recovered CO₂/³He ratios and $\delta^{13}\text{C}_{\text{CO}_2}$ values, CO₂ sources are quantified by these mixing equations:

$$\delta^{13}\text{C}_{\text{measured}} = \delta^{13}\text{C}_{\text{mantle}} \times f_{\text{mantle}} + \delta^{13}\text{C}_{\text{limestone}} \times f_{\text{limestone}} + \delta^{13}\text{C}_{\text{sediment}} \times f_{\text{sediment}} \quad (11)$$

$$1/(\text{CO}_2/^3\text{He})_{\text{measured}} =$$

$$f_{\text{mantle}}/(\text{CO}_2/^3\text{He})_{\text{mantle}} + f_{\text{limestone}}/(\text{CO}_2/^3\text{He})_{\text{limestone}} + f_{\text{sediment}}/(\text{CO}_2/^3\text{He})_{\text{sediment}} \quad (12)$$

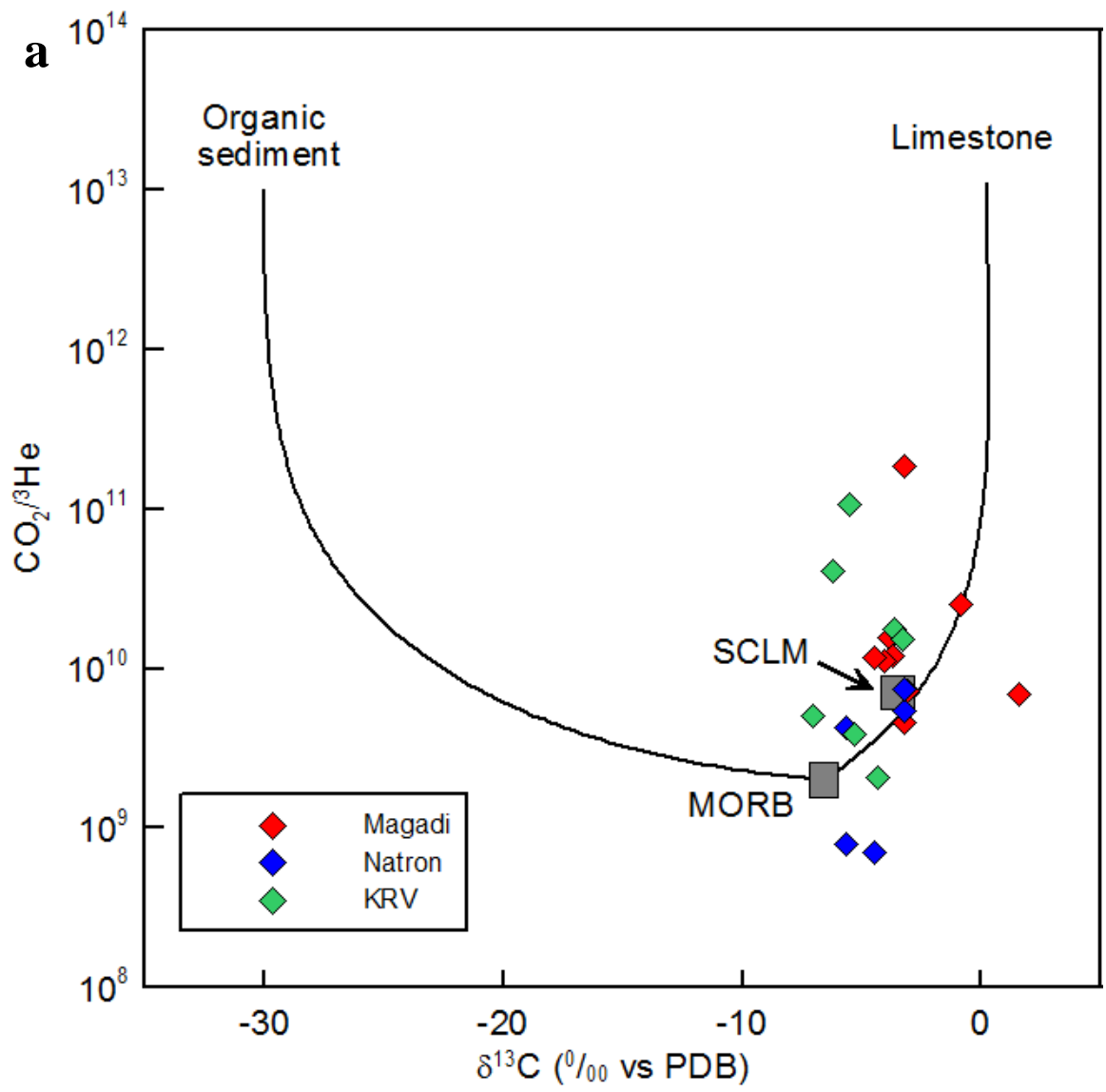
$$f_{\text{mantle}} + f_{\text{limestone}} + f_{\text{sediment}} = 1 \quad (13)$$

where $\delta^{13}\text{C}_{\text{mantle}}$, $\delta^{13}\text{C}_{\text{limestone}}$, and $\delta^{13}\text{C}_{\text{sediment}}$ are -6.5 ± 2.5 , 0, and -30‰, and $(\text{CO}_2/^3\text{He})_{\text{mantle}}$, $(\text{CO}_2/^3\text{He})_{\text{limestone}}$, and $(\text{CO}_2/^3\text{He})_{\text{sediment}}$ are 2.0×10^9 , 1×10^{13} and 1×10^{13} , respectively (Marty and Jambon, 1987; Sano and Marty, 1995). For individual samples from both the MNB and KRV areas, CO₂ sources are primarily either mantle (up to 97%) or crustal limestone (up to 90.9%) without significant sediment input which is less than 20% for all samples (Table 5). Heavier $\delta^{13}\text{C}_{\text{CO}_2}$ values are observed in two Little Magadi springs likely due to dissolution of CO₂ from carbonate rocks surrounding aquifer systems, which has been suggested for similar lithologies in the US (Crossey et al., 2009; Sherwood-Lollar and Ballentine, 2009; Zhou et al., 2012).

Most of the MNB and KRV samples have elevated CO₂/³He ratios relative to MORB values (1×10^9 - 6×10^9 , Marty and Zimmermann, 1999). In Fig. 8a, CO₂/³He ratios and

dissolved ^4He concentrations of the MNB thermal springs (Table 6) show a negative correlation, and a majority of values plot above the MORB range, except for two samples ($\text{CO}_2/{}^3\text{He} < 1 \times 10^9$). This may be attributed to He loss or CO_2 addition. First, He is significantly less soluble than CO_2 in water (Ozima and Podosek, 1983; Bräuer et al., 2013). However, there is no bubbling gas in the MNB thermal springs. Moreover, a vapor phase is unlikely to be produced because water temperatures are lower than 100°C (Table 1), making preferential partitioning of He into vapor unlikely. In the case of the KRV samples, it is plausible to lose He because bubbles were observed in two springs, and temperatures of fumaroles are high enough to separate a vapor phase (Table 1). Second, additional CO_2 has affected the elevated $\text{CO}_2/{}^3\text{He}$ ratios. This additional CO_2 could be derived from crust that is a mixture of both limestone and organic sediments, but these rocks are minor in surface outcrops (Table 5). A more likely scenario is that the CO_2 is SCLM-dominated in the MNB area consistent with Lee et al. (2016) who suggested that the deep source of CO_2 appears to be the lower crust and upper mantle. Dunai and Porcelli (2002) reported a wide range of $\text{CO}_2/{}^3\text{He}$ ratios ($\sim 10^9$ to $\sim 10^{13}$) from worldwide-sampled SCLM xenoliths implying additional CO_2 could be derived from SCLM. Bräuer et al. (2016), based on their selected samples, proposed higher $\delta^{13}\text{C}$ and $\text{CO}_2/{}^3\text{He}$ values ($\delta^{13}\text{C} = -3.5\text{‰}$, $\text{CO}_2/{}^3\text{He} = 7 \times 10^9$) than MORB for the ESCM. To determine SCLM compositions in the MNB, we selected samples with values of $\delta^{13}\text{C} < -2\text{‰}$ and $2 \times 10^9 < \text{CO}_2/{}^3\text{He} < 1 \times 10^{11}$ as well as taking Oldoinyo Lengai samples (Fischer et al., 2009), because the $\delta^{13}\text{C}$ values of SCLM xenoliths range from -2 to -8‰ (Cartigny, 2005), and crustal $\text{CO}_2/{}^3\text{He}$ ratios are $> 1 \times 10^{11}$ (Barry et al., 2013). Based on these constraints, we suggest that the

MNB area has SCLM compositions ($\delta^{13}\text{C} = -3.5\%$ and $\text{CO}_2/{}^3\text{He} = 7.31 \times 10^9$) similar to ESCM. Two samples with lower $\text{CO}_2/{}^3\text{He}$ ratios (Fig. 8b) probably gained more radiogenic ${}^4\text{He}$ compared to the amount of CO_2 loss (Table 4).



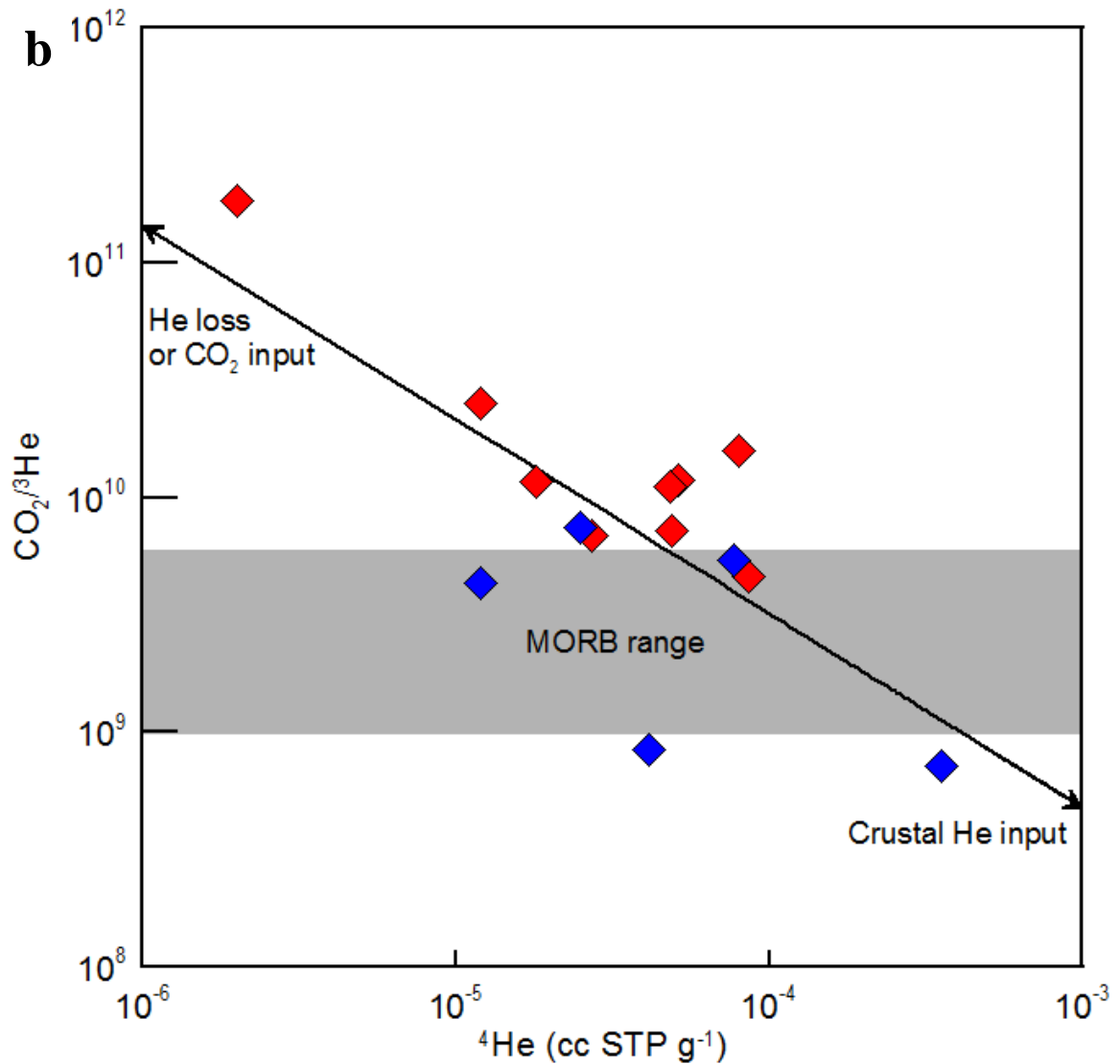


Fig. 8. a. Plot of $\delta^{13}\text{C}$ values of CO_2 versus $\text{CO}_2/{}^3\text{He}$ ratios. The mixing line is defined by equations in section 6.3.3. SCLM is defined by $\delta^{13}\text{C}$ (-3.5‰) and $\text{CO}_2/{}^3\text{He}$ (7×10^9) values of both European Subcontinental Mantle (ESCM, Bräuer et al., 2016) and average values of the selected MNB/Oldoinyo Lengai samples. **b.** Plot of dissolved ${}^4\text{He}$ concentrations versus $\text{CO}_2/{}^3\text{He}$ ratios of the MNB thermal springs. The gray area is the range of the $\text{CO}_2/{}^3\text{He}$ ratios of MORB (1×10^9 to 6×10^9 , Marty and Zimmermann, 1999).

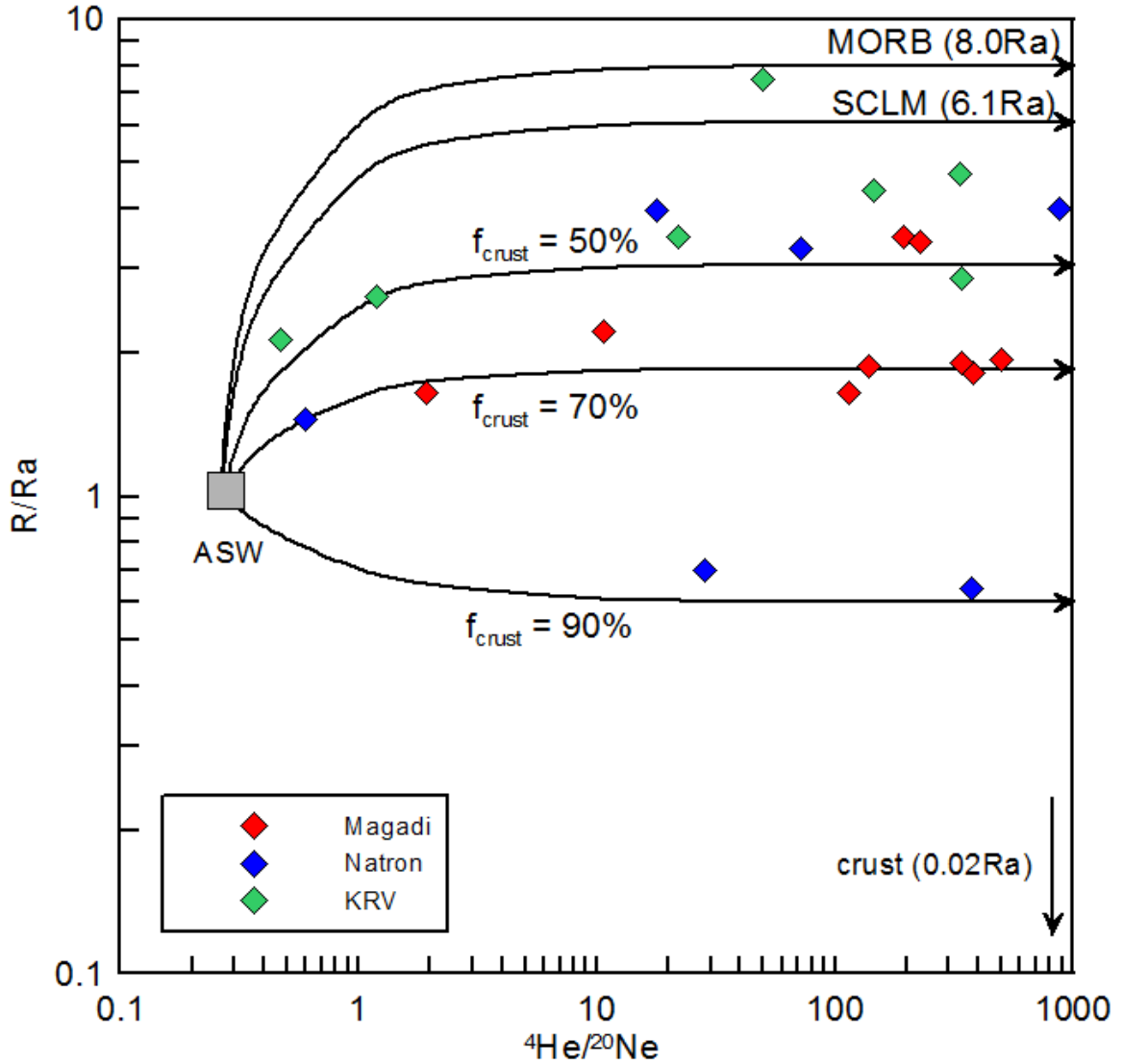


Fig. 9. Plot of R/Ra versus ${}^4\text{He}/{}^{20}\text{Ne}$ ratios. Mixing lines represent binary mixing relationships between ASW and end members which have different fractions of crustal He ($\%f_{\text{crust}}$). SCLM is selected as the mantle source for the MNB, showing most of the MNB and KRV samples are enveloped except for Silali that is the northernmost location of this study.

6.4. Helium sources

All Rc/Ra ratios of the MNB thermal springs are greater than 0.1 (Table 4), which implies that the mantle-derived fluids have relatively short residence time in the crust during transport to the shallow subsurface (Ballentine et al., 2002). However, the highest $^3\text{He}/^4\text{He}$ ratio observed (4.0 Ra) is still lower than both the ratios for SCLM (6.1 ± 0.9 Ra, Gautheron and Moreira, 2002) and for MORB (8.0 ± 1.0 Ra, Graham, 2002), showing a plume signature (9 – 20 Ra, Marty et al., 1996) is unlikely detected in the MNB. Although a MORB $^3\text{He}/^4\text{He}$ ratio is observed at the Silali volcano fumaroles (7.49 and 8.00 Ra) in the KRV (Darling et al., 1995; this study), the highest reported $^3\text{He}/^4\text{He}$ ratio of 6.86 Ra at Oldoinyo Lengai is lower than the MORB value (Fischer et al., 2009). Additionally, Hopp et al. (2007) showed that at Chyulu Hills in south Kenya, an active off-axis volcanic field ~100 km east of the study region, $^3\text{He}/^4\text{He}$ ratios of mantle xenoliths (5.62 to 7.59 Ra) are within the range of SCLM. Moreover, SCLM-related He-Ne systematics are found in mantle xenoliths and basaltic rocks in the southern Kenya rift (Halldórsson et al., 2014).

Lithospheric thickness decreases with increasing extension and heating. Along-strike variations in lithospheric thickness associated with southward younging (Magadi < 7 Ma and Natron < 3 Ma, Crossley, 1979; Foster et al., 1997), may be factor in the variations we see. It is likely that SCLM-derived volatiles instead of MORB-type volatiles are contributing to the MNB hydrothermal system, which is consistent the model suggested by Mana et al. (2014). Taking the SCLM value as the mantle end member we can quantify He sources of the MNB thermal springs. Mantle contributions to each thermal spring source are calculated by the following equation:

$$f_{\text{mantle}} = [(Rc/Ra)_{\text{measured}} - (R/Ra)_{\text{crust}}] / [(R/Ra)_{\text{SCLM}} - (R/Ra)_{\text{crust}}] \quad (14)$$

$$f_{\text{crust}} = 1 - f_{\text{mantle}} \quad (15)$$

where f_{mantle} is a fraction of mantle-derived He, and $(R/Ra)_{\text{SCLM}}$ and $(R/Ra)_{\text{crust}}$ are $^3\text{He}/^4\text{He}$ ratios of SCLM ($6.1 \pm 0.9 \text{ Ra}$, Gautheron and Moreira, 2002) and crust (0.02Ra , Ozima and Podosek, 1983), respectively. The f_{crust} values range from 34 to 90%, showing that significant amounts of continental crustal fluids have been incorporated into the MNB hydrothermal systems (Fig. 9). In volcano-hydrothermal systems, it has been shown that $^3\text{He}/^4\text{He}$ ratios decrease with distance from the volcanic center due to the increasing contribution of ^4He -rich groundwaters from crustal sources (Sano and Fischer, 2013). Underneath the MNB, Precambrian metamorphic basement rocks (Archean Tanzanian craton and late Proterozoic Mozambique belt) are covered by Pliocene-Pleistocene trachyte (Baker et al., 1986; Ebinger et al., 1997), likely containing abundant U and Th to produce radiogenic ^4He . Therefore, we suggest it is likely that the MNB thermal springs, with lower $^3\text{He}/^4\text{He}$ ratios, have been affected by interactions with ^4He -rich groundwater. The highest $^3\text{He}/^4\text{He}$ ratios are observed at the Little Magadi (up to 3.5 Ra) and eastern Natron (up to 4.0 Ra) areas (Fig. 1), implying less interaction with ^4He -rich groundwater, and possibly lower residence times in the crust; consequently, we suggest these springs are in close proximity to the primary conduits for deeply sourced volatiles. This is supported by the occurrence of recent seismic swarm in the Little Magadi region in 1997-1998, which may have represented the migration of magmatic fluids within a developing fracture network (Ibs-von Seht et al., 2001). Similarly, in the eastern Natron area the highest $^3\text{He}/^4\text{He}$ ratio (4.0 Ra) is adjacent to the Gelai magmatic-tectonic event in 2007 (Fig. 1). Since this event, the region has been subject to ongoing earthquake activity, with frequently occurring NE-trending swarms of relatively low magnitude earthquakes ($M_w < 4.5$) occurring between

Oldoinyo Lengai and the northern flanks of Gelai (Lee et al., 2016; Weinstein et al., submitted). Consistent with interpretations of seismic swarms elsewhere in the EAR (e.g., Albertine and Manyara basins; Lindenfeld et al., 2012; Albaric et al., 2014), this seismicity may represent hydraulic fracturing in response to high fluid pressures resulting from volatile release from underlying magma bodies (Lee et al., 2016; Weinstein et al., submitted).

6.5. Continental ^4He flux

In the MNB, a number of thermal springs discharge along fault zones, releasing volatiles (N_2 , CO_2 , and He). As stated above, the MNB thermal springs show higher He contents, which are likely affected by release of radiogenic He through alpha decay of U and Th from the Archean Tanzanian craton and Mozambique Proterozoic metamorphic belt (Danabalan et al., 2016). The radiogenic ^4He flux values of the MNB thermal springs are calculated as:

$$\phi^4\text{He} = 6.022 \times 10^{23} / 22,400 \times \phi_{\text{spring}} \times [^4\text{He}] \quad (16)$$

where $\phi^4\text{He}$ is a flux rate of ^4He (as atoms $\text{m}^{-2} \text{sec}^{-1}$), ϕ_{spring} is each flow rate of spring in the MNB reported by Crane (1981) and Crane and O'Connell (1983) (Table 6), and $[^4\text{He}]$ is the concentration of ^4He dissolved in each spring sample (Table 6). The calculated spring $\phi^4\text{He}$ range from 3.74×10^{11} to 3.34×10^{14} atoms $\text{m}^{-2} \text{sec}^{-1}$, which is four orders of magnitude higher than the global continental ^4He flux compiled from calculated results of helium excesses in lakes and aquifers as well as gradients in gas wells (2.8×10^{10} atoms $\text{m}^{-2} \text{sec}^{-1}$, O'Nion and Oxburgh, 1988). In order to account for higher spring ^4He flux than the

expected production rate through alpha decay of U and Th, the host rocks must release their accumulated radiogenic He (Lowenstern et al., 2014). Caracausi and Paternoster (2015) suggested that high crustal ^4He flux may be a temporal effect after moderate to large magnitude earthquakes to cause intense rock fracturing.

The mean of continental ^4He fluxes of the MNB springs (5.86×10^{13} atoms m^{-2} sec^{-1}) is greater than that of the global ^4He flux (4.18×10^{10} atoms m^{-2} sec^{-1} , Torgersen, 2010) calculated from reported measurements in various geological environments (e.g., lakes, groundwater basins, and volcanic areas) by a factor of $\sim 1,000$. According to the approach of Torgersen (2010), the ^4He flux of the MNB can be subdivided into mantle and crustal flux values (Table 6). Using this approach, the MNB spring ^4He fluxes ($2.8 \times 10^{10} - 2.5 \times 10^{14}$ atoms m^{-2} sec^{-1}) (Table 6) are higher than the previously reported tectonic strain values ($2.0 \times 10^9 - 1.8 \times 10^{11}$ atoms m^{-2} sec^{-1} , Torgersen, 2010), which suggests that fracturing released crustal ^4He . A swarm of teleseismic earthquakes of magnitude greater than 5 occurred in 2007 in the southern Natron basin, but no earthquakes of magnitude > 4.5 have occurred in the Magadi basin in historic time (e.g., Weinstein et al., submitted). Observed spatial variations, therefore, are not well explained by the intense fracturing model.

Torgersen (2010) separated worldwide-reported ^4He fluxes into regions of volcanic and tectonic-strain, considering that the continental ^4He flux increases due to releasing ^4He from fracturing of rocks by tectonic strain or additional mantle helium via magmatism. Higher continental ^4He flux values are found in volcanic areas, such as Lake Nyos (3.0×10^{14} atoms m^{-2} sec^{-1} , Kipfer et al., 2002), Laacher See (1.0×10^{13} atoms m^{-2} sec^{-1} , Kipfer et al., 2002) and Yellowstone (3.16×10^{13} atoms m^{-2} sec^{-1} , Lowenstern et al., 2014). Also, the mantle ^4He fluxes of the MNB ($4.2 \times 10^{11} - 7.5 \times 10^{13}$ atoms m^{-2} sec^{-1}) are higher than

the range of tectonic strain region values ($1.0 \times 10^6 - 3.5 \times 10^{10}$ atoms $\text{m}^{-2} \text{sec}^{-1}$, Torgersen, 2010), indicating that the addition of mantle ^4He has occurred. Similarly, other volcanic areas show higher mantle ^4He fluxes that range between 3.23×10^9 atoms $\text{m}^{-2} \text{sec}^{-1}$ and 1.96×10^{14} atoms $\text{m}^{-2} \text{sec}^{-1}$ (e.g., Taiwan, Yellowstone, and Lake Nyos). When plotted on an empirical ^4He flux diagram, the MNB ^4He flux data appears more representative of volcanic areas rather than tectonic strain (Fig. 10).

Magma intrusions transfer heat to the crust, and repeated dike intrusions lead to a reduction in strength locally (e.g., Buck, 2004; Daniels et al., 2014; Muirhead et al., 2016). New and existing seismic data from the Magadi and Natron basins indicate regular magma intrusions (e.g., dikes and sills) into the crust within the central basins, and evidence for one or more lower crustal magma chambers (Calais et al., 2008; Biggs et al., 2009; Weinstein et al., submitted). Thus we suggest magma intrusions likely play a key role in supplying and transporting mantle ^4He , and related heating and fracturing release crustal ^4He from Archean Tanzanian craton and/or the late Proterozoic Mozambique belt into the fluids in the MNB.

6.6. Mantle-derived volatile fluxes in the MNB hydrothermal system

Finally, it is likely that a number of thermal springs release mantle-derived volatiles (^3He , N_2 , and CO_2). Fluxes of these mantle-derived volatiles transferred by fluids has not yet been calculated, although a massive amount of CO_2 (4.05 Mt/yr) from diffuse degassing along the faults in the MNB has been reported (Lee et al., 2016). Using our results from the MNB thermal springs and $\phi^4\text{He}$ values calculated, the fluxes of fluid-derived ^3He , N_2 , and CO_2 can be acquired using these equations:

$$\phi^3\text{He} = \phi^4\text{He} \times (^3\text{He}/^4\text{He}) \quad (17)$$

$$\phi\text{N}_2 = \phi^3\text{He} \times \text{N}_2/^3\text{He} \times f_{\text{N}_2\text{-mantle}} \quad (18)$$

$$\phi\text{CO}_2 = \phi^3\text{He} \times \text{CO}_2/^3\text{He} \times f_{\text{CO}_2\text{-mantle}} \quad (19)$$

where $\phi^3\text{He}$, ϕN_2 , and ϕCO_2 are flux rates (atoms $\text{m}^{-2} \text{sec}^{-1}$) of ^3He , N_2 , and CO_2 , respectively. ϕ_{spring} is the flow rate of each spring (Crane, 1981; Crane and O'Connell, 1983), and $f_{\text{N}_2\text{-mantle}}$ and $f_{\text{CO}_2\text{-mantle}}$ are the contribution of mantle end-member to N_2 and CO_2 , respectively (Table 6). Total flux values ($\Phi^3\text{He}$, ΦN_2 , and ΦCO_2) were calculated in the MNB thermal area, (1,193.2 km^2 , Crane, 1981; Crane and O'Connell, 1983), which exclude areas without samples in this study. The values of ^3He , N_2 , CO_2 are 8.18 mol/yr, 4.07×10^7 mol/yr and 5.31×10^9 mol/yr, respectively (Table. 6). The total ϕCO_2 and $\phi^3\text{He}$ values are better constrained than previously reported values (total CO_2 flux = 5.0×10^8 mol/yr; total ^3He flux = 0.46 mol/yr) of the Natron area as reported by Barry et al. (2013) because more samples were collected over a wider region. In comparison with the global fluxes ($\Phi^3\text{He} = 640$ mol/yr; $\Phi\text{N}_2 = 2.88 \times 10^{10}$ mol/yr; $\Phi\text{CO}_2 = 2.20 \times 10^{12}$ mol/yr, Marty, 1995; Marty and Tolstikhin, 1998; Fischer, 2008; Bianchi et al., 2010; Kagoshima et al., 2015), $\Phi^3\text{He}$, ΦN_2 , and ΦCO_2 of the MNB thermal springs constitute 1.28%, 2.04% and 0.24%, respectively (Table 6). In the MNB, the total flux of mantle-derived CO_2 (0.23 Mt/yr) from the thermal springs is significantly lower than the total flux of diffuse CO_2 degassing (4.05 Mt/yr, Lee et al., 2016). This implies that many faults, or segments along individual fault structures, that are not actively releasing fluids at the surface in the MNB may still act as conduits for CO_2 transport from deep sources.

6.7. Geochemical implications for continental rifting

The MNB area is a young section of the EAR (section 2), and the hydrothermal system shows a variety of geochemical features of incipient magmatic rifting. Our isotope modeling of N₂ (Fig. 7c) and CO₂ (Fig. 8a) sources shows that MORB is inappropriate as a mantle end-member. Instead, the SCLM is more likely the primary magma source beneath the MNB (Fig. 11), which is also consistent with observations in a magmatic Eger rift in the European continent (Bräuer et al., 2004; Bräuer et al., 2013). Additionally, ³He/⁴He ratios of the MNB thermal springs (0.64 – 4.00 Ra) (Table 4) and Oldoinyo Lengai (6.68 – 6.86 Ra, Fischer et al., 2009) support the contribution of SCLM (6.1 ± 0.9 Ra, Gautheron and Moreira, 2002) beneath the MNB. As discussed in section 6.5, SCLM-derived volatiles are supplied and transported by magma intrusions that also heat and fracture host rocks to release crustal volatiles (Fig. 11). The mixture of SCLM and crustal volatiles is contaminated by atmospheric components in ASW or air-infiltration in the shallow subsurface (Fig. 11). The SCLM-derived volatiles in the MNB support the rift development model of Ebinger (2005), which suggests that the asthenosphere (MORB-type mantle) replaces a relatively small volume of SCLM during the early stage of continental rifting. Further south in Tanzania, near the southern end of the eastern rift, ³He/⁴He ratios are all < 0.1 (0.039 – 0.053 Ra) and dominantly crustal (Danabalan et al., 2016). This implies that a smaller fraction of lithosphere is replaced by the asthenosphere underneath the youngest sectors of the eastern rift.

7. CONCLUSIONS

Our results show new data of gas chemistry and isotopes (O, H, N, C, and He) of the MNB thermal springs. Dissolved gases are a mixture of deep (mantle-derived) and shallow (air/ASW) sources according to the N₂-He-Ar systematics. Equilibrated temperatures of the hydrothermal systems range from ~100 to ~150°C using the log(H₂/Ar*) and log(CH₄/CO₂) geothermometers. N₂ is mostly atmospheric with minor mantle-derived contribution. CO₂ which is the most abundant gas component in the MNB thermal springs is contributed by both mantle and limestone, similar to the KRV samples. Helium is derived from both mantle and crust. However, SCLM can be the dominant mantle source for N₂, CO₂, and He in the MNB, with the contribution of continental crust. The higher continental ⁴He flux values in the MNB relative to the mean global continental flux suggest that magma intrusion, and related heating and fracturing, releases additional mantle and crustal helium into the hydrothermal system. Fluxes of mantle-derived volatiles (³He, N₂, and CO₂) represent 1.28%, 2.04%, and 0.24% of global fluxes. Our results suggest the MNB thermal springs discharge magmatic volatiles from SCLM, which significantly interacted with continental crust and demonstrate that a small volume of SCLM is replaced by the asthenosphere during the incipient stages of continental rifting (< 10 Ma) in the EAR.

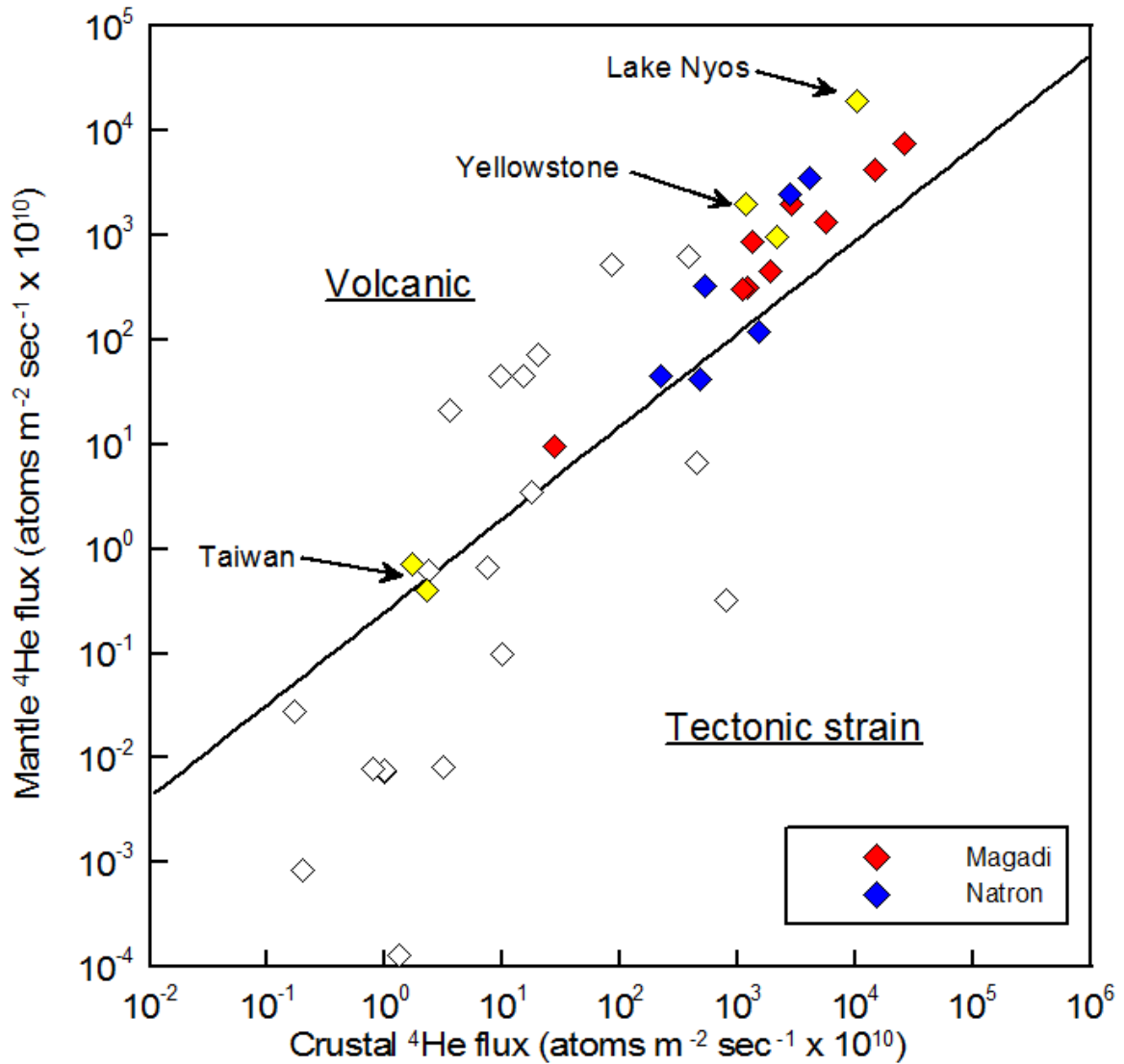


Fig. 10. Plot of crustal versus mantle ^4He fluxes, following Torgersen (2010). White and yellow diamonds represent previously reported locally volcanic and continental ^4He flux values, respectively (Torgersen, 2010; Lowenstern et al., 2014; references therein). The solid line divides ^4He flux values into volcanic and tectonic strain regions.

Table 6. Fluxes of volatiles in the MNB.

sample ID	Location	^4He (ccSTP/g)	Spring flow ^a	$\phi^4\text{He}$ ($\times 10^{12}$)	$\phi^4\text{He}_m$ ($\times 10^{10}$) ^b	$\phi^4\text{He}_c$ ($\times 10^{10}$) ^b	$\phi^3\text{He}$ ($\times 10^8$)
		($\times 10^{-5}$)	($\text{g m}^{-2} \text{sec}^{-1}$)	(atoms $\text{m}^{-2} \text{sec}^{-1}$)			
KN14-S01	Magadi W	8.0	0.011	23.71	454	1917	0.55
KN14-S02		5.1	0.011	15.23	320	1203	0.39
KN14-S03		4.8	0.011	14.06	307	1099	0.37
KN14-S05	Magadi S	8.6	0.145	334.08	7,522	25,886	9.08
KN14-S06		4.9	0.145	189.37	4,165	14,772	5.03
KN14-S07		1.8	0.145	70.02	1,335	5,667	1.61
KN14-S08	Little Magadi	2.7	0.069	49.15	2,005	2,910	2.41
KN14-S09		1.2	0.069	22.1	880	1,330	1.06
KN14-S11	Magadi E	0.2	0.009	0.37	10	28	0.01
TZ14-S01	Natron	7.7	0.008	16.35	119	1,516	0.15
TZ14-S02		2.5	0.008	5.25	42	483	0.05
TZ14-S03		35.5	0.008	75.99	3,537	4,062	4.25
TZ14-S04		24.6	0.008	52.56	2,434	2,822	2.93
TZ14-S05		4.1	0.008	8.67	332	535	0.4
TZ14-S06		1.2	0.008	2.65	44	221	0.05
				mean			
				58.64	1567.07	4296.73	

Table 6. (continued).

Location	Area ^a (km ²)	$\Phi^3\text{He}$	ΦN_2 (x10 ⁶)	ΦCO_2 (x10 ⁹)
		Total flux (mol yr ⁻¹) ^c		
Magadi W	11.6	0.026	0.03	0.05
Magadi S	5.6	0.154	0.21	0.31
Little Magadi	13	0.118	0.16	0.22
Magadi E	10	0.001	0.05	0.00003
Natron	1,153	7.88	8.23	4.73
		sum		
		8.18	40.7	5.31
		Global ^d		
		640	2,000	2,200
		% vs Global ^d		
		1.28	2.04	0.24

^aAreas which are associated with thermal springs and flow rates are reported in Crane (1981) and Crane and O'Connell (1983).

^b $\phi^4\text{He}_m$ and $\phi^4\text{He}_c$ represent mantle-sourced and crustal-sourced ⁴He fluxes, respectively. Calculated mantle-sourced and crustal-sourced ⁴He fluxes, using ³He/⁴He ratios of 1.2 x10⁻⁵ and 2.0 x10⁻⁸, respectively (Torgersen, 2010).

^cTotal flux of each component which is calculated by summation of average of each different location.

^dGlobal fluxes from Marty (1995), Marty and Tolstikhin (1998), Fischer (2008), Bianchi et al. (2010), and Kagoshima et al. (2015).

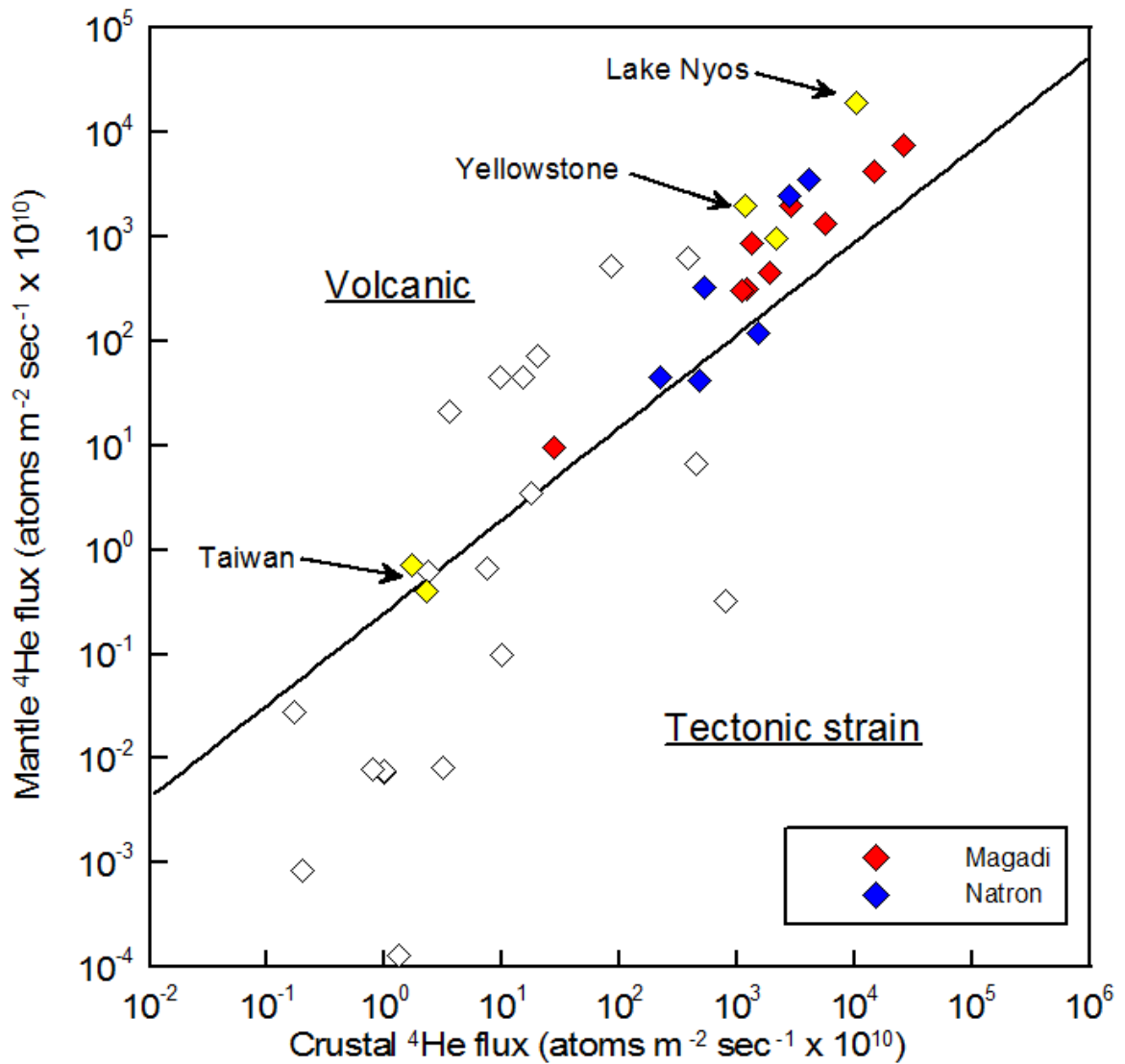


Fig. 10. Plot of crustal versus mantle ^4He fluxes, following Torgersen (2010). White and yellow diamonds represent previously reported locally volcanic and continental ^4He flux values, respectively (Torgersen, 2010; Lowenstern et al., 2014; references therein). The solid line divides ^4He flux values into volcanic and tectonic strain regions.

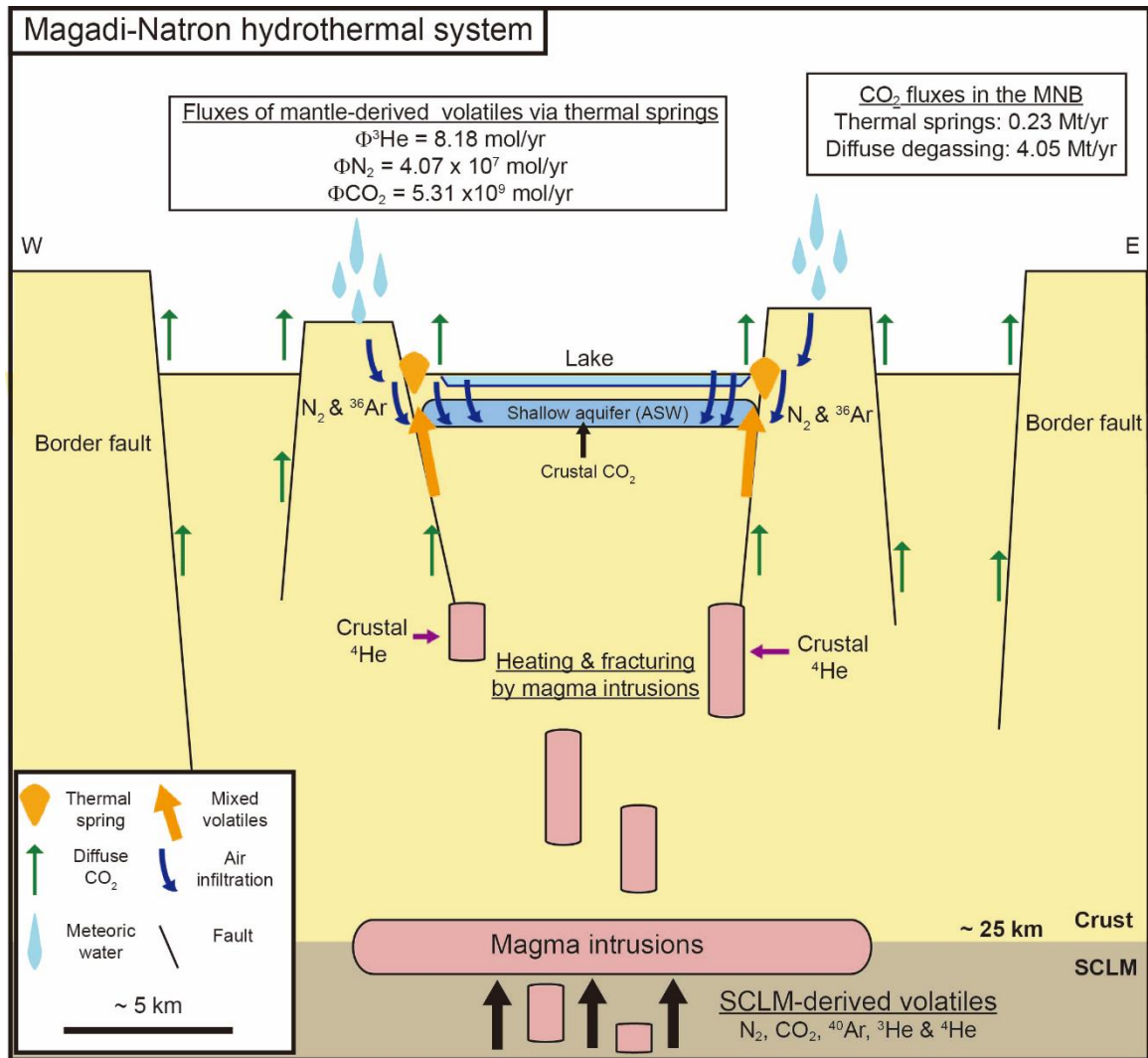


Fig. 11. Schematic illustration of the MNB hydrothermal system releasing mixed volatiles with SCLM, crust, and ASW end-members based on the results. Major lakes in the MNB (Magadi, Little Magadi, and Natron) are fed by the thermal springs. Mantle-derived N₂ and Ar are significantly affected by ASW. Helium is SCLM-derived, but has been masked by radiogenic ⁴He. Total fluxes of mantle-derived volatiles associated with thermal springs are reported in Table 6. Total flux of diffuse CO₂ degassing along fault zones in the MNB are reported in Lee et al. (2016).

8. REFERENCES

- Albaric, J., Déverchère, J., Perrot, J., Jakovlev, A., and Deschamps, A. (2014) Deep crustal earthquakes in North Tanzania, East Africa: interplay between tectonic and magmatic processes in an incipient rift. *Geochem. Geophys. Geosyst.* **15** (2), 374–394.
- Allard, P. (1983) The origin of hydrogen, carbon, sulfur, nitrogen, and rare gases in volcanic exhalations: evidence from isotope geochemistry. *In: Forecasting volcanic events* (eds. H. Tazieff and J. C. Sabroux), Elsevier, Amsterdam, 337–386.
- Allard, P., Jean-Baptiste, P., D’Alessandro, W., Parello, F., Parisi, B., and Flehoc, C. (1997) Mantle-derived helium and carbon in groundwaters and gases of Mount Etna, Italy. *Earth Planet. Sci. Lett.* **148**, 501-516.
- Allen, D. J., Darling, W. G., and Burgess, W. G. (1989) Geothermics and hydrogeology of the southern part of the Kenya Rift Valley. *British Geol. Surv, Res. Rep.* **SD/89/1**.
- Baker, B.H. (1986) Tectonics and volcanism of the southern Kenya Rift Valley and its influence on rift sedimentation. In: Frostick, L.E., Renaut, R.W., Reid, I., Tiercelin, J.J. (Eds.), *Sedimentation in the African Rifts: Geol. Soc. Spec. Pub.* **25**. pp. 45-57.
- Baker, B.H. (1987) Outline of the petrology of the Kenya rift alkaline province. In: Fitton, J.G., Upton, B.G.J. (Eds.), *Alkaline Igneous Rocks. Geological Society London Special Publications* **30**, pp. 293-311.
- Ballentine, C. J., Burgess, R., and Marty, B. (2002) Tracing fluid origin, transport and

- interaction in the crust. *Rev. Mineral. Geochem.* **47**, 539-614.
- Barry, P. H., Hilton, D. R., Fischer, T. P., de Moor, J. M., Mangasini, F., and Ramirez, C. (2013) Helium and carbon isotope systematics of cold “mazuku” CO₂ vents and hydrothermal gases and fluids from Rungwe Volcanic Province, southern Tanzania. *Chem. Geol.* **339**, 141-156.
- Benavente, O., Tassi, F., Reich, M., Aguilera, F., Capecchiacci, F., Gutiérrez, F., Vaselli, O., and Rizzo, A. (2016) Chemical and isotopic features of cold and thermal fluids discharged in the Southern Volcanic Zone between 32.5°S and 36°S: Insights into the physical and chemical processes controlling fluid geochemistry in geothermal systems of Central Chile. *Chem. Geol.* **420**, 97–113.
- Bianchi, D., Sarmiento, J. L., Gnanadekisan, A., Key, M. R., Schlosser, P. and Newton, R. (2010) Low helium flux from the mantle inferred from simulations of oceanic helium isotope data. *Earth Planet. Sci. Lett.* **297**, 379–386.
- Biggs, J., Amelung, F., Gourmelen, N., Dixon, T. H., and Kim, S. W. (2009) InSAR observations of 2007 Tanzania rifting episode reveal mixed fault and dyke extension in an immature continental rift. *Geophys. J. Int.* **179**, 549-558.
- Bräuer, K., Kämpf, H., Niedermann, S., Strauch, G., and Weise, S.M. (2004) Evidence for a nitrogen flux directly derived from the European subcontinental mantle in the Western Eger Rift, Central Europe. *Geochim. Cosmochim. Acta* **68**, 4935–4947.
- Bräuer, K., Kämpf, H., Niedermann, S., and Strauch, G. (2013) Indications for the existence of different magmatic reservoirs beneath the Eifel area (Germany):

- a multi-isotope (C, N, He, Ne, Ar) approach. *Chem. Geol.* **356**, 193–208.
- Bräuer, K., Geissler, W. H., Kämpf, H., Niedermann, S., and Rman, N. (2016). Helium and carbon isotope signatures of gas exhalations in the westernmost part of the Pannonian Basin (SE Austria/NE Slovenia): Evidence for active lithospheric mantle degassing. *Chem. Geol.* **422**, 60-70.
- Buck, W.R. (2004) Consequences of asthenospheric variability on continental rifting. In: Karner, G.D., Taylor, B., Driscoll, N.W., Kohlstedt, D.L. (Eds.), *Rheology and Deformation of the Lithosphere at Continental Margins*. Columbia University Press, New York, pp. 1–31.
- Burton, M. R., Sawyer, G. M., and Granieri, D. (2013) Deep carbon emissions from volcanoes. *Rev. Mineral. Geochem.* **75**, 323-354.
- Calais, E., d'Oreye, N., Albaric, J., Deschamps, A., Delvaux, D., Déverchère, J., Ebinger, C., Ferdinand, R.W., Kervyn, F., Macheyeke, A.S., Oyen, A., Perrot, J., Saria, E., Smets, B., Stamps, D.S., and Wauthier, C. (2008) Strain accommodation by slow slip and dyking in a youthful continental rift, East Africa. *Nature* **456**, 783-787.
- Capaccioni, B., Franco, T., Alberto, R., Orlando, V., Marco, M., and Salvatore, I. (2014) Geo-chemistry of thermal fluids in NW Honduras: new perspectives for exploration of geothermal areas in the southern Sula graben. *J. Volcanol. Geotherm. Res.* **280**, 40–52.
- Caracausi, A., and Paternoster, M. (2015) Radiogenic helium degassing and rock fracturing: A case study of the southern Apennines active tectonic region. *J. Geophys. Res.* **120**, 2200-2211.

- Cartigny P. (2005) Stable isotopes and the origin of diamond. *Elements* **1**, 79–84.
- Chiodini, G. and Marini, L. (1998) Hydrothermal gas equilibria: the H₂O–H₂–CO₂–CO–CH₄ system. *Geochim. Cosmochim. Acta* **62**, 2673–2687.
- Clor, L. E., Fischer, T. P., Hilton, D. R., Sharp, Z. D., and Hartono, U. (2005) Volatile and N isotope chemistry of the Molucca Sea collision zone: tracing source components along the Sangihe Arc, Indonesia. *Geochem. Geophys. Geosyst.* **6**, Q03J14.
- Corti, G. (2009) Continental rift evolution: from rift initiation to incipient break-up in the Main Ethiopian Rift, East Africa. *Earth Sci. Rev.* **96**, 1–53.
- Craig, H., Clarke, W., and Beg, M. (1975) Excess ³He in deep water on the East Pacific Rise. *Earth Planet. Sci. Lett.* **26**, 125–132.
- Crane, K. (1981) Thermal variations in the Gregory Rift of southern Kenya (?). *Tectonophysics* **74**, 239-262.
- Crane, K. and O’Connell, S. (1983) The distribution and implications of heat flow from the Gregory Rift in Kenya. *Tectonophysics* **94**, 253-275.
- Crossey, L., Karlstrom, K., Springer, A., Newell, D., Hilton, D. R., and Fischer, T. (2009) Degassing of mantle-derived CO₂ and He from springs in the southern Colorado Plateau region-Neotectonic connections and implications for groundwater systems. *Geol. Soc. Am. Bull.* **121**, 1034-1053.
- Crossley, R. (1979) The Cenozoic stratigraphy and structure of the western part of the rift valley in southern Kenya. *J. Geol. Soc. London* **136**, 393-405.
- Danabalan, D., Gluya, J. G., Macpherson, C. G., Abraham-James, T. H., Bluett, J. J., Barry, P. H., and Ballentine, C. J. (2016) New high-grade helium discoveries in

Tanzania. *Goldschmidt conference abstracts*, **595**.

Daniels, K. A., Bastow, I. D., Keir, D., Sparks, R. S. J., and Menand, T. (2014) Thermal models of dyke intrusion during development of continent-ocean transition. *Earth Planet. Sci. Lett.* **145-153**, doi: 10.1016/j.epsl.2013.09.018.

Darling, W. G., Greisshaber, E., Andrews, J. N., Armannsson, H., and O'Nions, R. K. (1995) The origin of hydrothermal and other gases in the Kenya Rift Valley. *Geochim. Cosmochim. Acta* **59**, 2501-2512.

Darrah, T. H., Tedesco, D., Tassi F., Vaselli, O., Cuoco, E., and Poreda, R. J. (2013) Gas chemistry of the Dallol region of the Danakil depression in the Afar region of the northern-most East African Rift. *Chem. Geol.* **339**, 16-29.

de Moor, J.M., Fischer, T.P., Sharp, Z.D., Mangasini, F., Ramirez, C., Hilton, D.R., and Barry, P. (2013) Cold mantle gases from Rungwe Volcanic Province, southern Tanzania. *Chem. Geol.* **339**, 30-42.

Dunai, T. J. and Porcelli, D. (2002) Storage and transport of noble gases in the subcontinental lithosphere. *Rev. Mineral. Geochem.* **47**, 371–409.

Ebinger, C. J. (1989) Tectonic development of the western branch of the East African rift system. *Geol. Soc. Am. Bull.* **101**, 885–903.

Ebinger, C. J. (2005) Continental break-up: the East African perspective. *Astron. Geophys.* **46**, 2.16-2.21.

Ebinger, C. and Scholz, C.A. (2012) Continental rift basins: the East African perspective. In: Azor Pérez, A., Busby, C. (Eds.), *Tectonics of sedimentary basins*. Blackwell Publishing Ltd., pp. 185–208.

Ebinger, C., Bechtel, T., Forsyth, D., and Bowin, C. (1989) Effective elastic plate thickness

- beneath the East African and Afar plateaus and dynamic compensation of the uplifts. *J. Geophys. Res.* **94**, 2883-2901.
- Ebinger, C., Djomani, Y., Mbede, Y., Foster, F., and Dawson, J. (1997) Rifting Archean lithosphere: the Eyasi–Manyara–Natron rifts, East Africa. *Journal of the Geological Society of London* **154**, 947-960.
- Ebinger, C.J., Yemane, T., Hardling, D.J., Tesfaye, S., Kelley, S., and Rex, D.C. (2000) Rift deflection, migration, and propagation: Linkage of the Ethiopian and Eastern rifts, Africa. *Geological Society America Bulletin* **112** (2), 163–176.
- Elkins, L., Fischer, T.P., Hilton, D.R., Sharp, Z.D., McKnight, S., and Walker, J.A. (2006) Tracing nitrogen in volcanic and geothermal volatiles from the Nicaraguan volcanic front. *Geochim. Cosmochim. Acta* **70**, 5215–5235.
- Eugster, H. P. (1970) Chemistry and origin of the brines of Lake Magadi, Kenya. *Mineral. Soc. Amer. Spec. Paper* No. 3. 215-235.
- Fischer, T.P. (2008) Volatile fluxes (H₂O, CO₂, N₂, HCl, HF) from arc volcanoes. *Geochem. J.* **42**, 21–38.
- Fischer, T. P. and Chiodini, G. (2015) Volcanic, magmatic, and hydrothermal gases. In: Sigurdsson, H., Houghton, B., McNutt, S., Rymer, H., Stix, J. (Eds.), *Encyclopedia of Volcanoes*, Academic Press, London, pp. 779-797.
- Fischer, T., Burnard, P., Marty, Palhol, F., Magasini, F., and Shaw, A.M. (2006) The 2005 and 2006 eruptions of Ol Doinyo Lengai: assessing deep and shallow processes at an active carbonatite volcano using volatile chemistry and fluxes. *Eos Transactions. American Geophysical Union* **87** (52). Fall Meeting Supplement: Abstract V14B-04.

- Fischer, T.P., Hilton, D.R., Zimmer, M.M., Shaw, A.M., Sharp, Z.D., and Walker, J.A. (2002) Subduction and recycling of nitrogen along the Central American margin. *Science* **297**, 1154-1157.
- Fischer, T. P., Burnard, P., Marty, B., Hilton, D. R., Furi, E., Palhol, F., Sharp, Z. D., and Mangasini, F. (2009) Upper-mantle volatile chemistry at Oldoinyo Lengai volcano and the origin of carbonatites. *Nature* **459**, 77-80.
- Foster, A., Ebinger, C., Mbede, E., and Rex, D. (1997) Tectonic development of the northern Tanzanian sector of the east African rift system. *J. Geol. Soc.* **154**, 689-700.
- Gautheron, C. and Moreira, M. (2002) Helium signature of the subcontinental lithospheric mantle. *Earth Planet. Sci. Lett.* **199**, 39-47.
- George, R., Rogers, N., and Kelley, S. (1998) Earliest magmatism in Ethiopia: evidence for two mantle plumes in one flood basalt province. *Geology* **26**, 923-926.
- Giggenbach, W.F. (1980) Geothermal gas equilibria. *Geochim. Cosmochim. Acta* **44**, 2021–2032.
- Giggenbach, W.F. (1987) Redox processes governing the chemistry of fumarolic gas discharges from White Island, New Zealand. *Appl. Geochem.* **2**, 143–161.
- Giggenbach, W.F. and Goguel, R.L. (1989) Methods for the collection and analysis of geothermal and volcanic water and gas samples. CD 2387, *Department of Scientific and Industrial Research, Chemistry Division*.
- Giggenbach, W.F. and Poreda, R.J. (1993) Helium isotopic and chemical composition of gases from volcanic-hydrothermal systems in the Philippines. *Geothermics* **22**, 369-380.

- Gilfillan, S.M.V., Lollar, B.S., Holland, G., Blagburn, D., Stevens, S., Schoell, M., Cassidy, M., Ding, Z., Zhou, Z., Lacrampe-Couloume, G., and Ballentine, C.J. (2009) Solubility trapping in formation water as dominant CO₂ sink in natural gas fields. *Nature* **458**, 614-618.
- Goff, F. and Janik, C.J. (2000) Geothermal Systems. In: Sigurdsson, H., Houghton, B., McNutt, S., Rymer, H., Stix, J. (Eds.), *Encyclopedia of Volcanoes*. Academic Press, San Diego, CA, pp. 817-834.
- Goff, F. and Janik, C.J. (2002) Gas geochemistry of the Valles caldera region, New Mexico and comparisons with gases at Yellowstone, Long Valley and other geothermal systems. *J. Volcanol. Geotherm. Res.* **116**, 299–323.
- Graham, D.W. (2002) Noble gas isotope geochemistry of mid-ocean ridge and ocean island basalts: characterization of mantle source reservoirs. *Rev. Mineral. Geochem.* **47**, 247-317.
- Halldórsson, S.A., Hilton, D.R., Scarsi, P., Adebé, T., and Hopp, J. (2014) A common mantle plume source beneath the entire East African Rift system revealed by coupled helium–neon systematics. *Geophys. Res. Lett.* **41**, 2304-2311.
- Hilton, D., Halldórsson, S., Barry, P., Fischer, T., de Moor, J., Ramirez, C., Mangasini, F., and Scarsi, P. (2011) Helium isotopes at Rungwe Volcanic Province, Tanzania, and the origin of East African Plateaux. *Geophys. Res. Lett.* **38**, L21304.
- Hochstein, M.P., Temu, E.P., and Moshy, C.M.A. (2000) Geothermal resources of Tanzania. In: *Proceedings of the World Geothermal Congress*, Kyushu-Tohoku, Japan, May 28–June 10, pp. 1233-1238.
- Hopp, J., Trieloff, M., and Altherr, R. (2007) Noble gas compositions of the lithospheric

- mantle below the Chyulu Hills volcanic field, Kenya. *Earth Planet. Sci. Lett.* **261**, 635-648.
- Ibs-von Seht, M., Blumenstein, S., Wagner, R., Hollnack, D., and Wohlenberg, J. (2001) Seismicity, seismotectonics and crustal structure of the southern Kenya Rift—new data from the Lake Magadi area. *Geophys. J. Int.* **146**, 439-453.
- Jones, B. F., Eugster, H. P. and Rettig, S. L. (1977) Hydrochemistry of the Lake Magadi basin, Kenya. *Geochim. Cosmochim. Acta* **44**, 53-72.
- Kagoshima, T., Sano, Y., Takahata, N., Maruoka, T., Fischer, T.P., and Hattori, K. (2015) Sulphur geodynamic cycle. *Sci. Reports* **5**, 8330.
- Kampunzu, A.B., Bonhomme, M.G., and Kanika, M. (1998) Geochronology of volcanic rocks and evolution of the Cenozoic Western branch of the East African rift system. *J. Afr. Earth Sci.* **26**, 441-446.
- Kennedy, B. M., Kharaka, Y. K., Evans, W. C., Ellwood, A., DePaolo, D. J., Thordsen, J. J., Ambats, G., and Mariner, R. H. (1997) Mantle fluids in the San Andreas fault system, California. *Science* **278**, 1278-1281.
- Kennedy, B. M. and Van Soest, M. C. (2007) Flow of mantle fluids through the ductile lower crust: helium isotope trends. *Science* **318**, 1433-1436.
- Kipfer, R., Aeschbach-Hertig, W., Peeters, F., and Stute, M. (2002) Noble gases in lakes and ground waters. *Rev. Mineral. Geochem.* **47**, 615-700.
- Lee, H., Sharp, Z. D., and Fischer, T. P. (2015) Kinetic nitrogen isotope fractionation between air and dissolved N₂ in water: Implications for hydrothermal systems. *Geochem. J.* **49**, 571-573.
- Lee, H., Muirhead, J. D., Fischer, T. P., Ebinger, C. J., Kattenhorm, S. A., Sharp, Z. D.,

- and Kianji, G. (2016) Massive and prolonged deep carbon emissions associated with continental rifting. *Nat. Geosci.* **9**, 145-149.
- Le Gall, B., Nonnotte, P., Rolet, J., Benoit, M., Guillou, H., Mousseau-Nonnotte, M., Albaric, J., and Déverchère, J. (2008) Rift propagation at craton margin: distribution of faulting and volcanism in the North Tanzanian Divergence (East Africa) during Neogene times. *Tectonophysics* **448** (1–4), 1–19. doi:10.1016/j.tecto.2007.11.005.
- Levin N. E., Zipser E. J. and Cerling T. E. (2009) Isotopic composition of waters from Ethiopia and Kenya: insights into moisture sources for eastern Africa. *J. Geophys. Res.* **114**, D23306. doi:10.1029/2009JD012166.
- Lindenfeld, M., Rumpker, G., Link, K., Koehn, D., Batte, A. (2012) Fluid-triggered earthquake swarms in the Rwenzori region, East African Rift—evidence for rift initiation. *Tectonophysics* **566–567**, 95–104.
- Lowenstern, J., Evans, W., Bergfeld, D., Hunt, A. (2014) Prodigious degassing of a billion years of accumulated radiogenic helium at Yellowstone. *Nature* **506**, 355–358.
- Mana, S., Furman, T., Turrin, B.D., Feigenson, M.D., and Swisher III, C.C. (2015) Magmatic activity across the East African North Tanzanian Divergence Zone, *J. Geol. Soc.* **172**, 368–389.
- Mangler, M.F., Marks, M.A.W., Zaitzev, A.N., Eby, G.N., and Markl, G. (2014) Halogen (F, Cl, and Br) at Oldoinyo Lengai volcano (Tanzania): effects of magmatic differentiation, silicate- natrocarbonatite melt separation and surface alteration of natrocarbonatite. *Chem. Geol.* **365**, 43–53.

- Marty, B. (1995) Nitrogen content of the mantle inferred from N₂-Ar correlation in oceanic basalts. *Nature* **377**, 326-329.
- Marty, B. and Jambon, A. (1987) C³He in volatile fluxes from the solid earth – implications for carbon geodynamics. *Earth Planet. Sci. Lett.* **83**, 16-26.
- Marty, B. and Humbert, F. (1997) Nitrogen and argon isotopes in oceanic basalts. *Earth Planet. Sci. Lett.* **152**, 101–112.
- Marty, B. and Tolstikhin, I. N. (1998) CO₂ fluxes from mid-ocean ridges, arc and plumes. *Chem. Geol.* **145**, 233-248.
- Marty, B. and Zimmermann, L. (1999) Volatiles (He, C, N, Ar) in mid-ocean ridge basalts: assessment of shallow-level fractionation and characterization of source composition. *Geochim. Cosmochim. Acta* **63**, 3619-3633.
- Marty, B., Pik, R., and Gezahegn, Y. (1996) Helium isotopic variations in Ethiopian plume lavas: nature of magmatic sources and limit on lower mantle contribution. *Earth Planet. Sci. Lett.* **144**, 223–237.
- Mohapatra, R.K. and Murty, S.V.S. (2004) Nitrogen isotopic composition of the MORB mantle: a reevaluation. *Geochem. Geophys. Geosys.* **5**. doi:10.1029/2003GC000612.
- Moreira, M., Kunz, J., and Allegre, C.J. (1998) Rare gas systematics in popping rock: isotopic and elemental compositions in the upper mantle. *Science* **279**, 1178–1181.
- Muirhead, J. D., Kattenhorn, S. A., and Le Corvec, N. (2015) Varying styles of magmatic strain accommodation across the East African Rift. *Geochem. Geophys. Geosyst.* **6** (8), 2775-2795.

- Muirhead, J. D., Kattenhorn, S. A., Lee, H., Mana, S., Turrin, B. D., Fischer, T. P., Kianji, G., Dindi, E., and Stamps, D. S. (2016) Evolution of faulting and magmatic volatile systems during early-stage continental rift development in the East African Rift. *Geosphere* **12** (6), 1670-1700.
- Newell, D. L., Jessup, M. J., Cottle, J. M., Hilton, D. R., Sharp, Z. D., and Fischer, T. P., (2008) Aqueous and isotope geochemistry of mineral springs along the southern margin of the Tibetan Plateau: implications for fluid sources and regional degassing of CO₂. *Geochem. Geophys. Geosyst.* **9**, Q08014, <http://dx.doi.org/10.1029/2008GC002021>.
- Nyblade, A.A. and Brazier, R.A. (2002) Precambrian lithospheric controls on the development of the East African Rift System. *Geology* **30**, 755-758.
- O’Nions, R. K. and Oxburgh, E. R. (1988) Helium, volatile fluxes and the development of the continental crust. *Earth Planet. Sci. Lett.* **90**, 331-347.
- Ozima, M. and Podosek, F.A. (1983) Noble Gas Geochemistry. *Cambridge University Press*, Cambridge, p. 367.
- Pasteels, P., Villeneuve, M., De Paepe, P., and Klerkx, J. (1989) Timing of the volcanism of the southern Kivu province: implications for the evolution of the western branch of the East African Rift system. *Earth Planet. Sci. Lett.* **94**, 353-363.
- Reyners, M., Eberhart-Phillips, D., and Stuart, G. (2007) The role of fluids in lower-crustal earthquakes near continental rifts. *Nature* **446**, 1075–1078.
- Roberts, E.M., Stevens, N.J., O’Connor, P.M., Dirks, P.H. G.M., Gottfried, M.D., Clyde, W.C., Armstrong, R.A., Kemp, A.I.S., and Hemming, S. (2012) Initiation of the western branch of the East African Rift coeval with the eastern branch.

Nat. Geosci. **5**, 289-294.

- Robertson, E., Biggs, J., Edmonds, M., Clor, L., Fischer, T. P., Vye-Brown, C., Kianji, G., Koros, W., and Kandie, R. (2016) Diffuse degassing at Longonot volcano, Kenya: Implications for CO₂ flux in continental rifts. *J. Volcanol. Geotherm. Res.* **327**, 208-222.
- Ryan, W. B. F., Carbotte, S. M., Coplan, J. O., O'Hara, S., Melkonian, A., Arko, R., Weisell, R. A., Ferrini, V., Goodwillie, A., Nitsche, F., Bonczkowski, J., and Zemsky, R. (2009) Global multi-resolution topography synthesis. *Geochem. Geophys. Geosyst.* **10**. <http://dx.doi.org/10.1029/2008GC002332>.
- Sano, Y. and Wakita, H. (1985) Geographical distribution of ³He/⁴He ratios in Japan: implications for arc tectonics and incipient magmatism. *J. Geophys. Res.* **90** (B10), 8729–8741.
- Sano, Y. and Marty, B. (1995) Origin of carbon in fumarolic gas from island arcs. *Chem. Geol.* **119**, 265-274.
- Sano, Y. and Fischer, T. P. (2013) The analysis and Interpretation of Noble Gases in Modern Hydrothermal Systems. In P. Burnard (ed.), *The Noble Gases as Geochemical Tracers, Advances in Isotope Geochemistry*. DOI: 10.1007/978-3-642-28836-4-2, pp. 249-317, Springer-Verlag, Berlin.
- Sano, Y., Takahata, N., and Seno, T. (2006) Geographical Distribution of ³He/⁴He Ratios in the Chugoku District. Southwestern Japan. *Pure Appl. Geophys.* **163**, 745-757.
- Sano, Y., Tokutake, T., and Takahata, N. (2008) Accurate measurement of atmospheric

helium isotopes. *Anal. Sci.* **24**, 521-525.

Sano, Y., Takahata, N., Nishio, Y., and Marty, B. (1998) Nitrogen recycling in subduction zones. *Geophys. Res. Lett.* **25**, 2289-2292.

Sano, Y., Takahata, N., Nishio, Y., Fischer, T., and Williams, S. (2001) Volcanic flux of nitrogen from the Earth. *Chem. Geol.* **171**, 263-271.

Sawyer, G. M., Carn, S. A., Tsanev, V., Oppenheimer, C., and Burton, M. (2008) Investigation into magma degassing at Nyiragongo volcano, Democratic Republic of the Congo. *Geochem. Geophys. Geosyst.* **9**, Q02017, doi:10.1029/2007GC001829.

Sawyer, G. M., Oppenheimer, C., Tsanev, V. I., and Yirgu, G. (2008) Magmatic degassing at Erta 'Ale volcano, Ethiopia. *J. Volcanol. Geotherm. Res.* **178**, 837-846.

Sherwood-Lollar, B. and Ballentine, C.J. (2009) Insights into deep carbon derived from noble gases. *Nat. Geosci.* **2**, 543-547.

Tassi, F., Aguilera, F., Darrah, T., Vaselli, O., Capaccioni, B., Poreda, R.J., Delgado and Huertas, A. (2010) Fluid geochemistry of hydrothermal systems in the Arica–Parinacota, Tarapacá and Antofagasta Regions (Northern Chile). *J. Volcanol. Geotherm. Res.* **192**, 1–15.

Tedesco, D., Tassi, F., Vaselli, O., Poreda, R. J., Darrah, T., Cuoco, E., and Yalire, M. M. (2010) Gas isotopic signatures (He, C, and Ar) in the Lake Kivu region (western branch of the East African rift system): geodynamic and volcanological implications. *J. Geophys. Res —Solid Earth.*

Torgersen, T. (2010) Continental degassing flux of ⁴He and its variability. *Geochem. Geophys. Geosyst.* **11**. Q06002, doi:10.1029/2009GC002930.

- Truesdell, A.H. and Hulston, J.R. (1980) Isotopic evidence on environments of geothermal systems. In: Fritz, P. and J. Ch. Fontes (Ed.), *Handbook of Environmental Isotopes Geochemistry. The Terrestrial Environment A 1*. Elsevier, Amsterdam, 179–226.
- Weinlich, F. H., Bräuer, K., Kämpf, H., Strauch, G., Tesar, J., and Weise, S. M. (1999) An active subcontinental mantle volatile system in the western Eger rift, Central Europe: gas flux, isotopic (He, C, and N) and compositional fingerprints. *Geochim. Cosmochim. Acta* 63, 3653–3671.
- Weinstein, A., Ebinger, C. J., Oliva, S. J., Roecker, S., Tiberi, C., Lambert, C., Witkin, E., Albaric, J., Gautier, S., Muzuka, A., Mulibo, G., Hadfield, R., Illsley-Kemp, F., Msabi, M., Ferdinand-Wambura, R., Peyrat, S, Muirhead, J., Rodzianko, A., and Fischer, T. P. Magmatic CO₂ –assisted rifting in East Africa: Seismicity of the Magadi-Natron-Manyara basins, Africa (submitted).
- Zhang, J., Quay, P.D., and Wilbur, D.O. (1995) Carbon isotope fractionation during gas–water exchange and dissolution of CO₂. *Geochim. Cosmochim. Acta* 59, 107–114.
- Zhou, Z., Ballentine, C.J., Schoell, M., and Stevens, S.H. (2012) Identifying and quantifying natural CO₂ sequestration processes over geological timescales: the Jackson Dome CO₂ Deposit, USA. *Geochim. Cosmochim. Acta* 86, 257–275.
- Zimmer, M. M., Fischer, T. P., Hilton, D. R., Alvarado, G. E., Sharp, Z. D., and Walker, J. A. (2004) Nitrogen systematics and gas fluxes of subduction zones: Insights from Costa Rica arc volatiles. *Geochem. Geophys. Geosyst.* 5, Q05J11,

doi:10.1029/2003GC000651.

CHAPTER 4

NITROGEN RECYCLING AT THE COSTA RICAN SUBDUCTION ZONE: THE ROLE OF INCOMING PLATE STRUCTURE

Manuscript in preparation collaborating with Fischer, T.P., de Moor, J.M., Sharp, Z.D., Takahata, N., and Sano, Y.

1. ABSTRACT

Efficient recycling of subducted sedimentary nitrogen back to the atmosphere through arc volcanism has been advocated for the Central America margin (Fischer et al., 2002) while at other locations mass balance considerations (Mitchell et al., 2010) and nitrogen contents of high pressure metamorphic rocks (Busigny et al., 2003) imply massive addition of subducted nitrogen to the mantle and past the zones of arc magma generation. The difference in the recycling efficiency of subducted nitrogen, with its implications of the deep nitrogen cycle, has been attributed to slab temperature variations (Busigny et al., 2003) and recently to variations in fluid oxidation states (Mikhail et al., 2017). Here, we report new results of nitrogen isotope compositions with gas chemistry and noble gases of forearc and arc front springs in Costa Rica to show that the structure of the incoming plate has a profound effect on the extent of nitrogen subduction into the mantle. In the Costa Rican subduction zone at 9-11N°, nitrogen isotope compositions of emitted arc gases imply less subducted pelagic sediment contribution compared to further north (Fischer et al., 2002; Zimmer et al., 2004; Elkins et al., 2006). The nitrogen isotope compositions ($\delta^{15}\text{N} =$

-4.4 to 1.6‰) of forearc springs at 9-11N° are consistent with these previously reported values in volcanic centers ($\delta^{15}\text{N} = -3.0$ to 1.9‰: Fischer et al., 2002; Zimmer et al., 2004; Fischer et al., 2015). The Nicoya and Santa Elena forearc springs in particular have similar nitrogen compositions as altered subducted oceanic plates. We advocate that subduction erosion enhanced by abundant seamount subduction at 9-11N° introduces overlying forearc crustal materials into the Costa Rican subduction zone, diluting slab sediment-derived nitrogen isotope signatures. This process supporting the deep recycling of N into the deep mantle in this section of the Central American margin.

2. INTRODUCTION

Subduction-zone fluids play a pivotal role in magma generation processes in arc settings. The release of fluids and volatiles from subducting slabs causes melting of the overlying mantle to produce arc magmas (Tatsumi et al., 1983; Arculus, 1994). Mass balance relationships of geochemical processes have been used to understand subduction processes, recycling of chemical components, mantle heterogeneity, and climate effects (Fischer et al., 2002; Hilton et al., 2002). The Central American margin extending from the Mexico/Guatemala border to northern Panama is considered an appropriated area to test geochemical mass balance relationships because numerous studies have constrained geophysical and geochemical parameters. The Costa Rican subduction zone that is associated with the Caribbean plate subducted by the Cocos plate and the Cocos ridge (Fig. 1) has been favored by geochemical studies of carbon and nitrogen recycling mechanisms because of geochemical accessibilities to drilled oceanic samples, forearc fluid seeps, and volcanism on the arc front (Fischer et al., 2002; Shaw et al., 2003; Zimmer et al., 2004; Li

and Bebout, 2005; Fűri et al., 2010). Nitrogen (N), the most abundant gas component in air, is one of major volatiles released by volcanism and hydrothermal activity to the atmosphere (Rubey, 1951). In subduction systems, N in magmatic volatiles reflects pelagic sediment input ($\delta^{15}\text{N} = 7\text{‰}$, Sano et al., 2001) that is subducted with oceanic plates (Fischer et al., 2002; Elkins et al., 2006; Agosto et al., 2013; Tardani et al., 2016). In the Central American margin, previously reported N isotope compositions of fumarole and hot spring gas discharges in Guatemala and Nicaragua show such a sediment contribution with $\delta^{15}\text{N}$ values $< 6.3\text{‰}$ (Fischer et al., 2002; Elkins et al., 2006). However, $\delta^{15}\text{N}$ values of fumarole and hot spring gas samples in Costa Rica have been reported with a range from -3.0 to 1.7‰, indicating less sediment contribution compared to localities further north (Fischer et al., 2002; Zimmer et al., 2004). Recycling efficiency of N in the Costa Rican subduction zone is low due to the small N outflux at the arc front compared to the N influx at the trench (Zimmer et al., 2004). This observation has been attributed to off-scraping of sediments or forearc devolatilization of N recycling at the Costa Rica subduction zone (Zimmer et al., 2004). In other regions, a low efficiency of N recycling has been documented in the Sangihe Arc (Clor et al., 2005) and in the Mariana Arc (Mitchell et al., 2010). In these locations, sediment off-scraping or lack of organic sediment availability have been invoked as plausible causes for the comparatively low sedimentary N flux out of these volcanic arcs. In order to further constrain the notion of sediment off-scraping or underplating, trenchward regions, such as the forearc, are potential locations where such processes may be observed geochemically. In these areas, devolatilization of pelagic sediments could occur and potentially be sampled in associated springs and groundwaters. However, to date,

N isotope compositions of forearc regions have not been constrained rendering it impossible to investigate its ultimate sources. Costa Rica is the ideal location to perform such a study because the forearc areas are accessible to sampling at Santa Elena, Nicoya, Osa, and Burica peninsulas (Fig. 1), where a number of springs are releasing volatiles. In this work, we report new results of N isotope compositions, gas chemistry, and helium isotopes of springs in the Costa Rican forearc. We also report new data from springs in the Costa Rica arc front.

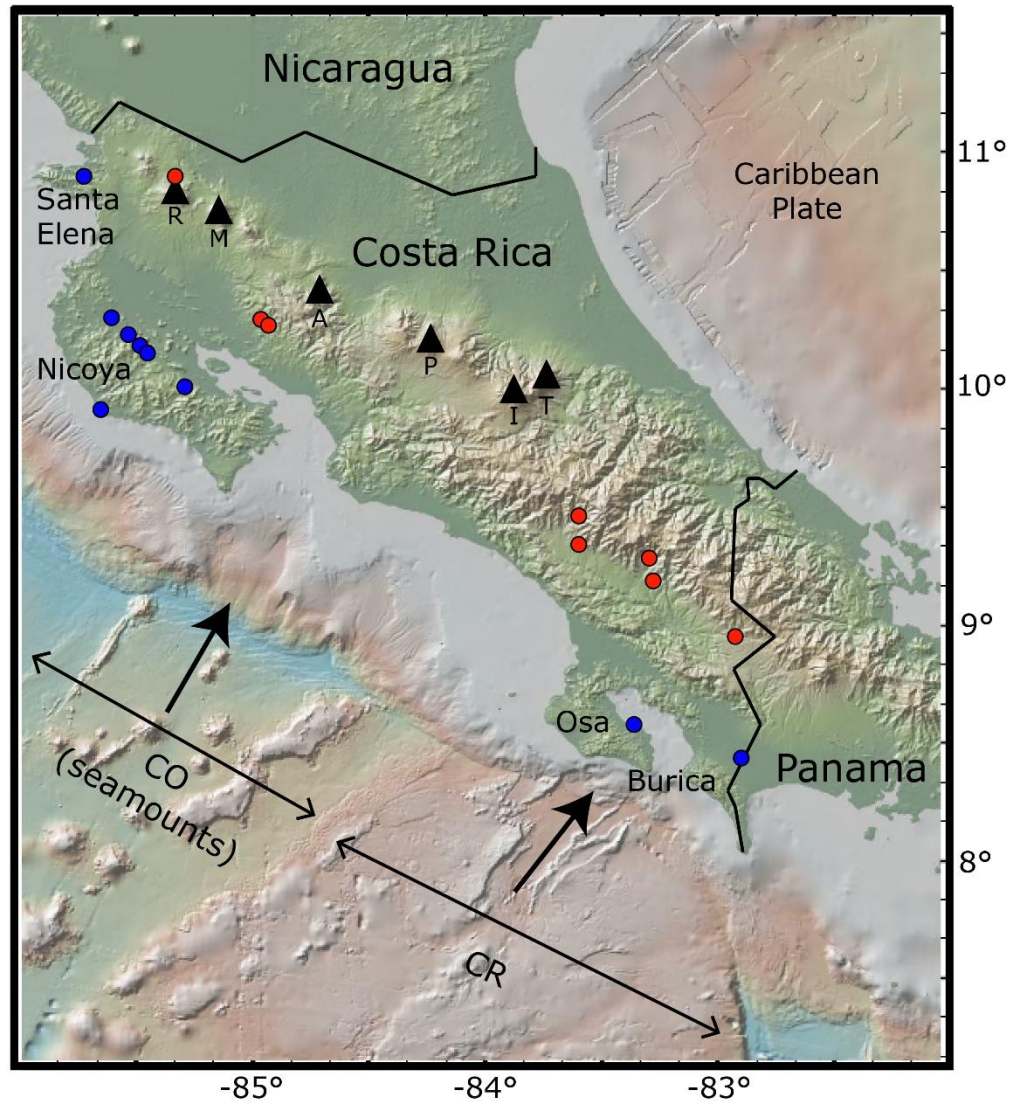


Figure 1. Map of the Costa Rican subduction zone. Sampled forearc (blue circles) and arc front (red circles) springs are shown. This map was created using GeoMapApp (Ryan et al., 2009). Volcanic centers (black triangles) are displayed: R (Rincon de la Vieja), M (Miravalles), A (Arenal), P (Poas), I (Irazu), T (Turrialba). The Cocos plate (CO) with seamounts and the Cocos Ridge (CR) are two major segments in the Costa Rican subduction zone. The subducting plate with seamounts and related scars at the frontal arc are shown at 9-11N°

3. EXPERIMENTAL METHODS

The Costa Rican forearc (Nicoya, Santa Elena, Osa, and Burica) and arc front springs were sampled in 2012 and 2014 (Table 1). Spring samples were collected and stored in pre-evacuated Giggenbach bottles, leaving headspaces for gas analyses. Concentrations of gas components (e.g., N₂, Ar, He, and so on) were obtained in the Volatiles Laboratory at the University of New Mexico (UNM), and the general procedures are described in Giggenbach and Goguel (1989). He, Ar, O₂, and N₂ were also measured in dynamic mode on a Pfeiffer Quadrupole Mass Spectrometer (QMS, analytical errors < 1%) with a mass range from 0 to 120 amu and a secondary electron multiplier detector. CO₂, CH₄, H₂, Ar+O₂, N₂, and CO contents were determined using a Hayes Sep pre-column and 5Å molecular sieve columns on a Gow-Mac series G-M 816 Gas Chromatograph (GC, analytical errors < 2%) with a helium carrier gas. A discharge ionization detector was used for CO₂, CH₄, H₂, Ar+O₂, N₂ and CO, respectively. Concentrations of all gas components were acquired after merging the data from QMS and GC (whole results in Supplementary Information).

Determination of N isotope compositions was conducted using splits of gas samples taken into glass tubes and sealed on high vacuum lines. We neglected the mass interference by carbon monoxide based on its low concentrations (Supplementary Information). Then, N isotope compositions were analyzed on a Thermo Delta V Plus isotope ratio mass spectrometer (IRMS) with a gas bench in the center for Stable Isotopes at UNM. A tube-breaker and a six-way valve were used to break sealed glass tubes and inject N into the IRMS as describe in de Moor et al. (2013). Experimental errors ($1\sigma = 0.1\text{‰}$) for $\delta^{15}\text{N}$ were obtained using multiple measurement of air samples ($\delta^{15}\text{N} = 0\text{‰}$). Argon isotope ratios

($^{40}\text{Ar}/^{36}\text{Ar}$) were determined in static mode on QMS after purification using a cold trap (at liquid N temperature) and hot titanium getters (at 550°C) at UNM. Cu tubes were used for helium isotope analyses because helium can penetrate the glass containers (e.g., Giggenbach bottle). $^3\text{He}/^4\text{He}$ ratios were acquired by a Helix-SFT noble gas mass spectrometer at the Atmosphere and Ocean Research Institute of the University of Tokyo (AORI). He and Ne were purified using hot titanium getters (held at 400°C) and charcoal traps (at liquid N temperature) and $^4\text{He}/^{20}\text{Ne}$ ratios were obtained by an on-line QMS. After that, neon was trapped using a cryogenic trap (at 40°K). Experimental errors (1σ) for and $^3\text{He}/^4\text{He}$ and $^4\text{He}/^{20}\text{Ne}$ ratios are about 1% and 5% (Sano et al., 2008).

Table 1. Locations of the sampled Costa Rican springs.

Area	ID	Latitude (N)	Longitude (W)	T	pH	
Forearc springs						
Nicoya	La Conchita Pool	CR14-01	10°18'27.1'	85°36'20.5"	27.8	7.5
	Rancho El Salitral	CR12-16	10°13'55.6"	85°31'53.7"	29.6	10.1
		CR14-02			30.5	10.2
	Sabana Grande	CR12-15	10°10'44.6"	85°28'48.5"	31.5	8.5
		CR14-03			31.6	9.4
	Playa Garza	CR14-06A	09°54'28.5"	85°39'00.9"	29.8	7.0
		CR14-06B				
	Salitral Vigia	CR14-07	10°06'24.6"	85°17'09.8"	26.0	8.1
	Salitral San Martin	CR12-14	10°09'37.4"	85°27'36.2"	29.7	8.5
		CR14-08				
Santa Elena	Rio Murcielago 1	CR14-09	10°53'26.3"	85°43'33.6"	28.6	11.1
		CR14-09B				
Osa	Sandaló	CR12-01	08°34'31.2"	83°21'49.8"	29.5	
		CR12-02				
Burica	Laurel	CR12-03	08°26'28.6"	82°54'17.4"		8.3
		CR12-04				8.1
Arc front springs						
Aguas Calientes	CR12-05	08°56'49.1"	82°55'08.8"	37.2	6.5	
	CR12-06				6.4	
Yheri	CR12-07	09°11'41.4"	83°16'50.9"	26.1	7.7	
	CR12-08				6.7	
Rocas Calientes	CR12-09	09°18'10.4"	83°17'52.4"	62.8	7.4	
	CR12-10				7.8	
Montecarlo	CR12-11	09°20'38.4"	83°35'43.5"	32.3	7.8	
	CR12-12					
Aguas Termales Gevi	CR12-13	09°28'20.0"	83°36'16.7"	36.8	8.1	
Pueblo Antiguo	CR12-18	10° 16' 59.8"	84° 55' 45.3"	45.3	7.8	
Cayuco	CR12-19	10°17'14.9"	84°57'20.3"	72.6	6.5	
Rincon de la Vieja	CR14-11	10°53'51.8"	85°19'35.6"	61.5	6.5	

Table 2. Gas chemistry of N₂-Ar-He and isotope compositions of the Costa Rican springs.

ID	N ₂ /Ar	N ₂ /He	He/Ar	N ₂ ^{exc} /He	δ ¹⁵ N-N ₂	±	R/Ra	±	⁴ He/ ²⁰ Ne
Forearc springs									
CR14-01							1.02	0.01	0.40
CR12-16	47	8,721	0.005	1,297	-0.7	0.1			
CR14-02	58	2,195	0.026	676	-2.1	< 0.1	0.88	0.01	0.49
CR12-15	66	5,998	0.011	2,377	-1.1	< 0.1			
CR14-03	49	4,267	0.011	773	-0.7	< 0.1	0.61	0.01	1.37
CR14-06A	68	3,536	0.019	1,453	-2.8	0.2	0.72	0.01	5.74
CR14-06B	72	2,832	0.025	1,260					
CR14-07	49	2,647	0.019	493	-1.4	< 0.1	0.98	0.01	0.39
CR12-14	75	25,548	0.003	11,865	-0.9	< 0.1			
CR14-08	86		0.036	1,291			0.62	0.01	0.68
CR14-09	46	1,377	0.034	190	0.0	< 0.1	1.06	0.01	0.40
CR14-09B	95	2,230	0.043	1,295			1.09	0.12	1.48
CR12-01	51	5,533	0.009	1,221	4.7	0.1			
CR12-02	73								
CR12-03	62	2,848	0.022	1,022	4.0	1.6			
CR12-04	68	785,392	0.0001	320,225					
Arc front springs									
CR12-05	65	4,463	0.015	1,707	-0.5	0.1			
CR12-06	59	4,980	0.012	1,609	-0.4	0.1			
CR12-07	143	3,728	0.038	2,687	1.6	< 0.1			
CR12-08	116	4,285	0.027	2,808	-0.4	< 0.1			
CR12-09	109	3,450	0.032	2,188	-0.2	0.1			
CR12-10	95	4,211	0.022	2,429	0.8	0.1			
CR12-11	91	3,476	0.026	1,941	-0.4	0.1			
CR12-12	64	3,618	0.018	1,356	0.1	0.3			
CR12-13	30	4,722	0.006		-0.8	0.1			
CR12-18	146	13,554	0.011	9,852.996	1.5	< 0.1			
CR12-19	68	84	0.804	34	-4.4	1.5			
CR14-11	108	1,179	0.092	743	-0.2	< 0.1	7.88	0.18	38.81

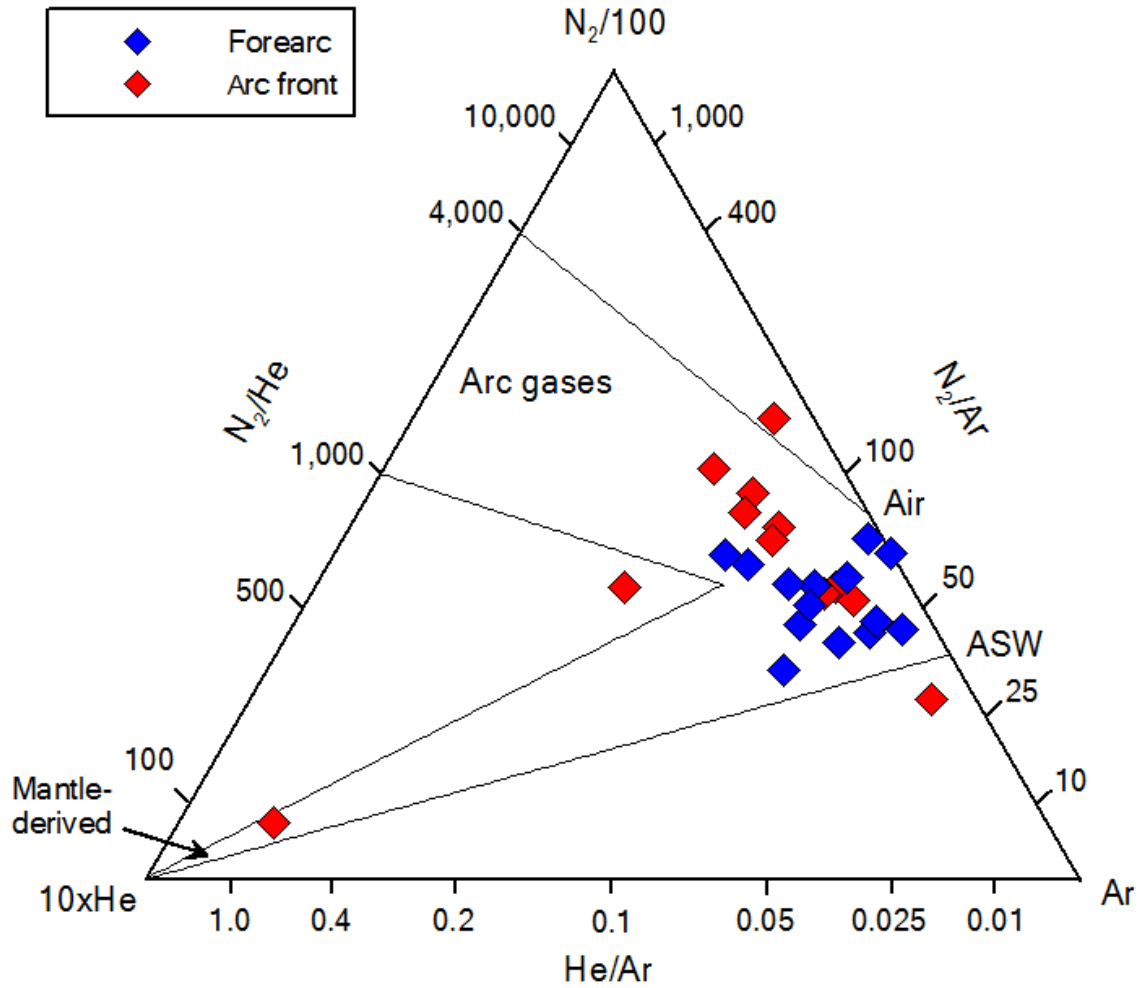


Figure 2. Ternary plot of N_2 -Ar-He abundances. Relative abundances of N_2 , Ar, and He in the forearc and arc front springs samples are used to show mixing relationships among the mantle, arc gases, air, and air saturated water (ASW). The forearc springs plot closer to the air-ASW components than the arc front springs which likely have either the mantle or arc gas end-members.

4. RESULTS

Forearc ($T = 26.0 - 31.6^{\circ}\text{C}$; $\text{pH} = 7.0 - 11.1$) and arc front springs ($T = 26.1 - 72.6^{\circ}\text{C}$; $\text{pH} = 6.5 - 9.6$) in Costa Rica were sampled in 2012 and 2014 (Fig. 1; Table 1). Based on gas compositions, forearc springs are subdivided into N_2 -rich (62.4 – 98.3 vol. %) and CH_4 -rich (36.1 – 96.8 vol. %) types, and arc front springs have N_2 -rich (88.0 – 98.5 vol. %) and CO_2 -rich (47.2 – 98.4 vol. %) types (Table S1). Although air contamination during sampling is minor based on low O_2 contents (< 2.3 vol. %) except for CR12-15, CR14-03, CR14-09B, CR12-05, and CR12-13(6.0-10.3 vol.%) (Table S1), N_2/Ar ratios for forearc (47-95) and arc front (30-146) springs are similar or slightly higher than ratios of air saturated water (ASW, 40) and air (83) (Table 2). N_2/He and He/Ar ratios are higher than 1,000 and lower than 0.1, respectively, except for Cayuco ($\text{N}_2/\text{He} = 84$; $\text{He}/\text{Ar} = 0.8$) which seems to have more mantle-derived volatiles (Table 2). In Fig. 2, the N_2 -Ar-He abundances show that volatiles in the Costa Rican springs are mostly atmospheric, except for two arc front springs (Cayuco and Rincon de la Vieja) with a higher proportion of mantle-derived components. Given that N_2/Ar ratios are higher than ASW, N in excess of ASW ($\text{N}_{2\text{-exc}}$) can be calculated. Ar contents are used to calculate $\text{N}_{2\text{-exc}}$ values based on the assumption that Ar in volcanic gases and geothermal fluids are mostly from ASW (Giggenbach, 1995, Sano and Fischer, 2013). Using measured N_2 and Ar contents and the N_2/Ar ratio of ASW (40), $\text{N}_{2\text{-exc}}$ values are obtained as following (Fischer et al., 1998):

$$\text{N}_{2\text{-exc}} = \text{N}_2 (\text{measured}) - 40 * \text{Ar} (\text{measured}) \quad (1)$$

Calculated $\text{N}_{2\text{-exc}}$ contents and $\text{N}_{2\text{-exc}}/\text{He}$ ratios indicate N amounts in excess to what is supplied to the sampled water phase by N_2 derived from air and then dissolved water (Table 2).

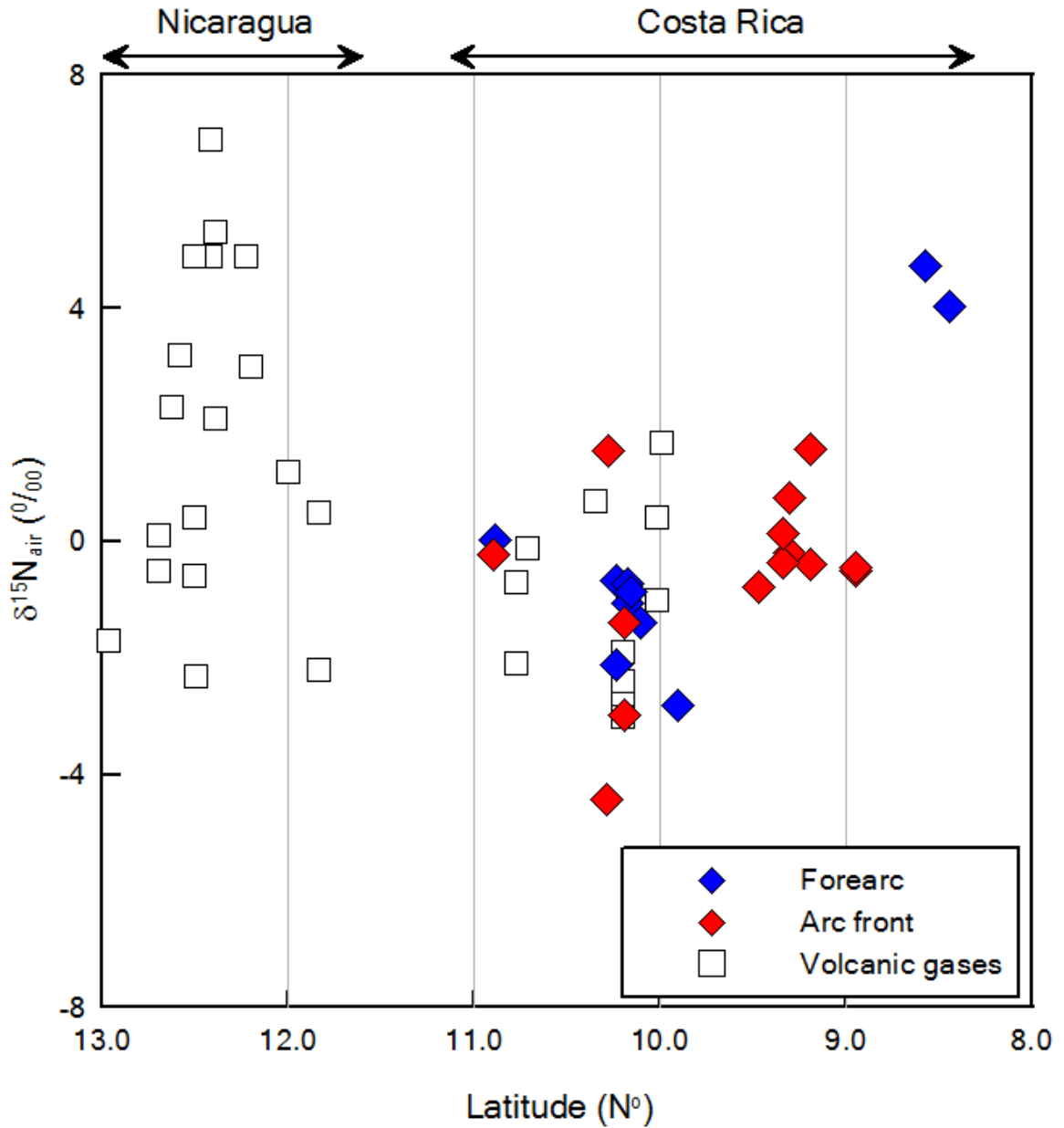


Figure 3. Plot of nitrogen isotope compositions versus latitude. Nitrogen isotope compositions of the Costa Rican forearc and arc front springs are displayed together with previously reported volcanic gases in Costa Rica (Fischer et al., 2002; Zimmer et al., 2004) and Nicaragua (Elkins et al., 2006). Two forearc data points at $< 9^\circ \text{N}$ are the Osa and Burica springs.

Nitrogen isotope compositions ($\delta^{15}\text{N}$ vs air) of the Costa Rican springs range from -4.4 to 1.6‰ (9-11N°), except for the Osa (4.7‰) and Burica (4.0‰) forearc springs located in the southernmost part of Costa Rica (8.4-8.6N°) (Table 2; Fig. 3). The $\delta^{15}\text{N}$ values of the springs are well consistent with the reported volcanic $\delta^{15}\text{N}$ values (-3.0 to 1.9‰, Fischer et al., 2002; Zimmer et al., 2004; Fischer et al., 2015). In Fig. 3, both the forearc and arc front springs at 9-11N° have less sediment ($\delta^{15}\text{N} = 7\%$) contribution than other Central American subduction zone samples ($\delta^{15}\text{N} = -2.2$ to 6.3‰) at > 11N° (e.g., Nicaragua and Guatemala) (Fischer et al., 2002; Elkins et al., 2006). The N sources are constrained following the approach of Sano et al. (2001) and Fischer et al. (2002) by using $\delta^{15}\text{N}$ and N_2/He ratios of the springs (Fig. 4a):

$$\delta^{15}\text{N}_{\text{measured}} = \delta^{15}\text{N}_{\text{MORB}} \times f_{\text{MORB}} + \delta^{15}\text{N}_{\text{sediment}} \times f_{\text{sediment}} + \delta^{15}\text{N}_{\text{air}} \times f_{\text{air}} \quad (2)$$

$$1/(\text{N}_2/\text{He})_{\text{measured}} = f_{\text{MORB}}/(\text{N}_2/\text{He})_{\text{MORB}} + f_{\text{sediment}}/(\text{N}_2/\text{He})_{\text{sediment}} + f_{\text{air}}/(\text{N}_2/\text{He})_{\text{air}} \quad (3)$$

$$f_{\text{MORB}} + f_{\text{sediment}} + f_{\text{air}} = 1 \quad (4)$$

where f_{MORB} , f_{sediment} , and f_{air} are fractions of three end-members (Mid Ocean Ridge Basalt (MORB), sediment, and air). $\delta^{15}\text{N}_{\text{MORB}}$, $\delta^{15}\text{N}_{\text{sediment}}$, and $\delta^{15}\text{N}_{\text{air}}$, are -5‰, 7‰, and 0‰, and $(\text{N}_2/\text{He})_{\text{MORB}}$, $(\text{N}_2/\text{He})_{\text{sediment}}$, and $(\text{N}_2/\text{He})_{\text{air}}$ are 150, 10,500, and 148,900, respectively (Peters et al., 1978; Marty, 1995; Marty and Zimmermann, 1999; Kienast, 2000; Sano et al., 2001; Ozima and Podosek, 2002; Fischer et al., 2002). However, $\delta^{15}\text{N}$ values (-2.8 to -0.7‰) of the Nicoya forearc springs and the arc front springs, which have been reported for the Sangihe and Nicaraguan arc systems (Clor et al., 2005; Elkins et al., 2006), are negatively shifted from the MOBR-air mixing lines (Fig. 4a). In order to account for this shift, kinetic fractionation processes related to gas bubbling through spring water (Lee et

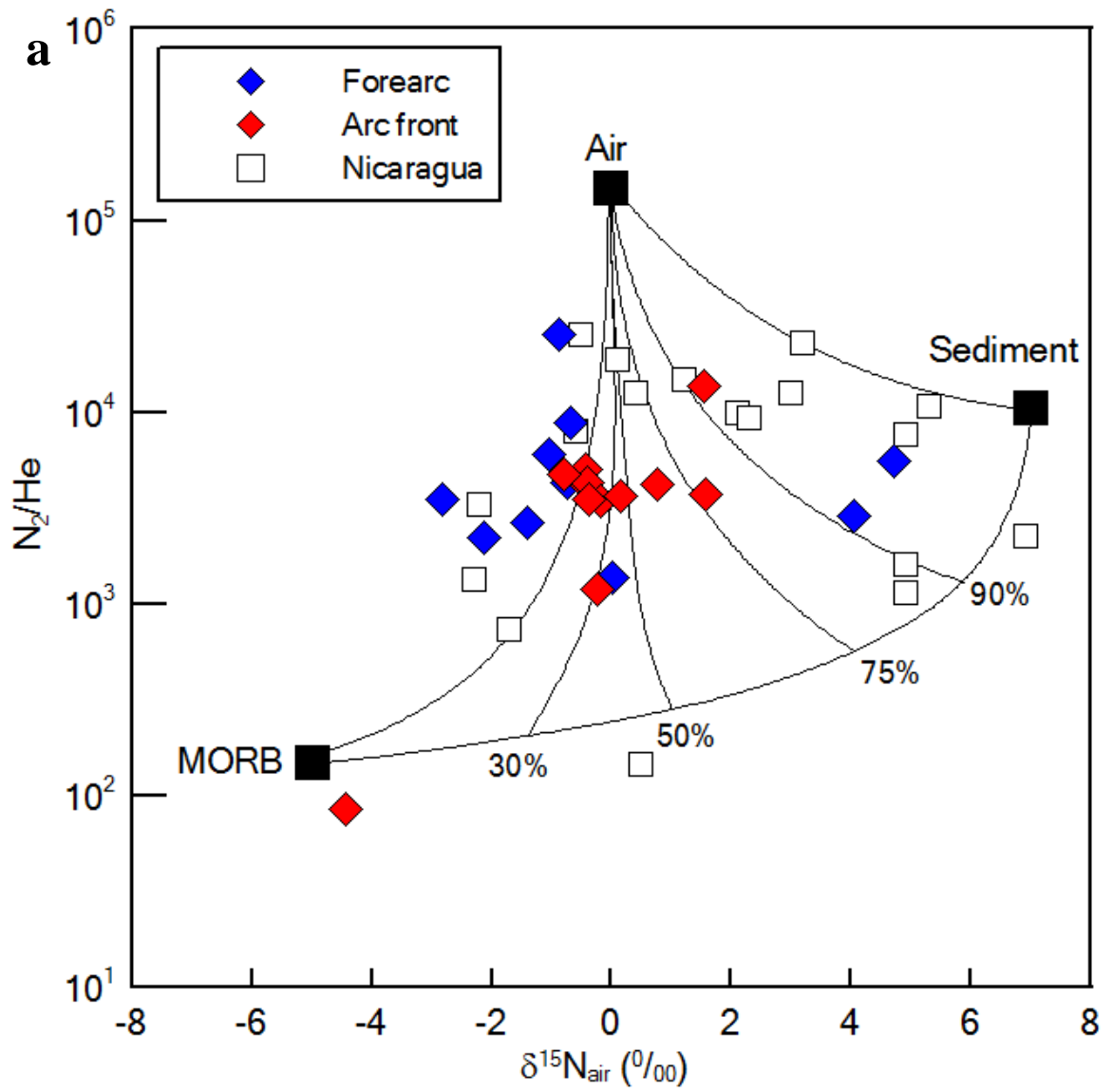
al., 2015) and thermal decomposition of ammonia (Li et al., 2009) have been proposed. But, fractionation factors suggested by these studies (< 1‰) are insufficient to explain the observed N isotope shift (Fig. 4a). For these reasons, N sources are constrained using the modified approach with $N_{2\text{-exc}}/\text{He}$ ratios following:

$$1/(N_{2\text{-exc}}/\text{He})_{\text{measured}} = f_{\text{MORB}}/(N_2/\text{He})_{\text{MORB}} + f_{\text{sediment}}/(N_2/\text{He})_{\text{sediment}} + f_{\text{air}}/(N_{2\text{-exc}}/\text{He})_{\text{air}} \quad (5)$$

where $(N_{2\text{-exc}}/\text{He})_{\text{air}}$ is 78,023 by reducing the ASW proportion, and $(N_2/\text{He})_{\text{MORB}}$ and $(N_2/\text{He})_{\text{sediment}}$ are the same values as above because we do not expect any air-derived N in these end-members. In Fig 4b. the $\delta^{15}\text{N}$ and $N_{2\text{-exc}}/\text{He}$ of the Costa Rican springs and Nicaraguan gases (Elkins et al., 2006) are displayed showing that now most samples lie within the mixing curves. The Air end-member in Fig. 4b now represents N_2 addition from air in the atmosphere and not dissolved in the water phase. Sediment contribution (f_{sediment}) to N of all Costa Rican springs ranges from 0 to 42%, except for the Osa (76%) and Burica (68%) springs (Table S2). Additionally, most of the Costa Rican springs at 9-11N° shows less sediment contribution compared to Guatemala ($f_{\text{sediment}} = 20 - 90\%$: Fischer et al., 2002) and Nicaragua ($f_{\text{sediment}} = 46 - 96\%$: Elkins et al., 2006) (Table S2).

$^3\text{He}/^4\text{He}$ and $^4\text{He}/^{20}\text{Ne}$ ratios of the Nicoya and Santa Elena forearc springs range from 0.61 to 1.09 Ra (Ra is $(^3\text{He}/^4\text{He})_{\text{air}} = 1.382 \times 10^{-6}$; Sano et al., 2013) and 0.24 to 5.33, respectively (Table 2). One arc front spring near Rincon de la Vieja volcano (Fig. 1) has $^3\text{He}/^4\text{He}$ and $^4\text{He}/^{20}\text{Ne}$ ratios of 7.88 Ra and 20.0, respectively (Table 1), which is a typical feature of Costa Rican volcanic fluids (Shaw et al., 2003; Zimmer et al., 2004). The $^4\text{He}/^{20}\text{Ne}$ ratios of dissolved gases in most of spring samples are close to the ASW ratio (0.25 at 0°C, Sano et al., 2006), which implies that atmospheric components are the major source for noble gases. This is also consistent with $^{40}\text{Ar}/^{36}\text{Ar}$ ratios (296.7 ± 7.5) which are

close to air ($^{40}\text{Ar}/^{36}\text{Ar} = 295.5$) (Supplementary Information). For these reason, the inverse ratios ($^{20}\text{Ne}/^4\text{He}$) can be used to extrapolate deep sources with linear mixing lines (Matsuda and Marty, 1995; Hong et al., 2010; Horiguchi et al., 2013). In Fig 5, all the forearc springs plot on the line indicating 10% mantle helium similar to what has been measured in submarine seep fluids off the coast of Costa Rica (Füri et al., 2010), implying that mantle fluids exist in the Nicoya and Santa Elena complexes.



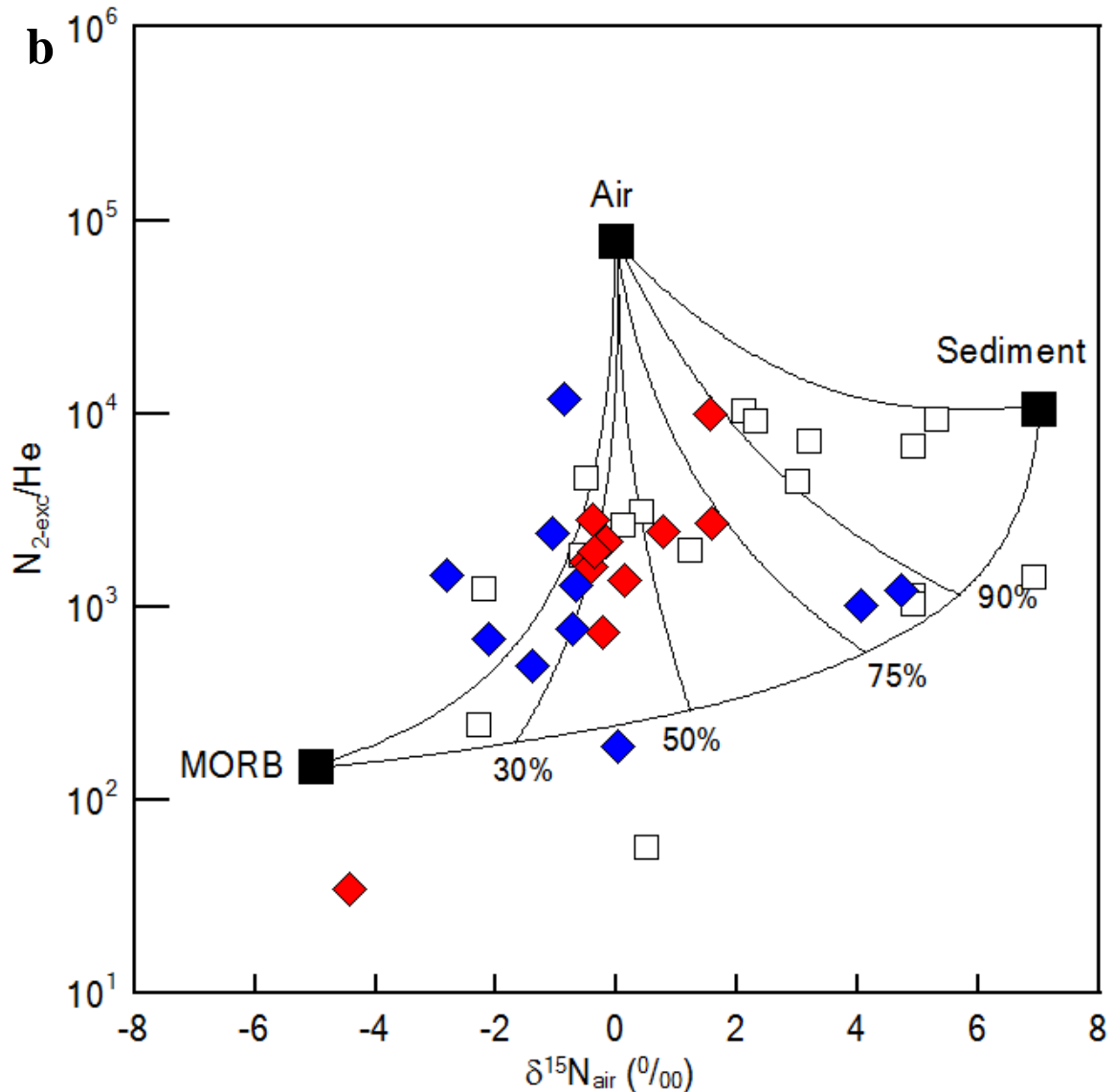


Figure 4. Nitrogen provenance diagram. a. nitrogen isotopes compositions versus N_2/He ratios of the Costa Rican springs. End-members and mixing lines are defined as described in Sano et al. (2001) and Fischer et al. (2002). Percentages of sediment input are shown. The Nicaraguan data is from (Elkins et al. 2006). b. nitrogen isotope compositions versus N_{2-exc}/He , which displays a less number of data points (for both this study and Elkins et al., 2006) off the mix line between MORB and air. N_{2-exc}/He of the air end-member was taken by reducing the ASW contribution.

5. DISCUSSION

N isotope compositions ($\delta^{15}\text{N} = -4.4$ to 1.6%) of all samples collected in Costa Rica ($9-11\text{N}^\circ$) indicate that less proportions of N associated with pelagic sediments are released by most of springs compared to Nicaragua (Fig. 4 and Table S2). Costa Rican volcanic arc gases have a smaller number of samples which have $\delta^{15}\text{N}$ values heavier than air (0%) compared to Nicaragua (Fig. 3 and 4) (Fischer et al., 2002; Zimmer et al., 2004). In Fig 4b and Table S2, the Nicoya forearc springs have less sediment fractions ($f_{\text{sediment}} = 0 - 3\%$) compared to the arc front springs ($f_{\text{sediment}} = 0 - 36\%$) implying that progressive N devolatilization of the subducted slab underneath Costa Rica is occurring. But, the N release from sediment into the Costa Rican arc is significantly less than in the Nicaraguan and Guatemalan arc sections where f_{sediment} is $46 - 96\%$ (Elkins et al., 2006) and $20 - 90\%$ (Fischer et al., 2002), respectively. There are still outliers on the corrected N provenance diagram, and further studies are required to consider kinetic N isotope fractionation processes, such as denitrifying bacteria activities in forearc areas as proposed by Matsushita et al. (2016).

Helium isotope ratios (${}^3\text{He}/{}^4\text{He} = 0.61 - 1.09 \text{ Ra}$) of the Nicoya and Santa Elena forearc areas are dominated by a crustal component. Lower ${}^3\text{He}/{}^4\text{He}$ ratios ($< 2 \text{ Ra}$) are common in other forearc springs, such as Japan, the North Island of New Zealand, and the Kamchatka peninsula of Russia (Sano and Fischer, 2013 and references therein). In Fig. 5, the extrapolated end-member of helium isotope ratios can be determined because deep sources (higher ${}^4\text{He}/{}^{20}\text{Ne}$ ratios) without severe air contamination can be displayed on the y-intercept. Taking linear mixing lines with different MORB (8 Ra) and crustal (0.02 Ra) (Ozima and Podosek, 2002) inputs into account, the Nicoya and Santa Elena forearc springs

are mainly derived from crustal fluids with significant atmospheric contribution (Fig. 5). It has been known that basement rocks of Nicoya and Santa Elena are uplifted Caribbean large Igneous Province (CLIP) components which has formed during Late Cretaceous associated with the Galapagos plume activity (Kerr et al., 2003 and references therein). The crustal feature of $^3\text{He}/^4\text{He}$ ratios in forearcs could be ascribed to old basement rocks resulting in radiogenic ^4He production by U-Th decay (Sano and Fischer, 2013 and references therein).

There are also other lines of geochemical evidence to indicate weak sediment input in the Costa Rican subduction zone. Ba/La ratios of the Costa Rican lavas (< 70) are lower than other Central American margin segments (e.g., Nicaragua, El Salvador, and Guatemala) which are up to ~ 130 (Carr et al., 2007). Much lower contents of ^{10}Be have been reported in the Costa Rican lavas than the Nicaraguan lavas (Morris et al., 2002). Pb and Nd radiogenic isotopes imply that magma sources at the Costa Rican volcanic front are less likely affected by sediments (Goss et al., 2006; Gazel et al., 2009). Several models have been suggested to account for less sediment contribution in Costa Rica. First, uppermost sediments enriched in organic materials are removed by underplating (Shipley et al., 1990). This process would result in less N contribution into the arc systems. But, the ODP legs 170 and 205 of off-shore Costa Rica show pelagic sediments are in fact subducting beyond the trench (Li and Bebout, 2005). Second, the shallower slab dip at Costa Rica having warmer thermal regime (Chen et al., 2001) would result in N loss at shallow depths through forearc devolatilization as proposed by Busigny et al. (2003) based on exhumed metamorphic rocks. This model has been adopted to explain limited fluid availability due to fluids released by metamorphic reactions in the Costa Rican arc (Feigenson and Carr,

1986; Carr et al., 1990; Rupke et al., 2002). The proposed sediment-derived N loss at forearc depths is invalid because forearc springs in Nicoya and Santa Elena have only small sediment contributions ($f_{\text{sediment}} = 0 - 3\%$). Finally, it is also unlikely that the incoming plate has a different composition and volume of sediments because off-shore Costa Rica has similar lithology and thickness in sediments subducted into the trench (ODP site 1039) to off-shore Guatemala (DSDP site 495) (Li and Bebout, 2005).

The subduction erosion model that explains the removal of continental material at the frontal or basal areas of continental margins has been favored by Morris et al. (1990), von Huene and Scholl (1991), Ranero and von Huene (2000), Clift et al. (2005), Goss et al. (2006), and Ranero et al. (2008). Compared to the Nicaragua and Guatemalan segments, Costa Rica has abundant seamounts on the Cocos plate at 9-11N° (Fig. 1) (Ranero and von Huene, 2000), which could enhance subduction erosion to dilute the signals of pelagic sediments (Morris et al., 2002; Goss et al., 2006). In addition, scars caused by seamount subduction have been observed in the upper plate in the frontal arc in Costa Rica (Sahling et al., 2008) (Fig. 1).

We next explore how this model could explain observed N isotope variations in the Costa Rica forearc and arc front. N isotope compositions of the Costa Rican springs at 9-11N° ($\delta^{15}\text{N} = -4.4$ to 1.6%) and reported values of volcanic arc gases ($\delta^{15}\text{N} = -3.0$ to 1.9% , Fischer et al., 2002; Zimmer et al., 2004; Fischer et al., 2015) are well consistent with the ranges of low-grade serpentinites ($\delta^{15}\text{N} = 0.6 \pm 3.4$) and oceanic crust ($\delta^{15}\text{N} = -1.2 \pm 3.7$) (Halama et al., 2014). These values are consistent with the observation that the Nicoya and Santa Elena forearc areas are ophiolite complexes at the western edge of the CLIP (Sinton et al., 1997; Hauff et al., 2000; Gazel et al., 2006; Tryon et al., 2010). Hence, the ophiolitic

materials are likely the primary N source in Nicoya and Santa Elena forearc springs. In Fig .3, most of arc front springs and volcanic gases (Fischer et al., 2002; Zimmer et al., 2004) are slightly heavier than the Nicoya and Santa Elena springs. This slight difference between forearc and arc front springs is likely due to increased $\delta^{15}\text{N}$ values during progressive devolatilization resulting in decrease of ^{14}N in the remaining materials (Li and Bebout, 2005). Seamount subduction is not observed at $< 9 \text{ N}^\circ$ at the Osa and Burica peninsulas consistent with heavier $\delta^{15}\text{N}$ values of the Osa and Burica springs due to the absence of subduction erosion in this region.

Globally, there are other areas associated with seamount subduction, such as the Sangihe ($\delta^{15}\text{N} = -7.3$ to 2.1% , Clor et al., 2005) and Mariana ($\delta^{15}\text{N} = -2.5$ to 1.6% , Mitchell et al., 2010) arcs where ^{15}N depleted signatures have been documented. The bathymetry of the Molucca sea floor in front of the Sangihe arc is not as smooth as nearby Celebes sea and Philippine sea plates due to the central ridge (Widiwijayanti et al., 2003). Also, the bathymetric map of the northwest Pacific (Plank et al., 2000) shows that the ocean floor is rough with numerous seamounts in front of the Mariana subduction zone. Therefore, the subduction erosion of serpentized overlying materials (e.g., low-grade serpentinite) enhanced by seamount subduction could result in contribution of N with the ranges of $\delta^{15}\text{N}$ values reported in Halama et al. (2014). Then, N from the upper plate materials dilutes subducted sediment input, which causes the N mass imbalance at the Costa Rican arc and transports heavier N into the deep mantle as suggested by Marty and Dauphas (2003), Jia et al. (2003), and Li and Bebout (2005).

6. CONCLUSIONS

We report new N isotopes compositions in the Costa Rican forearc and arc springs to account for ^{15}N -depleted signatures at the Costa Rican arc. Like N isotope compositions reported in volcanic arc gases (Fischer et al., 2002; Zimmer et al., 2004; Fischer et al., 2015), both forearc and arc front springs at 9-11N° display a similar range of $\delta^{15}\text{N}$ values. In comparison with other tectonic models for the limited amounts of sediment-derived N release (e.g., off-scraping, shallower slab dip, and different lithology and thickness in sediments), the subduction erosion enhanced by seamount subduction at 9-11N° is a better choice to explain the observation. The $\delta^{15}\text{N}$ values fall within the range of low-grade serpentinite or altered oceanic crust, which is consistent with the observation that the Nicoya and Santa Elena areas have oceanic floor materials formed by the Galapagos plume activity during Late Cretaceous. The seamounts subduction incorporates the overlying plate materials into the arc to dilute sediment-derived N contribution, and progressive devolatilization for N occurs from forearc to arc front. The release of ^{15}N -depleted volatiles supports the deep recycling of N at the Costa Rican subduction system.

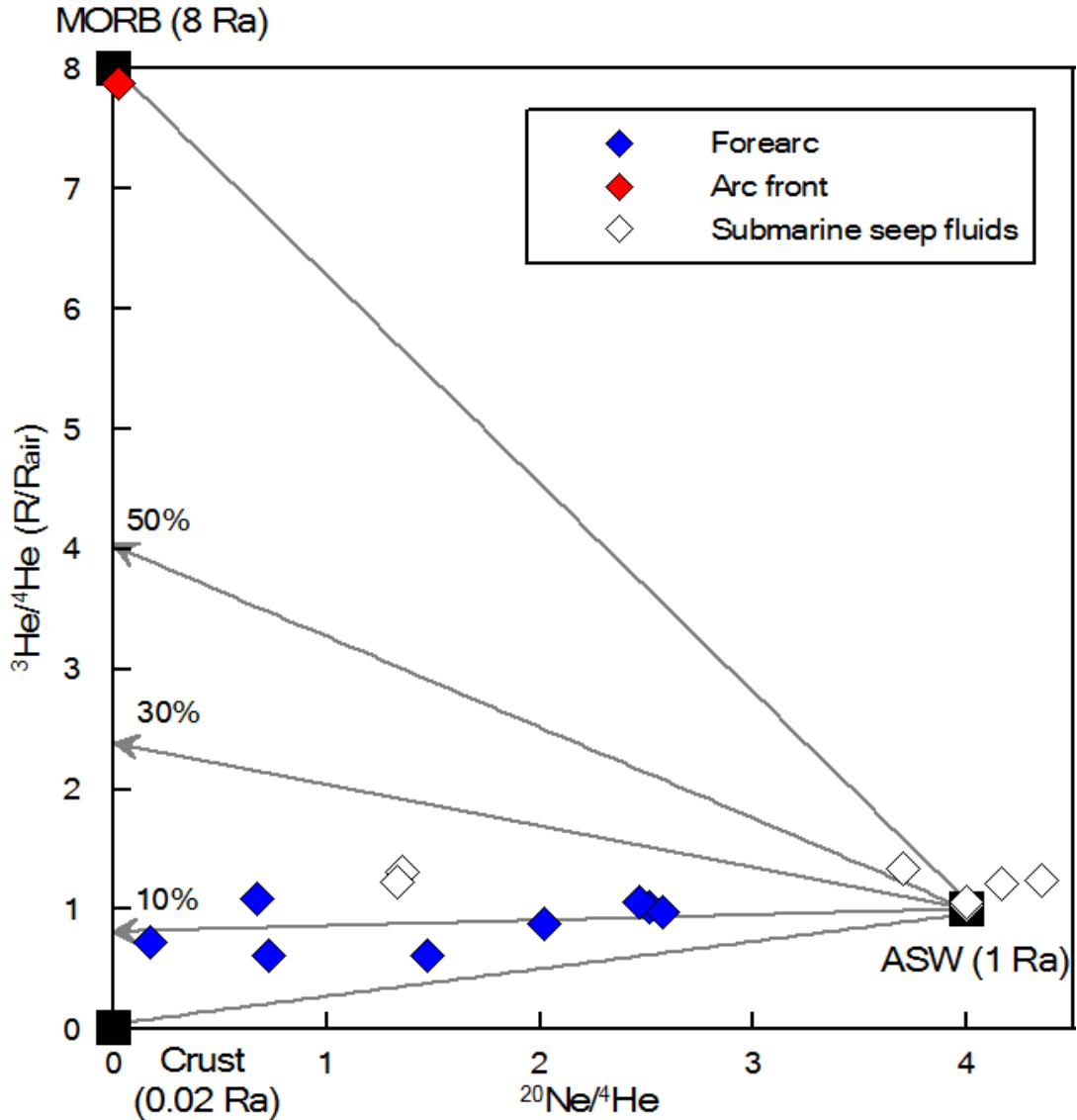


Figure 5. Plot of helium isotope ratios ($^3\text{He}/^4\text{He}$) versus $^{20}\text{Ne}/^4\text{He}$ with three components are MORB, crust, and ASW. The forearc data points include the Nicoya and Santa Elene springs, showing the mixing relationship between ASW and the hybrid fluid with 10 % MORB contribution. The arc front spring, located near the Rinconde la Vieja volcano (Fig. 1) is like the MORB component. The submarine seep fluids (Füri et al., 2010) are also mixed by two components (ASW and deep fluids with >10 % MORB input).

7. REFERENCES

- Agusto, M., Tassi, F., Caselli, A. T., Vaselli, O., Rouwet, D., Capaccioni, B., Caliro, S., Chiodini, G., Darrah, T. (2013) Gas geochemistry of the magmatic-hydrothermal fluid reservoir in the Copahue–Caviahue Volcanic Complex (Argentina). *J. Volcanol. Geotherm. Res.* **257**, 44-56.
- Arculus, R. J. (1994) Aspects of magma genesis in arcs. *Lithos* **33**, 189-208.
- Busigny, V., P. Cartigny, P. Philippot, and M. Javoy (2003) Nitrogen recycling in subduction zones: A strong geothermal control. *Geochim. Cosmochim. Acta* **67**, suppl. 1, A51.
- Carr, M. J., M. D. Feigenson, and E. A. Bennet (1990) Incompatible element and isotopic evidence for tectonic control of source mixing and melt extraction along the Central American arc. *Contrib. Mineral. Petrol.* **105**, 369–380.
- Carr, M. J., Saginor, I., Alvarado, G. E., Bolge, L. L., Lindsay, F. N., Milidakis, K., Turrin, B.D., Feigenson, M.D., and Swisher, C. C. (2007) Element fluxes from the volcanic front of Nicaragua and Costa Rica. *Geochem. Geophys. Geosyst.* **8** (6).
- Chen, P., C. R. Bina, and E. A. Okal (2001) Variations in slab dip along the subducting Nazca Plate, as related to stress patterns and moment release of intermediate-depth seismicity and to surface volcanism. *Geochem. Geophys. Geosyst.* **2**, 2001GC000153.
- Clift, P. D., Chan, L. H., Blusztajn, J., Layne, G. D., Kastner, M., and Kelly, R. K. (2005)

Pulsed subduction accretion and tectonic erosion reconstructed since 2.5 Ma from the tephra record offshore Costa Rica. *Geochem. Geophys. Geosyst.* **6** (9).

Clor, L. E., Fischer, T. P., Hilton, D. R., Sharp, Z. D., and Hartono, U. (2005) Volatile and N isotope chemistry of the Molucca Sea collision zone: Tracing source components along the Sangihe Arc, Indonesia. *Geochem. Geophys. Geosyst.* **6** (3).

de Moor, J. M. Fischer, T. P., Sharp, Z. D., Hilton, D. R., Barry, P. H., Mangasini, F., and Ramirez, C. (2013) Gas chemistry and nitrogen isotope compositions of cold mantle gases from Rungwe Volcanic Province, southern Tanzania. *Chem. Geol.* **339**, 30–42.

Elkins, L. J., Fischer, T. P., Hilton, D. R., Sharp, Z. D., McKnight, S., and Walker, J. (2006) Tracing nitrogen in volcanic and geothermal volatiles from the Nicaraguan volcanic front. *Geochim. Cosmochim. Acta* **70**, 5215-5235.

Feigenson, M. D., and M. J. Carr (1986) Positively correlated Nd and Sr isotope ratios of lavas from the Central American volcanic front. *Geology* **14**, 79–82.

Fischer, T. P., Giggenbach, W. F., Sano, Y., and Williams, S. N. (1998) Fluxes and sources of volatiles discharged from Kudryavy, a subduction zone volcano, Kurile Islands. *Earth Planet. Sci. Lett.* **160**, 81-96.

Fischer, T. P., Takahata, N., Sano, Y., Sumino, H., and Hilton, D. R. (2005) Nitrogen isotopes of the mantle: insights from mineral separates. *Geophys. Res. Lett.* **32**

(11).

Fischer, T. P., Hilton, D. R., Zimmer, M. M., Shaw, A. M., Sharp, Z. D., and Walker, J. A.

(2002) Subduction and recycling of nitrogen along the Central American margin. *Science* **297** (5584), 1154-1157.

Fischer, T.P., Ramirez, C., Mora-Amador, R., Hilton, D.R., Barnes, J.D., Sharp, Z.D., Le

Brune, M., de Moor, J.M., Furi, E., and Shaw, A.M. (2015) Temporal variations in fumaroles gas chemistry at Poas volcano, Costa Rica. *J. Volcanol. Geotherm. Res.* **294**, 56–70.

Füri, E., Hilton, D. R., Tryon, M. D., Brown, K. M., McMurtry, G. M., Brückmann, W.,

and Wheat, C. G. (2010) Carbon release from submarine seeps at the Costa Rica fore arc: Implications for the volatile cycle at the Central America convergent margin. *Geochem. Geophys. Geosyst.* **11** (4).

Giggenbach, W. F. (1995) Variations in the chemical and isotopic composition of fluids

discharged from the Taupo Volcanic Zone, New Zealand. *J. Volcanol. Geotherm. Res.* **68** (1), 89-116.

Gazel, E., Denyer, P., and Baumgartner, P. O. (2006) Magmatic and geotectonic

significance of Santa Elena Peninsula, Costa Rica. *Geologica Acta* **4** (1), 193.

Gazel, E., Carr, M. J., Hoernle, K., Feigenson, M. D., Szymanski, D., Hauff, F., and van

den Bogaard, P. (2009) Galapagos-OIB signature in southern Central America: Mantle refertilization by arc–hot spot interaction. *Geochem. Geophys. Geosyst.* **10** (2).

- Goss, A. R. and Kay, S. M. (2006) Steep REE patterns and enriched Pb isotopes in southern Central American arc magmas: Evidence for forearc subduction erosion? *Geochem. Geophys. Geosyst.* **7** (5).
- Giggenbach, W. F. and Goguel, R. L. (1989) Methods for The Collection and Analysis of Geothermal and Volcanic Water and Gas Samples. *Tech. Rep. CD 2401* (Department of Scientific and Industrial Research, Institute of Geological and Nuclear Sciences, New Zealand).
- Halama, R., Bebout, G. E., John, T., and Scambelluri, M. (2014) Nitrogen recycling in subducted mantle rocks and implications for the global nitrogen cycle. *International Journal of Earth Sciences* **103**, 2081-2099.
- Hauff, F., Hoernle, K., van den Bogaard, P., Alvarado, G., and Garbe-Schönberg, D. (2000) Age and geochemistry of basaltic complexes in western Costa Rica: Contributions to the geotectonic evolution of Central America. *Geochem. Geophys. Geosyst.* **1** (5).
- Hilton, D. R., Fischer, T. P. and Marty, B. (2002) Noble gases and volatile recycling at subduction zones. In: Noble Gases in Geochemistry and Cosmochemistry. *Reviews in Mineralogy and Geochemistry* **47** (eds Porcelli, D., Ballentine, C. J. & Wieler, R.) 319–370 (Mineralogical Society of America).
- Hong, W.L., Yang, T.F., Walia, V., Lin, S.J., Fu, C.C., Chen, Y.G., Sano, Y., Chen, C.H., and Wen, K.L. (2010) Nitrogen as the carrier gas for helium emission along an active fault in NW Taiwan. *Appl. Geochem.* **25**, 593–601.

- Horiguchi, K. and Matsuda, J. (2013) Geographical distribution of $^3\text{He}/^4\text{He}$ ratios in north Kyushu, Japan: Geophysical implications for the occurrence of mantle-derived fluids at deep crustal levels. *Chem. Geol.* **340**, 13–20 (2013).
- Huene, R. and Scholl, D. W. (1991) Observations at convergent margins concerning sediment subduction, subduction erosion, and the growth of continental crust. *Rev. Geophys.* **29**, 279-316.
- Kerr, A.C., White, R.V., Thompson, P.M., Tarnez, J., and Saunders, A.D. (2003) No oceanic plateau-no Caribbean Plate? The seminal role of an oceanic plateau in Caribbean Plate evolution. In: Bartolini, C., Buffler, R.T., Blickwede, J. (Eds.), The Circum-Gulf of Mexico and the Caribbean: hydrocarbon habitats, basin formation, and plate tectonics: *American Association of Petroleum Geologists (AAPG) Memoir*. **79**, pp. 126–188.
- Kienast, M. (2000) Unchanged nitrogen isotopic composition of organic matter in the South China Sea during the last climatic cycle: Global implications. *Paleoceanography* **15**, 244-253.
- Lee, H., Sharp, Z. D., and Fischer, T. P. (2015) Kinetic nitrogen isotope fractionation between air and dissolved N_2 in water: Implications for hydrothermal systems. *Geochem. J.* **49**, 571-573.
- Li, L. and Bebout, G. E. (2005) Carbon and nitrogen geochemistry of sediments in the Central American convergent margin: insights regarding subduction input fluxes, diagenesis, and paleoproductivity. *J. Geophys. Res.: Solid Earth* **110**

(B11).

- Li, L., Cartigny, P., and Ader, M. (2009) Kinetic nitrogen isotope fractionation associated with thermal decomposition of NH₃: Experimental results and potential applications to trace the origin of N₂ in natural gas and hydrothermal systems. *Geochim. Cosmochim. Acta* **73**, 6282-6297.
- Matsuda, J. I. and Marty, B. (1995) The ⁴⁰Ar/³⁶Ar ratio of the undepleted mantle; a reevaluation. *Geophys. Res. Lett.* **22**, 1937-1940.
- Marty, B. (1995) Nitrogen content of the mantle inferred from N₂-Ar correlation in oceanic basalts. *Nature* **377** (6547), 326.
- Marty, B., and Zimmermann, L. (1999) Volatiles (He, C, N, Ar) in mid-ocean ridge basalts: Assessment of shallow-level fractionation and characterization of source composition. *Geochim. Cosmochim. Acta* **63** 3619-3633.
- Mikhail, S., Barry, P. H., and Sverjensky, D. A. (2017). The relationship between mantle pH and the deep nitrogen cycle. *Geochim. Cosmochim. Acta* **209**, 149-160.
- Mitchell, E. C., Fischer, T. P., Hilton, D. R., Hauri, E. H., Shaw, A. M., de Moor, J. M., Sharp, Z.D., and Kazahaya, K. (2010) Nitrogen sources and recycling at subduction zones: Insights from the Izu-Bonin-Mariana arc. *Geochem. Geophys. Geosyst.* **11** (2).
- Morris, J. D., Leeman, W. P., and Tera, F. (1990) The subducted component in island arc lavas: constraints from Be isotopes B-Be systematics. *Nature* **344** (6261), 31.

- Morris, J., Valentine, R., and Harrison, T. (2002) ^{10}Be imaging of sediment accretion and subduction along the northeast Japan and Costa Rica convergent margins. *Geology* **30**, 59-62.
- Ozima, M. and Podosek, F. A. (1983) Noble Gas Geochemistry, 367 pp. (Cambridge Univ. Press).
- Peters, K. E., Sweeney, R. E., and Kaplan, I. R. (1978) Correlation of carbon and nitrogen stable isotope ratios in sedimentary organic matter. *Limnol. Oceanogr.* **23**, 598-604.
- Rubey, W. W. (1951) Geologic history of sea water an attempt to state the problem. *Geol. Soc. Am. Bull.* **62**, 1111-1148.
- Plank, T., Ludden, J. N., Escutia, C., and Party, S. S. (2000) Leg 185 summary; inputs to the Izu–Mariana subduction system. *Ocean Drilling Program Proceedings, Initial Reports, Leg 185*, 1-63.
- Ranero, C. R. and von Huene, R. (2000) Subduction erosion along the Middle America convergent margin. *Nature* **404**, 748-752.
- Ranero, C. R., Grevemeyer, I., Sahling, H., Barckhausen, U., Hensen, C., Wallmann, K., Weinrebe, W., Vannucchi, P., von Huene, R., and McIntosh, K. (2008) Hydrogeological system of erosional convergent margins and its influence on tectonics and interplate seismogenesis. *Geochem. Geophys. Geosyst.* **9** (3).
- Rupke, L. H., J. P. Morgan, M. Hort, and J. A. D. Connolly (2002) Are the regional variations in Central American arc lavas due to differing basaltic versus

peridotitic slab sources of fluids?. *Geology* **30**, 1035–1038.

Ryan, W. B. F., Carbotte, S. M., Coplan, J. O., O'Hara, S., Melkonian, A., Arko, R., Weissel, R. A., Ferrini, V., Goodwillie, A., Nitsche, F., Bonczkowski, J., and Zemsky, R. (2009) Global multi-resolution topography synthesis. *Geochem. Geophys. Geosyst.* **10**. <http://dx.doi.org/10.1029/2008GC002332>.

Sahling, H., D. G. Masson, C. R. Ranero, V. Hühnerbach, W. Weinrebe, I. Klauke, D. Bürk, W. Brückmann, and E. Suess (2008), Fluid seepage at the continental margin offshore Costa Rica and southern Nicaragua. *Geochem. Geophys. Geosyst.* **9**, Q05S05, doi:10.1029/2008GC001978.

Sano, Y. and Fischer, T. P. (2013) The analysis and interpretation of noble gases in modern hydrothermal systems. In: *The Noble Gases as Geochemical Tracers. Advances in Isotope Geochemistry* (ed Burnard, P.) 249–317 (Springer-Verlag).

Sano, Y., Takahata, N., and Seno, T. (2006) Geographical distribution of $^3\text{He}/^4\text{He}$ ratios in the Chugoku district, Southwestern Japan. *Pure Appl. Geophys.* **163**, 745-757.

Sano, Y., Tokutake, T., and Takahata, N. (2008) Accurate measurement of atmospheric helium isotopes. *Analytical Sciences* **24**, 521-525.

Sano, Y., Marty, B. & Burnard, P. Noble gases in the atmosphere. In: *The Noble Gases as Geochemical Tracers. Advances in Isotope Geochemistry* (ed. Burnard, P.) 17–31 (Springer-Verlag 2013).

Sano, Y., Takahata, N., Nishio, Y., Fischer, T. P., and Williams, S. N. (2001) Volcanic flux

of nitrogen from the Earth. *Chem. Geol.* **171**, 263-271.

Shaw, A. M., Hilton, D. R., Fischer, T. P., Walker, J. A., and Alvarado, G. E. (2003) Contrasting He–C relationships in Nicaragua and Costa Rica: insights into C cycling through subduction zones. *Earth Planet. Sci. Lett.* **214**, 499-513.

Shiple, T. H., and G. F. Moore (1986), Sediment accretion, subduction, and dewatering at the base of the trench slope off Costa Rica: A seismic reflection view of the decollement, *J. Geophys. Res.* **91**, 2019–2028.

Sinton, C. W., Duncan, R. A., and Denyer, P. (1997) Nicoya Peninsula, Costa Rica: A single suite of Caribbean oceanic plateau magmas. *J. Geophys. Res.* **102**, 15507-15520.

Tardani, D., Reich, M., Roulleau, E., Takahata, N., Sano, Y., Pérez-Flores, P., Sánchez, P., Cembrano, J., and Arancibia, G. (2016) Exploring the structural controls on helium, nitrogen and carbon isotope signatures in hydrothermal fluids along an intra-arc fault system. *Geochim. Cosmochim. Acta* **184**, 193-211.

Tatsumi, Y., Sakuyama, M., Fukuyama, H., and Kushiro, I. (1983) Generation of arc basalt magmas and thermal structure of the mantle wedge in subduction zones. *J. Geophys. Res.: Solid Earth* **88** (B7), 5815-5825.

Tryon, M. D., Wheat, C. G., and Hilton, D. R. (2010) Fluid sources and pathways of the Costa Rica erosional convergent margin. *Geochem. Geophys. Geosyst.* **11** (4).

Widiwijayanti, C., Mikhailov, V., Diament, M., Deplus, C., Louat, R., Tikhotsky, S., and Gvishiani, A. (2003) Structure and evolution of the Molucca Sea area:

constraints based on interpretation of a combined sea-surface and satellite gravity dataset. *Earth Planet. Sci. Lett.* **215**, 135-150.

Zimmer, M. M., Fischer, T. P., Hilton, D. R., Alvarado, G. E., Sharp, Z. D., and Walker, J. A. (2004) Nitrogen systematics and gas fluxes of subduction zones: Insights from Costa Rica arc volatiles. *Geochem. Geophys. Geosyst.* **5** (5).

APPENDIX 1: SUPPLEMENTARY INFORMATION FOR CHAPTER 2

A.1.1. SUPPLEMENTARY TEXT

A.1.1.1. Definition of tectonic degassing

The term tectonic degassing was coined by Burton et al. (2013), and can be used to differentiate mantle-derived CO₂ degassing at active volcanic centers (e.g., composite volcanoes, caldera complexes) from areas that are not directly affected by volcanism at the surface. CO₂ released from tectonic degassing is sourced from the mantle (e.g., Apennines, Italy; Chiodini et al., 2004) and ascends the crust through fault networks before reaching the surface in areas away from any observable volcanoes. Therefore, three specific criteria must be met under a tectonic degassing model: (1) the CO₂ must have a magmatic (mantle-derived) signature; (2) the CO₂ must ascend through the crust along faults and fractures; and (3) the CO₂ must reach the surface away from volcanic centers (e.g., composite volcanoes).

A.1.1.2. Definition of structural zones from field-based analyses and aerial mapping

We observed the highest CO₂ flux in the vicinity of faults, in a zone extending outward from the base of the fault scarp over a distance equal to the fault throw (*fault zone* in Figs. S3, S4, and Fig. 3 of the main text). Permeable sediments in faulted grabens also exhibited higher flux values than those observed in impermeable lavas in uplifted footwalls. Based on these observations, we subdivided all CO₂ flux measurements into three categories based on sample location relative to fault structure and surface geology. These structural

categories include: (1) *fault zones*, defined as the area directly adjacent to the fault scarp and extending outward on the downthrown side of the fault to a distance equal to the maximum throw; (2) *hanging walls*, the downthrown side of the fault excluding the fault zone and characterized by sedimentary fill; and (3) *footwalls*, the uplifted side of the fault comprising primarily rift lavas with a thin veneer of sediments in places (Fig. S4).

A.1.1.3. Structural controls on CO₂ degassing

Categorizing flux measurements into the three zones outlined above revealed distinct distributions in diffuse CO₂ flux data (Fig. S4, Table S2, and Fig. 3 of the main text). Measurements in fault zones exhibited 2 to 17 times greater mean CO₂ flux than background values recorded in the hanging walls and footwalls of faults (Table S2). Furthermore, mean flux values in the permeable sediment fill in downthrown hanging walls were 5 to 11 times greater than mean flux in impermeable rift lavas in uplifted footwalls. Consistent with previous studies of diffuse CO₂ flux in tectonically active regions (Jolie et al., 2015), these results imply a structural control on the flux of CO₂ through the Magadi-Natron basin. High CO₂ flux occurred near the base of fault scarps, suggesting focused flow of CO₂-rich fluids through fault structures with high crustal permeability (Burton et al., 2013), which is further supported by observations of aligned spring systems at the base of some fault scarps (Table S4, and Fig. 3 of the main text). Faults in the Magadi-Natron basin form as dilational normal faults (Crosseley, 1979; Angelier et al., 1997), which produce fault-related apertures in the near the surface (<500 m depth: Crant and Kattenhorn, 2004) that likely facilitate diffuse CO₂ transport into overlying sediments. In the shallow subsurface, CO₂ spreads diffusely throughout these permeable sediments in the

hanging wall of the fault (for example, Jolie et al., 2015), with negligible flux occurring through impermeable rift lavas in the uplifted footwall (Fig. S4, Table S2, and Fig. 3 of the main text).

A.1.1.4. Estimating CO₂ flux in the Magadi-Natron basin and Eastern rift of the EAR

Although CO₂ gas emits diffusely over the 982 km² study area in the Magadi-Natron basin, there are clear differences in flux within the three structural zones defined above (Fig. S4 and Table S2). To account for these observed variations, we calculate total flux within each of our defined zones by multiplying the area of each zone (Fig. S3 and Table S3) by its mean CO₂ flux (Table S2). These values are then summed to calculate total diffuse CO₂ flux in the study area (Table S3). The areas occupied by downthrown graben sediments and uplifted trachyte lavas on the hanging walls and footwalls of faults, as well as fault traces (Fig. S3), were mapped from aerial photography (0.5 m resolution), Landsat 7 false color imagery (15 m resolution) and the Aster GDEM v.2 (30 m resolution), and validated in the field. Applying the method of ref. 7, fault throw (T) was estimated from the throw-length scaling relationship within the Magadi-Natron fault population using $T = \gamma L$ (Eq. 1), where L is fault length and γ is the throw/length coefficient. Our study used a γ of 0.0061 for faults of the Magadi-Natron basin, which was estimated from 30 faults measured from the Aster GDEM v.2 and aerial photography (0.5 m resolution). This value of γ is similar to dilation normal fault systems forming in rift lavas in Iceland (0.006; ref. 5) The area of the fault zone for each fault was then calculated by multiplying the fault length by fault throw calculated using equation 1.

Uncertainties in our flux estimates are reported as the standard error of the sample distributions (Tables S2, S3). Previous field studies of diffuse CO₂ degassing used a densely-sampled grid over comparatively smaller areas, collecting ~10-100 samples per km² (ref. 8, 9) compared to ~1 per km² collected for this work. However, our study area is 1 to 2 orders of magnitude larger than those of previous studies and was, therefore, comparatively sparsely sampled (565 measurements over 982 km²). The diffuse CO₂ flux is also clearly influenced by fault structure and permeability of the substrate (Fig. S4). These two factors limit the application of existing methods of geostatistical analysis (for example SGeMS) used to quantify total CO₂ flux (Deutsch and Journel, 1998; Werner and Cardellini, 2006; Chiodini et al., 2008). For these reasons, we suggest that the “structural-area method” outlined in the section above (Table S3) currently provides the most robust estimate of total CO₂ flux for the study site. It is, however, challenging to estimate the extent to which our collected flux data represents a fair distribution of CO₂ flux in the defined structural zones. We have therefore used a conservative estimate of total flux across the entire Magadi-Natron basin. Essentially, we calculated a CO₂ flux of 4.05 Mt yr⁻¹ over only ~10% of the 9,200 km² Magadi-Natron basin (combined study area = 982 km²; Fig. S3 and Table S3), but conservatively assumed that this amount represents the total flux across the entire Magadi-Natron basin. In this study, the basin length is defined as the distance from Oldoinyo Lengai to Suswa volcano (184 km long), and basin width is defined as the distance from the western border fault system to the eastern edge of the faulted monoclinial flexure in the hanging wall of the half-graben structure (50 km wide; Foster et al., 1997). Assuming a total CO₂ flux of 4.05 Mt yr⁻¹ for the 9,200 km² Magadi-Natron basin equates to a minimum value of flux per unit area of 4.4×10^2 t km⁻² yr⁻¹. This

conservative value is one to two orders of magnitude lower than typical flux per unit area estimates of tectonic degassing in smaller ($\sim 10^1$ km²), geothermal regions elsewhere (Morner and Etiope, 2002), yet the total flux is significant compared to flux values from historically active volcanoes (Fig. S5).

The minimum CO₂ flux calculated for the Magadi-Natron basin may be used to extrapolate an estimate of CO₂ flux for the entire Eastern rift of the EAR. We applied rift dimensions in accordance with Ebinger and Scholz (2012), and define the Eastern rift to include rift basins from the Afar depression southward to the Kilombero rift over a total area of $3,240 \times 50$ km. By extrapolating CO₂ flux per unit area from the Magadi-Natron basin (4.4×10^2 t km⁻² yr⁻¹) across the Eastern rift, we make a number of assumptions about the nature of magmatism, faulting, and fluid migration in this rift sector. First, we assume that strain accommodation proceeds in a similar manner across the Eastern rift via dike intrusion and faulting. Second, plate spreading is accommodated across the full width of rift basins, as suggested by the distribution of seismicity observed across the Eastern (Nyblade et al., 1996; Hollnack and Stangl, 1998; Ibs-von Seht et al., 2001; Keir et al., 2006; Keir et al., 2009; Belachew et al., 2011) (Fig. 1 of the main text). Third, we assume that the faulted basins are underlain by zones of magma intrusion, as detected in geophysical imaging, and detection of active intrusions (Keller et al., 1994; Birt et al., 1997; Ibs-von Seht et al., 2001; Keranen et al., 2004; Calais et al., 2008; Keir et al., 2009; Belachew et al., 2011). Fourth, we assume that fluids exsolved from these crustal and upper mantle magma bodies migrate through permeable fault zones, which is supported by fluid-driven lower crustal and upper mantle earthquakes observed in the Albertine rift basin

(Lindenfeld et al., 2012) and in magmatic rifts elsewhere (e.g., Taupo Rift, New Zealand; Reyners et al., 2007).

A.1.1.5. Sources of CO₂ in the Magadi-Natron basin

CO₂ is removed from the mantle by the generation and ascent of magma. It exsolves from magma during cooling, crystallization and decompression, before rising through lithosphere along fractured, permeable pathways (Geissler et al., 2005; Burton et al., 2013). Seismic and magnetotelluric studies along the Eastern rift provide evidence for volumetrically significant accumulations of magma at depth (Keller et al., 1994; Birt et al., 1997; Ibs-von Seht et al., 2001; Kendall et al., 2004; Keranene t al., 2004; Whaler and Haulot, 2006; Calais et al., 2008; Keir et al., 2009; Keir et al., 2011). This magma is the likeliest source of the mantle-derived CO₂ measured at the surface. Here we discuss the possible location of the source (upper crust, lower crust, or upper mantle) in the Magadi-Natron basin based on previous work and the lower crustal seismicity presented in this study.

Upper crust. Although two shallow dike intrusions (< 10 km deep) have been detected by InSAR and temporary seismic arrays in the Magadi-Natron basin in the last 20 years (Hollnack and Stangl, 1998; Ibs-von Seht et al., 2001; Biggs et al., 2009), the volume of these intrusions is too small to supply the estimated 4.05 Mt yr⁻¹ of CO₂. For example, assuming that the 2.4 m-wide, 7 km-long and 4 km-high 2007 Natron dike (Calais et al., 2008; Biggs et al., 2009) consisted of 1 wt% CO₂ and had a density of 3000 kg m⁻³, it would have sourced only 2 Mt of CO₂ to the Magadi-Natron basin 7 years prior to the current survey. Based on analogy to other rift sectors (e.g., Main Ethiopian Rift; Keller et al., 1994;

Keir et al., 2009), the primary CO₂ is thus likely sourced from lower crustal and mantle lithosphere magma bodies.

Lower crust and Upper mantle. Anomalously low uppermost mantle (Pn) velocities across the Magadi sector of the Kenya Rift can be explained by a zone of ~5% partial melt (Keller et al., 1994; Birt et al., 1997). CO₂ may exsolve from magmas in the partial melt zone, and then travel vertically through faults in a strong, mafic lower crust, resulting in the observed deep seismicity (e.g., Kennedy et al., 1997; Lindenfeld et al., 2012). Alternatively, lower crustal seismicity could also be caused by active magma intrusion (Keir et al., 2009) and volatile-driven hydraulic fracturing along the margins of modern dike and sill intrusions (Albaric et al., 2014), or in some places represent detachment faulting (Mulibo and Nyblade 2009).

A.1.2. SUPPLEMENTARY FIGURES AND TABLES

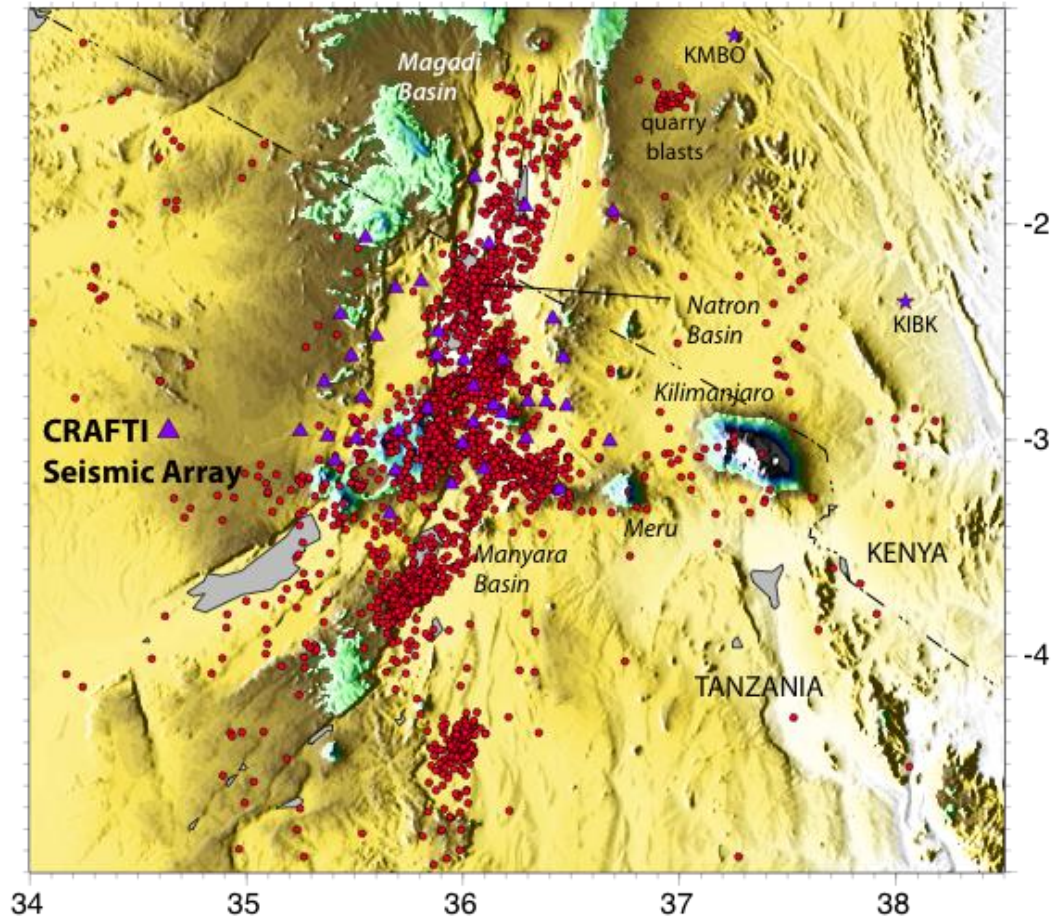


Figure S1. CRAFTI seismic network (purple triangles) and GEOFON stations KIBK and KMBO also used in event locations (red circles).

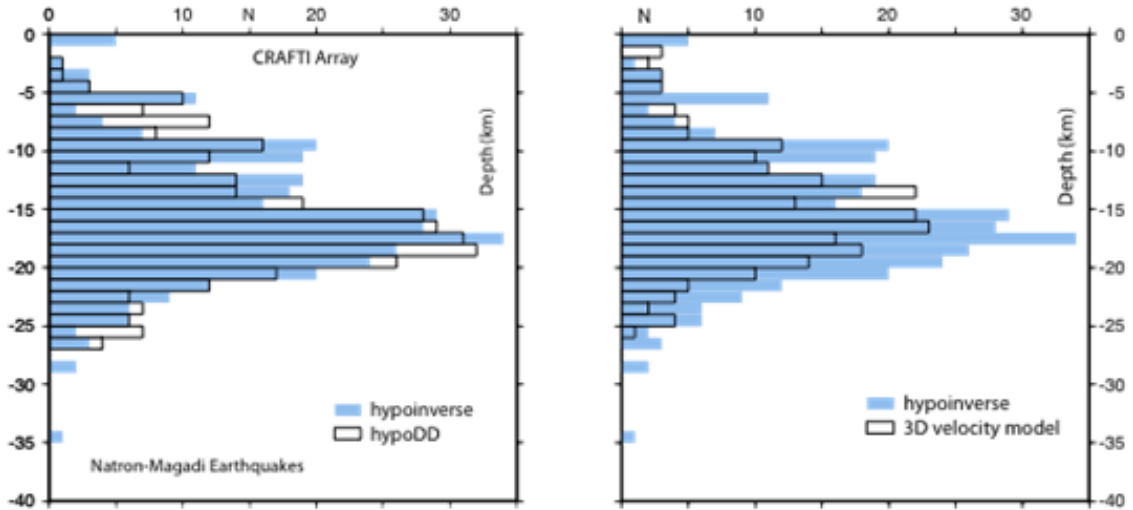


Figure S2. Histograms comparing depths of CRAFTI earthquakes in the Natron and Magadi basins (excluding Gelai earthquakes). Earthquakes located using hypoinverse are compared to those relocated using the double-difference algorithm (left) and a sub-set relocated in the 3D tomographic inversion (right). The pattern of depth distributions show little variation between methods, demonstrating a significant set of earthquakes in the lower crust (> 15 km) along the length of the Natron and Magadi basins.

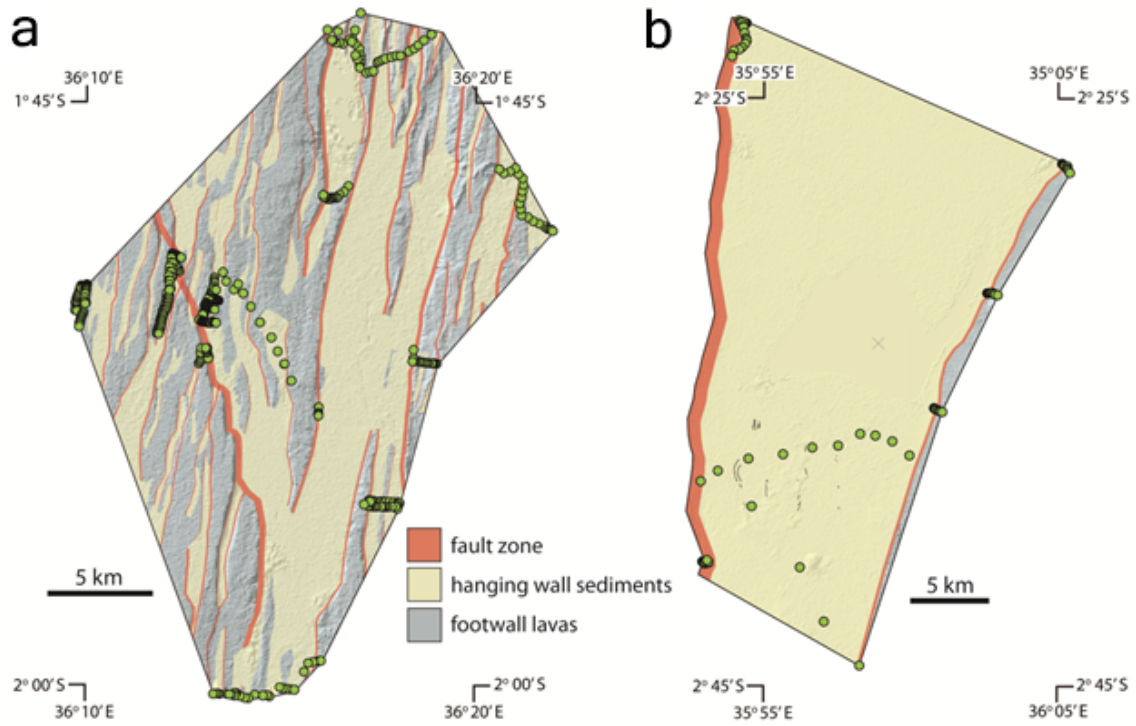


Figure S3. Areal distributions of fault zones, hanging wall sediments, and footwall lavas in the Magadi (a) and Natron (b) basin study areas. Structural zones are overlain on an Aster GDEM v.2 hillshade. Locations of CO₂ flux measurements are presented as green circles. Small faults (10s to 100s of meters long) and short gaping fissures (10s of meters long) mapped in the field by Sherrod et al. (2013) are presented as black lines.

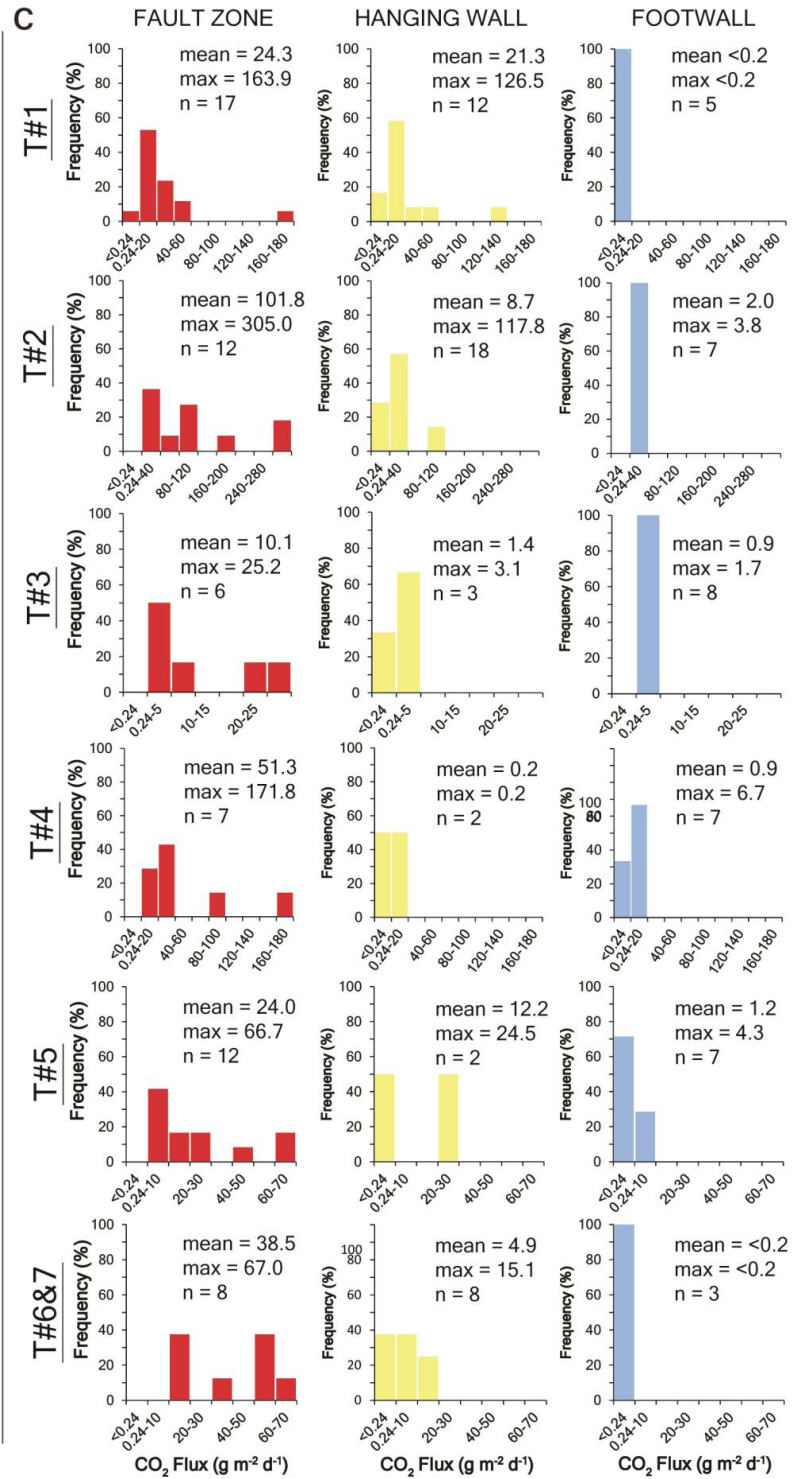
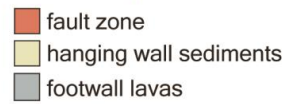
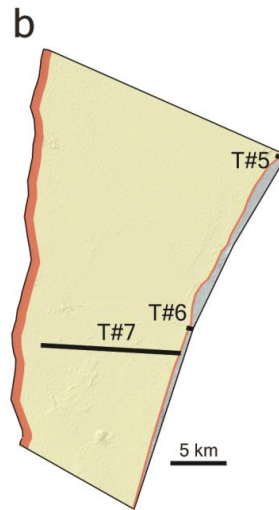
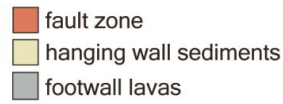
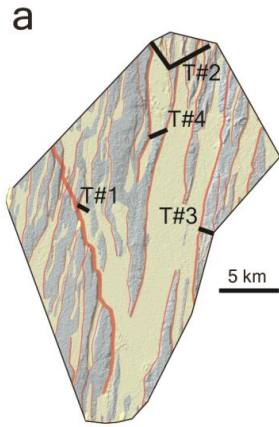


Figure S4. Diffuse CO₂ flux data from 7 transects across the Natron-Magadi basin.
a,b, general location of each transect in the Magadi (a) and Natron (b) study areas.
Transect numbers (e.g., T#1, T#2) correspond to transect numbers of histograms in (c). Coordinates of study areas and sample locations are shown in Fig. S1. c, Histograms of diffuse CO₂ flux in fault zones (red), hanging walls (yellow), and footwalls (blue) from the transects shown in (a) and (b). Units for mean and max values are g m⁻² d⁻¹.

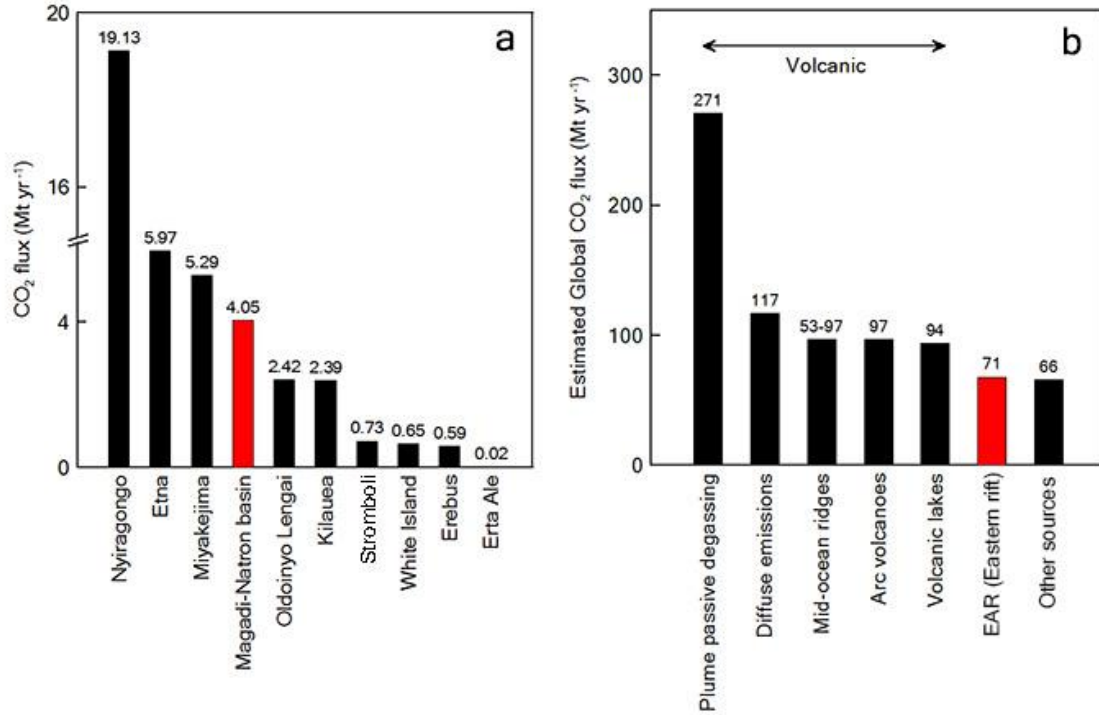


Figure S5. Histograms of CO₂ flux. a. Annual CO₂ flux from tectonic degassing in the Magadi-Natron basin and a selection of volcanoes worldwide¹. b. CO₂ flux from tectonic degassing in the EAR (Eastern rift) compared with global estimates from volcanoes and other basin sources (tectonic, hydrothermal, or inactive volcanic) (Marty and Tolstikhin, 1998; Pérez et al., 2011; Burton et al., 2013; Kagoshima et al., 2015).

Table S1. Locations, gas compositions, C isotope values, and structural divisions of measured samples from the Magadi and Natron basin study areas and Oldoinyo

Lengai North Crater.

Area	sample ID	location		Ar	N ₂	O ₂	CO ₂	He	H ₂	CH ₄	CO	δ ¹³ C-CO ₂	structural
		latitude (S°)	Longitude (E°)	vol. %			ppm					% vs. PDB	division
Magadi	A1P44	1.828625	36.167317	0.70	83.19	16.02	944.42	6.84	8.26	b.d.	b.d.	-8.5	FZ
	A1P63	1.84275	36.165028	0.70	83.28	15.94	832.00	7.11	5.45	b.d.	b.d.	-9.2	FZ
	A1P43	1.828289	36.167503	0.85	82.27	16.79	824.71	2.21	6.14	b.d.	16.03	-7.7	FZ
	A1P39	1.829833	36.165639	0.71	83.64	15.56	863.52	7.23	5.47	b.d.	b.d.	-9.6	HW
	A1P67	1.845944	36.164417	0.67	78.47	20.78	800.38	7.44	5.63	b.d.	b.d.	-8.7	FZ
	A2P82	1.838444	36.200167	0.66	80.61	18.66	642.53	6.49	5.35	b.d.	b.d.	-8.1	FZ
	A2P76	1.843972	36.198778	0.69	81.51	17.74	645.68	6.82	9.16	b.d.	16.32	-8.0	FZ
	A2P69	1.848028	36.1975	0.68	80.45	18.78	869.88	6.60	6.07	b.d.	b.d.	-10.1	FZ
	A2P86	1.834333	36.201639	0.66	80.85	18.42	688.76	7.29	5.62	b.d.	b.d.	-7.8	FW
	A3P5	1.859028	36.216361	0.76	78.94	20.22	803.95	0.96	5.86	b.d.	b.d.	-8.4	FZ
	A3P13	1.8575	36.218989	0.70	82.03	17.15	1223.27	9.21	4.26	b.d.	b.d.	-9.1	FZ
	A3P9	1.856528	36.216472	0.81	76.97	22.15	698.69	1.49	5.40	b.d.	b.d.	-9.9	HW
	A3P18	1.859328	36.219308	0.59	79.38	19.84	1882.03	13.47	4.37	b.d.	b.d.	-7.6	FZ
	A3P8	1.856833	36.216667	0.70	81.43	17.81	544.99	10.88	8.60	b.d.	b.d.	-7.2	FZ
	A3P21	1.85575	36.218472	0.70	83.55	15.36	3803.59	7.51	6.70	b.d.	b.d.	-7.9	FZ
	A4P27	1.835535	36.21852	0.86	82.60	16.46	768.65	1.47	4.57	b.d.	b.d.	-8.5	FZ
	A4P94	1.834439	36.222847	0.66	80.38	18.86	994.93	5.74	8.15	b.d.	15.77	-7.5	HW
	A4P82	1.844181	36.219661	0.86	82.32	16.70	1201.33	1.41	13.01	b.d.	b.d.	-7.1	HW
	A4P101	1.834103	36.220825	0.68	80.96	18.23	1314.96	6.61	6.58	b.d.	b.d.	-7.3	HW
	A4P111	1.836356	36.219469	0.82	81.82	17.31	578.11	7.43	6.45	b.d.	b.d.	-7.3	HW
	A4P113	1.8369	36.220089	0.71	80.05	19.14	990.99	7.67	6.11	b.d.	b.d.	-7.1	HW
	A4P81	1.844089	36.219269	0.65	81.23	17.99	1223.57	6.45	12.23	b.d.	18.19	-6.5	HW
	A4P90	1.844239	36.222794	0.68	82.28	16.95	919.84	5.70	8.27	b.d.	b.d.	-7.5	FZ
	A4P99	1.834244	36.221225	0.81	80.60	18.49	1025.56	2.30	5.75	b.d.	b.d.	-7.4	HW
A4P108	1.835656	36.218458	0.82	80.51	18.62	464.87	10.02	4.94	b.d.	b.d.	-7.9	FZ	
A4P115	1.837517	36.220681	0.70	81.67	17.53	988.54	7.20	6.40	b.d.	b.d.	-5.9	HW	
A4P120	1.838653	36.221867	0.69	82.52	16.68	1053.10	11.22	4.88	b.d.	b.d.	-7.5	FZ	
A5P19	1.815472	36.205722	0.79	79.51	19.65	520.77	8.36	6.44	b.d.	b.d.	-8.3	HW	
A5P24	1.816417	36.207694	0.68	82.31	16.91	958.17	10.92	3.74	b.d.	b.d.	-7.8	FZ	

A5P34	1.824361	36.203278	0.69	80.32	18.91	835.54	9.20	9.12	b.d.	11.93	-8.6	HW
A5P21	1.815889	36.2065	0.79	82.61	16.53	663.78	8.99	4.47	b.d.	b.d.	-7.4	HW
A6P54	1.830889	36.22075	0.61	79.55	19.77	710.90	13.86	4.32	b.d.	b.d.	-8.0	FZ
A6P50	1.829417	36.221194	0.67	80.95	18.29	873.04	6.04	5.84	b.d.	13.99	-11.1	FZ
A6P52	1.831139	36.220667	0.69	82.27	16.89	1360.76	7.29	10.39	b.d.	b.d.	-6.5	FZ
A7P30	1.921111	36.288222	0.74	82.89	16.29	784.68	11.22	9.06	b.d.	10.48	-5.8	HW
A7P26	1.922417	36.288417	0.80	80.20	18.94	617.14	13.02	4.59	b.d.	b.d.	-10.2	HW
A7P14	1.922694	36.3	1.08	80.64	18.22	573.68	8.71	5.69	b.d.	b.d.	-7.4	FZ
A7P4	1.920306	36.289306	0.71	80.22	18.99	759.74	9.05	9.89	b.d.	b.d.	-6.4	HW
A7P22	1.922611	36.292944	0.70	80.63	18.58	915.98	6.14	7.09	b.d.	15.99	-7.7	FW
A7P12	1.921056	36.300694	0.68	80.72	18.51	881.32	6.31	17.93	b.d.	16.64	-8.9	FZ
A7P5	1.920361	36.292444	0.83	82.34	16.78	484.60	7.68	7.52	b.d.	13.83	-7.1	HW
A7P19	1.922639	36.294639	0.71	82.14	17.07	834.17	7.29	6.63	b.d.	16.45	-6.7	FZ
A7P11	1.920778	36.300111	0.67	81.11	18.13	818.68	6.94	6.21	b.d.	b.d.	-6.9	HW
A7P8	1.920528	36.294722	0.69	82.46	16.79	543.74	7.94	5.11	b.d.	b.d.	-8.1	FZ
A7P29	1.922139	36.28775	0.86	82.56	16.51	659.63	9.54	4.19	b.d.	b.d.	-7.6	FZ
A8P35	1.988944	36.264167	0.69	82.05	17.19	686.65	10.77	4.64	b.d.	b.d.	-6.2	FZ
A8P40	2.000389	36.25275	0.72	81.21	17.97	969.67	8.67	12.59	b.d.	b.d.	-7	HW
A8P50	2.00225	36.231458	0.68	82.23	16.98	1021.22	7.66	11.89	b.d.	b.d.	-7.3	FZ
A8P42	1.999722	36.249889	0.67	82.17	17.09	662.11	6.05	7.51	b.d.	b.d.	-8.5	HW
A9P9	1.730319	36.298964	0.70	82.11	17.11	842.79	6.70	6.90	b.d.	17.19	-9.3	FZ
A9P5	1.732603	36.291972	0.86	81.06	18.03	497.51	2.31	8.45	b.d.	b.d.	-9.6	HW
A9P4	1.733103	36.291111	0.67	81.21	18.05	676.82	5.91	6.32	b.d.	15.89	-8.6	HW
A11P36	1.789639	36.268178	0.94	82.83	16.05	1735.20	2.00	9.37	b.d.	19.63	-5.7	FZ
A11P29	1.791111	36.271242	0.66	82.73	16.53	776.27	12.62	6.91	b.d.	b.d.	-4.3	FZ
A11P32	1.790764	36.269622	0.69	82.19	17.01	1107.14	9.93	5.06	b.d.	14.95	-3.8	FZ
A11P22	1.785847	36.278933	0.69	81.18	18.05	779.67	8.95	5.99	b.d.	15.39	-9.1	FW
A12P7	1.801833	36.359917	0.85	83.54	15.56	527.89	2.15	7.77	b.d.	b.d.	-9.3	HW
A12P4	1.804222	36.364472	0.84	80.77	18.32	618.92	1.47	9.79	b.d.	18.57	-6.8	HW
A12P17	1.780528	36.351111	0.85	80.56	18.52	666.84	1.66	5.89	b.d.	b.d.	-9.3	HW
A12P9	1.799083	36.355278	0.70	82.78	16.43	822.19	7.42	6.65	b.d.	15.84	-8.5	HW
A12P19	1.779556	36.347639	0.78	80.08	19.05	893.78	0.84	5.58	b.d.	16.00	-6.9	HW
A12P1	1.802944	36.362472	0.71	82.26	16.98	487.25	7.25	7.51	b.d.	b.d.	-9.8	HW
A13P38	1.855694	36.30675	0.87	82.01	17.01	1106.85	2.09	10.20	b.d.	b.d.	-7.4	FZ
A13P37	1.860667	36.306194	0.85	82.04	17.00	981.63	9.35	10.16	b.d.	b.d.	-9.3	FZ
A13P31	1.860861	36.309583	0.69	82.00	17.24	687.88	7.39	6.63	b.d.	18.52	-8.1	HW

	A14P6	1.734694	36.283478	0.68	81.40	17.81	1103.97	7.41	8.97	b.d.	19.51	-6.3	FZ	
	A14P20	1.723619	36.271606	0.67	80.63	18.58	1107.60	6.94	5.47	b.d.	b.d.	-7.3	FZ	
	A14P18	1.724681	36.273306	0.68	80.81	18.34	1647.35	7.41	5.82	b.d.	16.39	-6.5	FZ	
	A14P7	1.735419	36.283494	0.65	77.72	21.51	1202.78	6.02	6.74	b.d.	b.d.	-8.3	FZ	
	A14P10	1.730081	36.281619	0.69	81.60	17.49	2058.20	6.80	6.23	b.d.	16.86	-8.6	FZ	
	A14P21	1.719167	36.269775	0.85	80.44	18.56	1420.52	32.71	10.04	b.d.	17.82	-8.9	FZ	
	A14P1	1.727233	36.283283	0.68	80.96	18.28	787.91	6.45	5.72	b.d.	b.d.	-9.6	FW	
	A14P4	1.731719	36.283842	0.68	82.13	17.11	771.18	5.77	11.76	b.d.	b.d.	-9.1	HW	
Natron	T1P1	2.373139	35.905806	0.67	81.78	17.47	773.14	8.26	5.42	b.d.	0.00	-9.3	FZ	
	T1P2	2.373083	35.905278	0.69	82.51	16.69	1068.13	7.57	6.23	b.d.	14.40	-7.5	FZ	
	T1P5	2.372639	35.904167	0.74	84.09	15.08	872.89	8.48	7.14	b.d.	24.81	-7.8	FZ	
	T1P12	2.375583	35.904111	0.73	83.41	15.78	779.56	8.27	9.96	b.d.	20.67	-7.9	FZ	
	T1P18	2.385	35.905194	0.73	83.83	15.34	988.28	8.04	5.96	b.d.	0.00	-8.8	FZ	
	T1P23	2.392278	35.898278	0.73	84.07	15.12	879.30	7.98	6.49	b.d.	0.00	-8.3	FZ	
	T3P12	2.679528	35.882139	0.72	83.73	15.46	807.21	7.87	10.21	b.d.	0.00	-7.5	FZ	
	T3P13	2.6795	35.882389	0.70	83.83	15.38	882.85	7.37	6.17	b.d.	16.22	-8.1	FZ	
	T3P14	2.6795	35.882722	0.72	81.05	18.13	961.39	6.20	6.24	b.d.	18.98	-7.9	FZ	
	T3P17	2.679833	35.882667	0.76	83.66	15.49	872.08	7.40	6.11	b.d.	15.45	-8.0	FZ	
	T3P22	2.680667	35.882889	0.70	81.08	18.15	699.21	6.90	11.90	b.d.	0.00	-7.7	FZ	
	T3P26	2.680694	35.884056	0.71	83.61	15.56	1183.75	7.05	5.76	b.d.	0.00	-9.9	FZ	
	T3P28	2.680657	35.884472	0.72	80.80	18.38	865.70	7.09	5.55	b.d.	0.00	-9.8	FZ	
	T3P34	2.679583	35.8855	0.61	83.67	15.66	683.20	7.73	6.55	b.d.	0.00	-7.7	FZ	
	T3P35	2.678889	35.88525	0.68	82.19	17.02	1033.39	7.66	9.76	b.d.	15.90	-10.6	FZ	
	T5P45	2.767	36.044861										-11.7	HW
	T6P7	2.453806	36.086861	0.85	77.64	21.39	1214.85	5.82	8.35	b.d.	21.70	-6.4	FZ	
	T6P9	2.453944	36.087556	0.81	81.12	17.97	908.40	8.30	5.94	b.d.	0.00	-7.4	FZ	
	T6P3	2.453556	36.086111	0.82	81.65	17.44	922.00	7.89	5.80	b.d.	0.00	-7.7	FZ	
	T6P6	2.453778	36.086611	0.80	79.00	20.06	1414.51	7.18	6.25	b.d.	0.00	-7.2	FZ	
	T6P11	2.453889	36.088278	0.84	80.19	18.87	1034.56	8.78	7.39	b.d.	16.76	-7.8	FZ	
	T6P2	2.453	36.085944	0.86	83.62	15.43	879.47	13.15	11.22	b.d.	19.29	-8.6	HW	
	T6P13	2.45425	36.088667	0.83	79.15	19.93	872.40	9.54	9.50	b.d.	0.00	-8.7	FZ	
	T6P16	2.454972	36.088806	0.88	83.85	15.19	829.02	9.58	12.10	b.d.	14.96	-8.7	FW	
T7P27	2.526639	36.045278	0.85	81.60	17.33	1012.82	9.62	10.44	1250.03	0.00	-6.2	FZ		
T7P31	2.5265	36.046583	0.88	82.90	16.14	795.65	9.74	6.41	b.d.	15.62	-6.4	FZ		
T7P29	2.526083	36.046111	0.88	83.97	15.06	808.82	9.74	6.33	b.d.	22.35	-6.5	FZ		
T7P24	2.526639	36.044278	0.81	82.33	16.76	957.88	9.78	10.15	b.d.	0.00	-7.7	FZ		

	T7P22	2.526361	36.043667	0.84	83.75	15.31	995.48	9.32	11.58	b.d.	18.75	-8.8	FZ
	T7P23	2.526389	36.043972	0.87	83.36	15.68	888.45	9.57	9.78	b.d.	0.00	-8.7	FZ
	T7P35	2.527333	36.049278	0.87	83.75	15.29	762.89	9.52	10.10	b.d.	19.22	-8.1	FW
	T8P42	2.59325	36.015889	0.90	81.56	17.44	925.20	10.26	6.20	b.d.	15.73	-7.8	FZ
	T8P36	2.592333	36.014194	0.92	83.52	15.43	1224.22	10.44	6.37	b.d.	0.00	-8.2	FZ
	T8P38	2.592472	36.014778	0.84	79.33	19.74	853.63	9.65	5.44	b.d.	0.00	-8.6	FZ
	T8P40	2.592889	36.015333	0.93	83.36	15.60	1072.86	11.80	5.72	b.d.	0.00	-9.1	FZ
	T9P47	2.610667	35.989583	0.87	83.67	15.37	887.28	10.64	6.16	b.d.	19.08	-9.1	HW
	T9P49	2.606694	35.971306	0.83	82.24	16.86	669.92	9.44	5.91	b.d.	0.00	-10.6	HW
	T9P52	2.618306	35.927556	0.64	77.08	22.19	788.17	6.82	6.94	b.d.	15.86	-9.8	HW
	T9P53	2.620972	35.908028	0.69	83.42	15.78	1040.75	7.79	6.72	b.d.	16.62	-9.7	HW
Oldoinyo Lengai North Crater	OL21	2.761513	35.91533									-5.7	
	OL23	2.761339	35.915594	0.83	83.16	15.14	8655.19	9.82	6.49	b.d.	21.48	-3.0	
	OL24	2.761322	35.915638	0.83	83.16	15.29	7091.05	9.79	12.26	b.d.	20.51	-2.2	

FZ: fault zone. HW: hanging wall. FW: footwall. b.d.: below detection limit. No gas chemistry data for T5P45 and OL21.

Table S2. Diffuse CO₂ flux data (in g m⁻² d⁻¹) for different structural zones in the Magadi and Natron basin study areas.

	Magadi basin			Natron basin		
	fault zone	hanging wall	footwall	fault zone	hanging wall	footwall
number of data	174	186	93	71	24	17
mean flux	36.6	8.8	1.9	17.2	11.7	1.1
error (95% conf.)	11	2.6	1.4	5	6.8	0.8

Table S3: Summary of diffuse CO₂ flux for the Magadi-Natron basin, including mean and total flux from different structural zones, and estimated annual flux from each study area.

study area	structural zone	mean flux (g m ⁻² d ⁻¹)	area (km ²)	total flux (g d ⁻¹)	annual flux (Mt yr ⁻¹)
Magadi	fault zones	36.6 ± 11.0	72.9	2.7 x 10 ⁹	0.98 ± 0.29
	hanging walls	8.8 ± 2.6	150.7	1.3 x 10 ⁹	0.48 ± 0.14
	footwalls	1.9 ± 1.4	183.8	3.5 x 10 ⁸	0.13 ± 0.10
	total		407.5		1.59 ± 0.53
Natron	fault zones	17.2 ± 5.0	33.1	5.7 x 10 ⁸	0.21 ± 0.06
	hanging walls	11.7 ± 6.8	526.5	6.2 x 10 ⁹	2.25 ± 1.31
	footwalls	1.1 ± 0.8	14.4	1.6 x 10 ⁷	< 0.01
	total		574		2.46 ± 1.37

Mean and annual flux values are within 95% confidence

Table S4: Locations, temperatures, and pH of springs in the Magadi-Natron basin.

	ID	latitude (S°)	longitude (E°)	Temperature (°C)	pH
Magadi	KN14-S01	1.85744	36.21900	48.4	8.9
	KN14-S02	1.86319	36.21983	47.7	9.3
	KN14-S03	1.83581	36.21839	46.4	9.1
	KN14-S04	1.84329	36.21583	34.1	-
	KN14-S05	2.00228	36.23148	44.7	9.8
	KN14-S06	1.99825	36.23131	44.6	9.9
	KN14-S07	2.00284	36.22848	39	9.8
	KN14-S08	1.72756	36.28086	83.5	9.5
	KN14-S09	1.72547	36.27828	82.3	9.3
	KN14-S10	1.72461	36.27308	-	-
	KN14-S11	1.85989	36.30636	35	10
Natron	TZ14-S01	2.37314	35.90581	50.7	10.3
	TZ14-S02	2.39228	35.89828	51.2	10.3
	TZ14-S03	2.45581	36.08842	43.1	9.5
	TZ14-S04	2.52733	36.04928	-	-
	TZ14-S05	2.52733	36.04928	38.1	9.3
	TZ14-S06	2.59283	36.01597	36.8	9.2

A.1.3. SUPPLEMENTARY REFERENCES

- Albaric, J., Déverchère, J., Perrot, J., Jakovlev, A., and Deschamps, A. (2014) Deep crustal earthquakes in North Tanzania, East Africa: interplay between tectonic and magmatic processes in an incipient rift. *Geochem. Geophys. Geosyst.* **15**, 374–394.
- Angelier, J. Bergerat, F., Dauteuil, O., and Villemin, T. (1997) Effective tension-shear relationships in extensional fissure swarms, axial rift zone of northeastern Iceland. *J. Struct. Geol.* **19**, 673–685.
- Belachew, M., Ebinger, C., Coté, D., Keir, D., Rowland, J. V., Hammond, J. O. S., and Ayele, A. (2011) Comparison of dike intrusions in an incipient seafloor-spreading segment of Afar, Ethiopia: seismicity perspectives. *J. Geophys. Res.* **116**, B06405.
- Biggs, J., Amelung, F., Gourmelen, N., Dixon, T. H., and Kim, S. W. (2009) InSAR observations of 2007 Tanzania rifting episode reveal mixed fault and dyke extension in an immature continental rift. *Geophys. J. Int.* **179**, 549–558.
- Birt, C. S., Maguire, P. K. H., Khan, M. A., Thybo, H., Keller, G. R., and Patel, J. (1997) The influence of pre-existing structures on the evolution of the southern Kenya rift valley – Evidence from seismic and gravity studies. *Tectonophysics* **278**, 211–242.
- Burton, M. R., Sawyer, G. M., and Granieri, D. (2013) Deep carbon emission from volcanoes. *Rev. Mineral. Geochem.* **75**, 323-354.

- Calais, E., d Oreye, N., Albaric, J., Deschamps, A., Delvaux, D., Deverchere, J., Ebinger, C., Ferdinand, R.W., Kervyn, F., Macheyeke, A.S., Oyen, A., Perrot, J., Saria, E., Smets, B., Stamps, D.S., and Wauthier, C. (2008) Aseismic strain accommodation by slow slip and dyking in a youthful continental rift, East Africa. *Nature* **456**, 783-787.
- Chiodini, G., Cardellini, C., Amato, A., Boschi, E., Caliro, S., Frondini, F., and Ventura, G. (2004) Carbon dioxide Earth degassing and seismogenesis in central and southern Italy. *Geophys. Res. Lett.* **31**, L07615.
- Chiodini, G., Caliro, S., Cardellini, C., Avino, R., Granieri, D., and Schmidt, A. (2008) Carbon isotopic composition of soil CO₂ efflux, a powerful method to discriminate different sources feeding soil CO₂ degassing in volcanic hydrothermal areas. *Earth Planet. Sci. Lett.* **274**, 372–379.
- Cowie, P. A., Scholz, C., Edwards, M., and Malinverno, A. (1993) Fault strain and seismic coupling on mid-ocean ridges. *J. Geophys. Res.* **98**, 17911-17920.
- Crossley, R. (1979) The Cenozoic stratigraphy and structure of the western part of the Rift Valley in southern Kenya. *J. Geol. Soc. London* **139**, 393-405.
- Deutsch, C. V. and Journel, A. G. (1998) GSLIB: Geostatistical software library and users guide. *Oxford Univ. Press*, New York.
- Ebinger, C. J. and Scholz, C. A. (2012) Continental Rift Basins: The East African Perspective. in *Tectonics of sedimentary basins: recent advances Ch. 9* (eds. Busby, C. & Azor, A.) (John Wiley & Sons, Chichester, UK).

- Foster, A., Ebinger, C., Mbede, E., and Rex, D. (1997) Tectonic development of the northern Tanzanian sector of the east African rift system. *J. Geol. Soc.* **154**, 689–700.
- Geissler, W.H., Kämpf, H., Kind, R., Bräuer, K., Klinge, K., Plenefisch, T., Horálek, J., Zednik, J., Nehybka, V. (2005) Seismic structure and location of a CO₂ source in the upper mantle of the western Eger (Ohře) rift, central Europe. *Tectonics* **24**, TC5001.
- Grant, J. V. and Kattenhorn, S. A. Evolution of vertical faults at an extensional plate boundary, southwest Iceland. *J. Struct. Geol.* **26**, 537–57 (2004).
- Hollnack, D., and Stangl, R. The seismicity related to the southern part of the Kenya rift. *J. Afr. Earth Sci.* **26**, 477–495 (1998).
- Ibs-von Seht, M., Blumenstein, S., Wagner, R., Hollnack, D., and Wohlenberg, J. (2001) Seismicity, seismotectonics and crustal structure of the southern Kenya Rift – new data from the Lake Magadi area. *Geophys. J. Int.* **146**, 439–453.
- Jolie, E., Klinkmueller, M., and Moeck, I. (2015) Diffuse surface emanations as indicator of structural permeability in fault-controlled geothermal systems. *J. Volcanol. Geotherm. Res.* **290**, 97–113.
- Kagoshima, T., Sano, Y., Takahata, N., Maruoka, T., Fischer, T.P., and Hattori, K. (2015) Sulphur geodynamic cycle. *Sci. Rep.* **5**, 8330.
- Keir, D., Ebinger, C. J., Stuart, G. W., Daly, E., and Ayele, A. (2006) Strain accommodation by magmatism and faulting as rifting proceeds to breakup: seismicity of the northern Ethiopian rift. *J. Geophys. Res.* **111**, B05314.

- Keir, D., Bastow, I. D., Whaler, K. A., Daly, E., Cornwell, D. G., and Hautot, S. (2009) Lower crustal earthquakes near the Ethiopian rift induced by magmatic processes. *Geochem. Geophys. Geosyst.* **10**, Q0AB02.
- Keir, D., Hamling, I.J., Ayele, A., Calais, E., Ebinger, C., Wright, T.J., Jacques, E., Mohamed, K., Hammond, J.O.S., Belachew, M., Baker, E., Rowland, J.V., Lewi, E. and Bennati, L. (2011) Mapping the evolving strain field during continental breakup from crustal anisotropy in the Afar Depression. *Nature Communications* **2**, 285.
- Keller, G. R., Mechie, J., Braile, L.W., Mooney, W. D., and Prodehl, C. (1994) Seismic structure of the uppermost mantle beneath the Kenya rift. *Tectonophysics* **236**, 201–216.
- Kendall, J. -M., Stuart, G. W., Ebinger, C. J., Bastow, I. D., and Keir, D. (2004) Magma-assisted rifting in Ethiopia, *Nature* **433**, 146–148.
- Kennedy, B. M., Kharaka, Y. K., Evans, W. C., Ellwood, A., DePaolo, D. J., Thordsen, J. J., Ambats, G., Mariner, R. H. (1997) Mantle fluids in the San Andreas fault system, California. *Science* **278**, 1278–1281.
- Keranen, K., Klempere, S., and Gloaguen, R. (2004) EAGLE Working Group, Three dimensional seismic imaging of a proto-ridge axis in the Main Ethiopian Rift, *Geology* **39**, 949–952.
- Lindenfeld, M., Rumpker, G., Link, K., Koehn, D., and Batte, A. (2012) Fluid-triggered earthquake swarms in the Rwenzori region, East African Rift - evidence for rift initiation. *Tectonophysics* **566**, 95-104.

- Marty, B. and Tolstikhin, I. N. (1998) CO₂ fluxes from mid-ocean ridges, arcs and plumes. *Chem. Geol.* **145**, 233–248.
- Morner, N. A. and Etiope, G. (2002) Carbon degassing from the lithosphere. *Glob. Planet. Change* **33**, 185–203.
- Mulibo, G. and Nyblade, A. (2009) The 1994–1995 Manyara and Kwamtoro earthquake swarms: variation in the depth extent of seismicity in northern Tanzania. *S. Afr. J. Geol.* **112**, 387–404.
- Nyblade, A. A., Birt, C., Langston, C. A., Owens, T. J., and Last, R. J. (1996) Seismic experiment reveals rifting of the craton in Tanzania. *Eos* **77**, 517–521.
- Pérez, N.M., Hernández, P.A., Padilla, G., Nolasco, D., Barrancos, J., Melían, G., Padrón, E., Dionis, S., Calvo, D., Rodríguez, F., Notsu, K., Mori, T., Kusakabe, M., Arpa, C., Reniva, P., and Ibarra, M. (2011) Global CO₂ emission from volcanic lakes. *Geology* **39**, 235–238.
- Reyners, M., Eberhart-Phillips, D., and Stuart, G. (2007) The role of fluids in lower-crustal earthquakes near continental rifts. *Nature* **446**, 1075–1079.
- Sherrod, D. R., Magigita, M. M., and Kwelwa, S. (2013) Geologic map of Oldonyo Lengai (Oldoinyo Lengai) volcano and surroundings, Arusha region, *United Republic of Tanzania. Tech. Rep. 2013-1306*, U.S. Geol. Surv. pp. 65.
- Werner, C. and Cardellini, C. (2006) Comparison of carbon dioxide emissions with fluid upflow, chemistry, and geologic structures at the Rotorua geothermal system, New Zealand. *Geothermics* **35**, 221–238.

Wahler, K. and Hautot, S. (2006) The electrical resistivity structure of the crust beneath the northern Ethiopian rift. *Geol. Soc. Spec. Publ.* **256**, 294–305.

APPENDIX 2: SUPPLEMENRTARY INFORMATION FOR CHAPTER 3

Table S1. Water chemistry of hot springs in the Magadi-Natron basin and the Kenya Rift Valley.

Sample ID	TDS	HCO ₃	CO ₃	Na	K	Ca	Mg	B
mg/L								
KN14-S01	29,673	12,488	1,360	10,572	183	2	0.3	7.1
KN14-S02	32,310	15,580	2,820	8,551	204	0.3	n.d.	5.3
KN14-S03	26,744	12,753	2,080	7,330	169	1.3	0.1	7
KN14-S05	42,186	15,824	7,081	12,309	212	0.3	n.d.	12.9
KN14-S06	40,023	15,783	7,041	10,442	220	0.9	0.1	12.3
KN14-S07	29,743	11,675	4,881	8,244	170	0.7	0.1	11
KN14-S08	36,257	16,231	4,281	9,929	294	1.1	0.1	8.9
KN14-S09	41,623	18,224	3,881	11,210	306	0.7	0.1	10.6
KN14-S11	29,261	11,357	5,961	7,423	184	0.2	n.d.	12.2
TZ14-S01	23,145	8,420	5,001	5,950	156	0.4	n.d.	13.4
TZ14-S02	24,120	7,790	4,481	8,142	147	0.9	0.1	10
TZ14-S03	42,920	20,380	4,721	11,530	356	0.5	0.4	11.1
TZ14-S05	9,599	5,166	580	2,534	75	0.8	0.8	3.5
TZ14-S06	6,005	3,112	260	1,740	40	0.5	1.5	2.8
Lorusio	7,496	4,100	1,176	1,592	78	3.2	0.2	0.9
Kapedo	3,421	2,120	135	682	54	1.3	0.5	0.5
Bogoria	4,167	2,526	300	846	35	0.3	0.1	0.5

Table S1. (continued).

Sample ID	Li	Si	Cl	NO₃	PO₄	SO₄	Br	F
mg/L								
KN14-S01	0.3	41.1	4,596	18.5	9.0	230	80.5	85.5
KN14-S02	0.7	26.9	4,809	26.4	n.d.	114	81.5	89.6
KN14-S03	0.8	36.5	4,133	12.7	3.5	114	32.1	70.3
KN14-S05	0.6	55.7	6,369	11	16.6	81	94.3	118.8
KN14-S06	0.6	56	6,122	n.d.	n.d.	206	31.5	108.2
KN14-S07	0.6	56.6	4,258	77.8	n.d.	211	75.8	82.8
KN14-S08	1.6	35.7	5,146	25.9	n.d.	81	86.3	136.2
KN14-S09	1.7	42.4	6,011	1628.4	n.d.	69	86.7	152.2
KN14-S11	0.7	54.7	4,077	7.0	n.d.	69	25.5	89.9
TZ14-S01	0.5	80.8	3,047	5.4	16.3	304	72.7	78.4
TZ14-S02	0.5	49.2	2,914	77.7	16.5	340	74.7	76.7
TZ14-S03	0.5	32	4,888	75.6	68.8	601	81.6	174.9
TZ14-S05	0.5	23.5	1,029	10	4.6	134	10.3	27.9
TZ14-S06	0.5	21.9	686	2.3	1.9	99	9.5	26.4
Lorusio	1.1	36	321	26.7		114	7.0	39
Kapedo	0.6	36.6	267	2.8		101	8.0	14
Bogoria	0.5	41.5	281	1.2		74	8.0	54

APPENDIX 3: SUPPLEMENTARY INFORMATION FOR CHAPTER 4

Table S1. Whole gas compositions and Ar isotopes of the Costa Rican springs.

ID	sampling date	Ar	He	N₂	O₂	CO₂
CR14-01	5/1/2014					
CR12-16	2/29/2012	2.08	0.011	97.6	0.2	0.021
CR14-02	5/1/2014	1.66	0.044	96.1	1.2	0.005
CR12-15	2/29/2012	1.39	0.015	92.1	6.3	0.224
CR14-03	5/1/2014	1.83	0.021	89.2	8.3	0.441
CR14-06A	5/2/2014	0.05	0.001	3.1	1.0	0.87
CR14-06B		0.03	0.001	2.0	0.2	0.936
CR14-07	5/3/2014	1.27	0.024	62.4	0.7	30.383
CR12-14	2/29/2012	1.32	0.004	98.3	0.3	0.047
CR14-08	5/3/2014	1.11	0.04	95.4	1.9	0.054
CR14-09	5/4/2014	0.36	0.012	16.5	0.5	nd
CR14-09B		0.56	0.024	53	10.3	0.022
CR12-01	2/24/2012	0.04	0.0004	2.1	0.2	1.092
CR12-02		0.05	nd	3.7	0.6	1.875
CR12-03	2/25/2012	0.20	0.004	12.4	0.04	17.372
CR12-04		0.12	0.00001	8	0.004	18.447
CR12-05	2/25/2012	1.43	0.021	92.3	6.0	0.259
CR12-06		1.66	0.02	97.8	0.1	0.32
CR12-07	2/26/2012	0.68	0.026	96.9	0.2	0.011
CR12-08		0.83	0.023	96.8	0.1	0.004
CR12-09	2/26/2012	0.85	0.027	92.8	0.2	4.553
CR12-10		1.02	0.023	96.2	0.003	1.201
CR12-11	2/26/2012	1.09	0.028	98.5	0.3	0.002
CR12-12		1.54	0.027	98.3	0.01	0.007
CR12-13	2/26/2012	2.91	0.019	88	8.6	0.414
CR12-18	3/1/2012	0.66	0.007	96.6	2.3	0.377
CR12-19	3/1/2012	0.02	0.013	1.1	0.5	98.4
CR14-11	5/4/2014	0.46	0.042	49.8	1.0	47.2

Table S1. (continued).

ID	H ₂	CH ₄	CO	⁴⁰ Ar/ ³⁶ Ar	±
CR14-01					
CR12-16	nd	0.09	nd		
CR14-02	0.814	0.18	0.038	317.2	0.1
CR12-15	nd	0.01	nd		
CR14-03	nd	0.17	0.008	305.2	0.1
CR14-06A	0.001	94.98	nd	300.1	0.1
CR14-06B	nd	96.8	nd	293.3	0.1
CR14-07	0.031	5.20	nd	305.9	0.1
CR12-14	0.014	0.001	nd		
CR14-08	nd	1.48	nd	307.5	0.1
CR14-09	0.065	82.50	nd	291	0.1
CR14-09B	nd	36.08	nd	300	0.1
CR12-01	nd	96.49	nd	282.5	6.2
CR12-02	0.002	93.82	nd	271.1	4.1
CR12-03	0.006	69.99	nd	290.5	3.0
CR12-04	0.014	73.39	nd	290.8	3.4
CR12-05	0.001	0.01	nd	293.6	15
CR12-06	nd	0.01	nd	296.8	7.9
CR12-07	0.022	2.16	nd	302.2	7.1
CR12-08	0.002	2.29	nd	302.2	17.7
CR12-09	nd	1.60	nd	293.8	8.5
CR12-10	0.015	1.51	nd	297.7	18.6
CR12-11	0.003	0.04	nd		
CR12-12	0.048	0.04	nd		
CR12-13	0.027	0.0003	0.004		
CR12-18	nd	0.06	nd		
CR12-19	nd	0.001	0.0005	292.1	7.2
CR14-11	nd	1.47	nd	301.8	< 0.1

Table S2. End member contributions to nitrogen in the Costa Rican springs.

area	sample ID	f_{MORB} (%)	f_{sediment} (%)	f_{air} (%)
Nicoya	CR14-01	11	0	89
	CR12-16	19	0	81
	CR14-02	6	0	94
	CR12-15	19	3	78
	CR14-03	8	0	92
	CR14-06B	30	2	68
	CR14-07	1	0	99
Santa Elena	CR14-09	58	42	0
Osa	CR12-01	11	76	13
Burica	CR12-03	14	68	19
Arc front	CR12-05	9	0	91
	CR12-06	9	0	91
	CR12-07	5	26	69
	CR12-08	5	0	95
	CR12-09	7	2	91
	CR12-10	6	15	79
	CR12-11	8	0	92
	CR12-12	11	10	80
	CR12-13	0	0	0
	CR12-18	1	23	76
	CR12-19	64	36	0
CR14-11	20	11	69	

Table S3. Water chemistry of the Costa Rican springs.

	Area	ID	pH	Temp C	TDS
					mg/L
Nicoya	San Martin	CR12-W07	9.1	28.0	262
	Sabana Grande	CR12-W08	8.5	31.5	288
	Rancho Salitral	CR12-W09	10.1	29.6	218
	Salitral Vigia	CR14-S07	7.9	26.0	226
	Finca El Sitio Santa Cruz	CR14-S04	8.1	36.7	264
Santa Elena	Rio Murcielago	CR14-S10	9.0	27.0	32,154
Burica	Laurel	CR12-03	8.3	-	399
		CR12-04	8.1	-	360
Arc front	Monte Carlo	CR12-W05	7.8	32.3	1,372
	Aguas Termales Gevi	CR12-W06	8.1	36.8	413
	Pueblo Antiguo	CR12-W11	7.8	45.3	1,901
	Cayuco	CR12-W12	6.5	72.6	2,849
	Aguas Calientes	CR12-05	6.5	37.2	904
		CR12-06	6.4		902
	Yheri	CR12-07	7.7	26.1	2,408
		CR12-08	6.7		2,428
	Rocas Calientes	CR12-09	7.4	62.8	1,772
		CR12-10	7.8		1,961

Table S3. (continued).

ID	Na	K	Ca	Mg	Li	B	Sr
	mg/L	mg/L	mg/L	mg/L	mg/L	mg/L	mg/L
CR12-W07	64	1.03	1.47	0.04	0.09	1.07	0.03
CR12-W08	69	0.91	1.46	0.07	0.09	1.03	0.03
CR12-W09	54	0.73	1.93	0.02	0.09	1.19	0.02
CR14-S07	21	1.95	22.45	7.59	0.06	0.11	0.07
CR14-S04	65	0.64	2.37	0.00	0.08	0.88	-
CR14-S10	9,457	190.93	1.73	0.06	2.01	7.02	0.09
CR12-03	2	13.87	7.98	6.62	0.56	8.73	0.01
CR12-04	8	5.90	46.23	16.68	0.02	0.18	0.19
CR12-W05	305	4.67	137.70	0.00	0.83	2.15	1.12
CR12-W06	85	6.34	15.74	1.03	0.86	7.17	0.41
CR12-W11	429	8.57	184.80	0.47	1.00	6.46	1.94
CR12-W12	727	40.61	72.37	28.25	1.60	14.37	-
CR12-05	108	1.15	122.40	0.68	-	1.82	0.99
CR12-06	108	1.08	121.90	0.68	-	1.41	0.99
CR12-07	461	21.05	310.10	0.00	0.65	21.00	3.37
CR12-08	459	3.49	314.40	0.00	-	6.19	3.41
CR12-09	392	11.01	101.50	1.37	0.18	8.05	3.03
CR12-10	396	25.84	100.30	1.39	1.02	21.80	2.97

Table S3. (continued).

ID	HCO ₃	Cl	NO ₃	SO ₄	Br	F	SiO ₂
	mg/L	mg/L	mg/L	mg/L	mg/L	mg/L	mg/L
CR12-W07	161	3.1	-	8.62	-	3.28	18
CR12-W08	178	7.1	0.65	11.70	-	2.37	15
CR12-W09	92	25	0.71	17.13	-	1.98	24
CR14-S07	129	10	0.63	4.26	0.44	0.38	27
CR14-S04	99	25	0.28	33.27	0.36	0.54	37
CR14-S10	16,108	5,894	74.85	214	26	138	40
CR12-03	340	3.4	0.56	0.42	0.43	0.17	15
CR12-04	273	3.2	0.16	0.22	0.29	0.30	6
CR12-W05	26	539	1.31	340	1.91	0.70	10
CR12-W06	66	74	5.69	129	0.73	6.23	15
CR12-W11	32	652	0.66	557	1.51	7.51	17
CR12-W12	161	906	7.22	850	12.91	2.18	24
CR12-05	32	104	0.12	509	0.32	0.38	22
CR12-06	28	104	0.55	516	0.33	0.39	20
CR12-07	45	1,491	1.88	3.0	4.90	1.49	45
CR12-08	20	1,594	0.99	4.0	4.67	1.60	16
CR12-09	61	707	0.91	443	2.18	2.22	38
CR12-10	195	709	0.63	443	2.10	16.93	45

Table S4. Oxygen and hydrogen isotope compositions (‰ vs. VSMOW) of the Costa Rican springs.

	Area	ID	$\delta^{18}\text{O}$	δD
Nicoya	Rancho Salitral	CR12-W09	-8.8	-60.2
	Salitral San Martin	CR12-W07	-8.0	-55.2
	Sabana Grande	CR12-W08	-7.7	-54.8
	Finca El Sitio Santa Cruz	CR14-S04	-8.2	-57.3
	Salitral Vigia	CR14-S07	-7.3	-50.7
Santa Elena	Rio Murcielago 1	CR14-09b	-7.2	-48.3
	Rio Murcielago 2	CR14-S10	-0.2	-5.6
Burica	Laurel	CR12-03	-6.0	-44.3
	Laurel	CR12-04	-7.0	-45.8
Arc front	Monte Carlo	CR12-W05	-11.6	-78.2
	Aguas Termales Gevi	CR12-W06	-11.8	-82.0
	Pueblo Antiguo	CR12-W11	-8.8	-64.1
	Cayuco	CR12-W12	-8.9	-63.3
	Aguas Calientes	CR12-05	-11.3	-76.6
	Aguas Calientes	CR12-06	-10.9	-74.7
	Yheri	CR12-07	-10.2	-70.3
	Yheri	CR12-08	-10.7	-71.5
	Rocas Calientes	CR12-09	-11.2	-75.2
	Rocas Calientes	CR12-10	-10.6	-73.1
	Rincon Vulcan cite travertine	CR14-S11	-4.4	-25.7

Table S5. Diffuse CO₂ flux values of the Santa Cruz area, Nicoya.

EGM-4 Data		T=30°C	
Software Version=1.05			
Plot	Flux (g/m² day)	Lat (10°N)	Long (85°W)
1	33.120	18.984	35.952
2	10.548	18.961	35.963
3	1.360	18.938	35.977
4	0.810	18.919	35.995
5	3.180	18.9	36.018
6	2.150	18.883	36.034
7	5.380	18.858	36.036
8	3.976	18.834	36.044
9	7.360	18.802	36.048
10	0.570	18.784	36.067
11	0.846	18.762	36.084
12	0.544	18.747	36.105
13	0.240	18.726	36.13
14	2.560	18.705	36.148

Table S6. Diffuse CO₂ flux values of the Salitral Vigia area, Nicoya.

EGM-4 Data		T=30°C	
Software Version=1.05			
Plot	Flux (g/m² day)	Lat (10°N)	Long (85°W)
1	12.311	6.382	17.679
2	13.869	6.404	17.680
3	15.120	6.432	17.681
4	14.712	6.461	17.682
5	18.284	6.489	17.687
6	18.080	6.518	17.685
7	17.832	6.545	17.690
8	32.580	6.581	17.688
9	89.760	6.572	17.684
10	16.516	6.606	17.681
11	22.133	6.634	17.674
12	16.217	6.659	17.668
13	3.760	6.686	17.665
14	15.447	6.712	17.658
15	14.496	6.738	17.650
16	25.200	6.592	17.652
17	28.880	6.574	17.651
18	14.664	6.569	17.641
19	42.600	6.578	17.627
20	8.200	6.571	17.604
21	51.520	6.575	17.576
22	5.990	6.554	17.583
23	27.800	6.533	17.620